

# CHALMERS



## Fault Detection in HVDC-Connected Wind Farm with Full-Scale Converter Generator (FCG) Wind Turbines

*Master's Thesis in Electric Power Engineering*

RONI IRNAWAN

Department of Energy and Environment  
*Division of Electric Power Engineering*  
CHALMERS UNIVERSITY OF TECHNOLOGY  
Göteborg, Sweden 2011

MASTER'S THESIS

Fault Detection in HVDC-Connected Wind Farm with  
Full-Scale Converter Generator (FCG)  
Wind Turbines

Master's Thesis in Electric Power Engineering

RONI IRNAWAN



Department of Energy and Environment  
*Division of Electric Power Engineering*  
CHALMERS UNIVERSITY OF TECHNOLOGY

Göteborg, Sweden 2011

Fault Detection in HVDC-Connected Wind Farm with Full-Scale Converter Generator  
(FCG) Wind Turbines  
RONI IRNAWAN

©RONI IRNAWAN, 2011

Master's Thesis  
Department of Energy and Environment  
Division of Electric Power Engineering  
Chalmers University of Technology  
SE-412 96 Göteborg  
Sweden  
Telephone: + 46 (0)31-772 1000

Cover:  
Lillgrund – the largest offshore wind farm in Sweden. (<http://goo.gl/5AVEr>)

Chalmers Reproservice  
Göteborg, Sweden 2011



# Abstract

The wind energy technology has rapidly developed during the last decade. HVDC-connected wind farm with full-scale converter generator (FCG) become a popular solution to be applied in the remote wind farm.

During short-circuit fault, the peak as well as the steady state current contribution from FCG and HVDC is usually limited to 10% above their rated current, due to the safety reason of the power electronic switch used in the FCG and HVDC. This condition makes the protection system design become a challenging task.

In this thesis the fault detection methods in the HVDC-connected wind farm with FCG are proposed. The case study system is implemented in the transient simulation program PSCAD/EMTDC. Three-phase to ground fault is applied in six different locations in the wind farm collection point. The voltage and current measurements from the simulation are then sampled and post-processed using MATLAB to imitate the work of digital protective relay.

After analyzing the signal processing output, the faulty feeder can be detected by observing the instantaneous active power direction of the HVDC feeder, together with the peak current measurement or the current spectrum magnitude of the wind farm feeder. The faulty section within a feeder can be detected either by comparing the peak current or the instantaneous active power direction or the trajectory of positive sequence line-ground impedance between two contiguous measurement units.

Different system conditions to verify the proposed fault detection method are also discussed, the result shown that short-circuit fault within the system is difficult to detect when short-circuit current contribution from HVDC is reduced to 0.1 p.u.

# Acknowledgment

This thesis work has been carried out at ABB Corporate Research, Västerås, Sweden. I would like to express my deep gratitude to my supervisors at ABB, Dr. Giovanni Velotto, Dr. Kailash Srivastava, and Dr. Muhamad Reza, for their excellent supervision and helps during the work.

I would like to express gratitude to Dr. Tuan Le, my thesis examiner at Chalmers University of Technology for providing guidance of my thesis topic selection. I gratefully thank Dr. Stefan Lundberg and Dr. Massimo Bongiorno for their valuable suggestions.

Many thanks to the Indonesian community in Göteborg and Västerås, who has been my second family here in Sweden, and my Indonesian fellow students in Sweden especially Göteborg and Stockholm for their kindness and friendship. Special thanks to *bang* Ricky, *bang* Setyo, *mas* Ibra and *pak* Eko for their corrections in my report.

I also want to thank Hani Pranowo Jati and Desi Pramudiwati for their support during my study here.

Last but not least, my ultimate gratitude go to my parents, Jumiwati and Indriyanto, *mugi-mugi tulisan niki tansah dados bukti bektos kulo dhumateng panjenengan kekalih.*

# Contents

<b>Abstract</b>	<b>i</b>
<b>Acknowledgments</b>	<b>ii</b>
<b>Contents</b>	<b>iii</b>
<b>List of Figures</b>	<b>v</b>
<b>List of Abbreviations</b>	<b>viii</b>
<b>1 Introduction</b>	<b>1</b>
1.1 Background . . . . .	1
1.2 Problem description . . . . .	2
1.3 Scope of the report . . . . .	2
1.4 Limitations of the study . . . . .	3
1.5 Structure of the report . . . . .	3
<b>2 Simulation setup</b>	<b>4</b>
2.1 Wind Farm Description . . . . .	4
2.1.1 Wind farm size and capacity . . . . .	4
2.1.2 Wind farm layouts . . . . .	5
2.1.3 Case study system . . . . .	6
2.2 Main Components Modeling . . . . .	7
2.2.1 FCG model . . . . .	7
2.2.2 HVDC model . . . . .	15
2.2.3 Cable model . . . . .	16
<b>3 Short-Circuit Studies</b>	<b>18</b>
3.1 Short-circuit studies . . . . .	18
3.2 Simulation scenarios . . . . .	19
3.3 Simulation results . . . . .	19
3.3.1 Collection point . . . . .	20
3.3.2 Feeder line . . . . .	24
3.4 Fault clearing time . . . . .	26
<b>4 Fault Detection</b>	<b>27</b>
4.1 Digital protective relaying . . . . .	27
4.2 Results and analysis . . . . .	29
4.2.1 Collection point . . . . .	29
4.2.2 Feeder line . . . . .	33
4.3 Different simulation conditions . . . . .	37

4.3.1	Different sampling frequency . . . . .	37
4.3.2	Different wind turbines condition . . . . .	42
4.3.3	Reduced HVDC short-circuit current contribution . . . . .	45
4.3.4	Reduced HVDC short-circuit current contribution and different wind turbines condition . . . . .	48
4.3.5	Different wind turbines and HVDC power rating . . . . .	51
<b>5</b>	<b>Conclusions and Future Works</b>	<b>56</b>
5.1	Conclusions . . . . .	56
5.2	Future works . . . . .	57
	<b>References</b>	<b>58</b>
<b>A</b>	<b>FCG components modeling</b>	<b>61</b>
A.1	Aerodynamic model . . . . .	61
A.2	Permanent Magnet Synchronous Machine model . . . . .	63
A.3	Generator-side converter model . . . . .	64
<b>B</b>	<b>FCG Model parameters</b>	<b>66</b>

# List of Figures

1.1	Wind farm with HVDC connection . . . . .	2
2.1	Offshore wind farm grid layout . . . . .	5
2.2	Horns Rev 1 layout [1] . . . . .	6
2.3	The case study system layout . . . . .	6
2.4	PMSG with back-to-back PWM converter . . . . .	7
2.5	Simplified model of FCG . . . . .	8
2.6	Power flow dynamic in the DC-link . . . . .	9
2.7	DC chopper schematic . . . . .	9
2.8	Transformation of axis for vector control . . . . .	10
2.9	Grid-side converter control . . . . .	11
2.10	Hysteresis band current controller . . . . .	11
2.11	FCG test system . . . . .	11
2.12	(a) Instantaneous current measured in FCG busbar, (b) dq-axis current measured in FCG busbar, (c) Instantaneous voltage measured in FCG busbar, and (d) Active and reactive power measured in FCG busbar . . . . .	13
2.13	Measurement output during low wind condition:(a) Instantaneous current measured in FCG busbar, (b) dq-axis current measured in FCG busbar, (c) Instantaneous voltage measured in FCG busbar, and (d) Active and reactive power measured in FCG busbar . . . . .	14
2.14	VSC-HVDC transmission system . . . . .	15
2.15	During normal condition, active power flows from wind farm grid to DC-link, while during fault in the wind farm grid, active power flows in reverse direction . . . . .	15
2.16	SE-HVDC converter control mode switch is implemented by sensing the instantaneous voltage ( $v_{SE}$ ) and current ( $i_{SE}$ ). . . . .	16
2.17	Pi line section model . . . . .	16
2.18	HVDC cable geometry implemented in PSCAD/EMTDC . . . . .	17
3.1	Equivalent circuit of FCG/HVDC and synchronous generator (SG) during short-circuit fault . . . . .	18
3.2	Different fault locations for the short-circuit simulation . . . . .	19
3.3	Two observation points in the case system . . . . .	20
3.4	Current behavior when fault occurs in feeder 1 . . . . .	20
3.5	Current flowing in: (a) feeder 1; (b) feeder 2; (c) feeder 3; and (d) HVDC feeder . . . . .	21
3.6	Current behavior when fault occurs in feeder 2 . . . . .	22
3.7	Current flowing in: (a) feeder 1; (b) feeder 2; (c) feeder 3; and (d) HVDC feeder . . . . .	23
3.8	Current behavior when fault is in location 1 . . . . .	24
3.9	Fault current when fault is located in: (a) location 1; (b) location 2; and (c) location 3 . . . . .	25

4.1	Block diagram of digital protective relay . . . . .	27
4.2	Sliding data window method . . . . .	28
4.3	The ellipses indicate the measurement units (MUs) in the collection point .	29
4.4	Peak current magnitude during fault located in (a) feeder 1, and (b) feeder 2	29
4.5	Instantaneous active power behavior when the fault is occurred in (a) loca- tion 1, and (b) SE-HVDC terminal . . . . .	30
4.6	Instantaneous active power during fault in (a) feeder 1, and (b) feeder 2 . .	30
4.7	Current differential behavior when fault occurred in (a) feeder 1, and (b) feeder 2 . . . . .	31
4.8	Current harmonics behavior when fault occurred in feeder 1 . . . . .	31
4.9	Current harmonics behavior when fault occurred in feeder 2 . . . . .	32
4.10	Proposed method for detecting the faulty feeder . . . . .	33
4.11	The ellipses indicate the measurement points along the feeder line . . . . .	33
4.12	Peak current behavior when fault is occurred in (a) location 2, and (b) location 3 . . . . .	34
4.13	Peak voltage behavior when fault is occurred in (a) location 2, and (b) location 3 . . . . .	34
4.14	Instantaneous active power behavior when fault is occurred in (a) location 2, and (b) location 3 . . . . .	35
4.15	Voltage differential behavior when fault is occurred in (a) location 2, and (b) location 3 . . . . .	35
4.16	Positive sequence line-ground impedance behaviors when the fault is oc- curred in location 2, the dashed arrows represent the movement direction .	36
4.17	Closer look in positive sequence line-ground impedance behavior when the fault is occurred in (a) location 2 and (b) location 3 . . . . .	36
4.18	Proposed method for detecting the faulty section within a feeder . . . . .	37
4.19	(a) and (c) show the peak current and the instantaneous active power be- havior in the collection point for 4 kHz sampling frequency, while (b) and (d) are for 10 kHz sampling frequency . . . . .	38
4.20	Current harmonic spectrum in the collection point for 4 kHz sampling fre- quency . . . . .	39
4.21	Current harmonic spectrum in the collection point for 10 kHz sampling frequency . . . . .	40
4.22	(a), (c), and (e) show the peak current, the instantaneous active power, and the positive sequence line-ground impedance behavior in feeder 1 for 4 kHz sampling frequency, while (b), (d), (f) are for 10 kHz sampling frequency .	41
4.23	(a) the peak current behavior, (b) the instantaneous active power behavior in the collection point . . . . .	42
4.24	Current harmonic spectrum in the collection point . . . . .	43
4.25	(a) the peak current behavior, (b) the instantaneous active power behavior, (c) the positive sequence line-ground impedance behavior in feeder 1 . . . .	44
4.26	(a) the peak current behavior, (b) the instantaneous active power behavior in the collection point . . . . .	45
4.27	Current harmonic spectrum in the collection point . . . . .	46
4.28	(a) the peak current behavior, (b) the instantaneous active power behavior, (c) the positive sequence line-ground impedance behavior in feeder 1 . . . .	47
4.29	(a) the peak current behavior, (b) the instantaneous active power behavior in the collection point . . . . .	48
4.30	Current harmonic spectrum in the collection point . . . . .	49

4.31	(a) the peak current behavior, (b) the instantaneous active power behavior, (c) the positive sequence line-ground impedance behavior in feeder 1 . . . .	50
4.32	(a) the peak current behavior, (b) the instantaneous active power behavior in the collection point for 5 MW turbines . . . . .	51
4.33	(a) the peak current behavior, (b) the instantaneous active power behavior in the collection point for 1.5 MW turbines . . . . .	51
4.34	Current harmonic spectrum in the collection point for 5 MW turbines . . .	52
4.35	Current harmonic spectrum in the collection point for 1.5 MW turbines . .	53
4.36	(a) the peak current behavior, (b) the instantaneous active power behavior, (c) the positive sequence line-ground impedance behavior in feeder 1 for 5 MW turbines . . . . .	54
4.37	(a) the peak current behavior, (b) the instantaneous active power behavior, (c) the positive sequence line-ground impedance behavior in feeder 1 for 1.5 MW turbines . . . . .	55
A.1	A typical wind turbine power curve . . . . .	62
A.2	$C_p$ - $\lambda$ curve for different $\beta$ . . . . .	62
A.3	Simple $dq$ -axis representation in 2 poles PM machine . . . . .	63
A.4	Basic scheme of FOC for PMSG . . . . .	64
A.5	Phasor diagram of full torque control strategy . . . . .	65
A.6	PMSG control structure . . . . .	65

# List of abbreviations

WTG	wind turbine generator
FCG	full-scale converter generator
PMSG	permanent magnet synchronous generator
DSP	digital signal processing

# Chapter 1

## Introduction

*The first chapter has the main purpose to make an introduction to the presented report. It starts with a general presentation about wind energy technology and then the problem description is presented. In order to have a way to go through the research the scope and the limitations of the study are defined. The chapter ends with the report structure*

### 1.1 Background

For the last decade, world non-hydro renewable electricity generation has gradually increased from 1.7% of total electricity generation in year 2000 to 4.6% in year 2009 [2]. This number is expected to increase since many countries try to get 20% of their electricity generation from renewable resources by 2020 [3]. In Europe, 41% of new electricity generation installations during 2010 came from renewable energy [4]. This statistic shows a huge leap of EU countries to move away from fossil fuels and nuclear power.

Among renewable energy sources, wind energy is the fastest growing energy technology, due to its cost-competitiveness, reliability, and efficiency [5]. At the end of year 2000, there are 18 GW installed capacity of wind energy around the globe; by the end of year 2010 this number has increased tremendously to 195 GW [3]. With 44% of the global installed wind energy capacity in 2010, Europe is the global leader in wind energy technology [6].

The new wind energy technology has rapidly developed. For two decades, commercial wind turbine size increases exponentially, from a few hundreds kW in 1980s to 5 MW in the end of 2010 [7]. Beside increasing in size, the modern wind energy technology can also accommodate the wind speed variation in order to get better efficiency and controllability [8]. This wind turbine technology is called the variable-speed wind turbine.

The variable-speed wind turbine generator (WTG) type consists of induction generator with variable rotor resistance, doubly-fed induction generator (DFIG), and full-scale converter generator (FCG). Full-scale converter generator (or direct drive wind turbine) becomes popular because they have some advantages, i.e. wide range of speed operation, direct control of real and reactive power injection to the grid, and reduced mechanical stress [9]. In FCG, generator and grid are separated by a back to back converter which controls power exchange from generator to grid. Therefore, different types of generator and converter control schemes can be used in this topology [10,11]. Nowadays, permanent magnet synchronous generator (PMSG) is one of the best solutions for variable speed application. The advantages of using this generator type are DC excitation system is not needed, possibility to operate at low speed (no need of gearbox) for multi-pole generator, and generator speed is controlled by power electronic devices to maximize power extraction from wind.

In order to maximize the turbine efficiency without increasing the environmental impacts, wind farms are often located in remote sites, both offshore and onshore. If the wind farm connection exceeds 80 km offshore [12] or 500 km onshore [13], HVDC transmission system gives more economical benefit than HVAC transmission system. Voltage source converter high voltage DC (VSC-HVDC) system is a better option than the classical (Line Commutated Converter) HVDC system. Larger active and reactive power controllability, independent converter operation, high-speed switching converter, and small filter requirement are some of the benefits of using VSC-HVDC as opposed to classical HVDC [14]. Further in this study, the term HVDC will refer to VSC-HVDC.

The potential use of HVDC-connected wind farm with FCG should be guaranteed by a good protection system. By having a good protection system, faulty parts within the wind farm can be removed as quickly as possible while leaving the healthy parts as much as possible. As mentioned in [15, 16], short-circuit current (SCC) contribution from FCGs as well as VSC-HVDC can be limited (10% to 50% above normal current), which makes it difficult to detect a short-circuit fault within the wind farm. Fault detection in HVDC-connected wind farm with FCG become challenging task because the protection system standard for HVDC-connected wind farm with FCG is still hard to find.

## 1.2 Problem description

In this study, bolted three-phase short-circuit analysis was performed in the test case using PSCAD/EMTDC as depicted in Fig. 1.1. Wind farm configuration that is used in this study consists of 9 FCGs distributed in 3 feeders. Short-circuit fault points are placed in the point of common connection (PCC) of each FCGs.

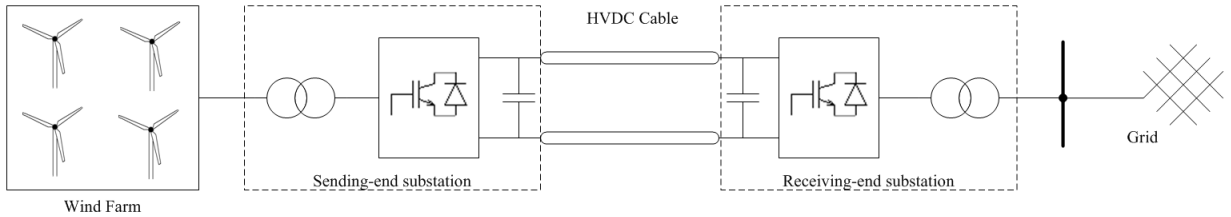


Figure 1.1: Wind farm with HVDC connection

Instantaneous voltage and current at the PCC of FCG as well HVDC are monitored. Digital signal processing, such as instantaneous peak value, instantaneous power, and discrete Fourier transform (DFT) analysis, are performed in the measured voltage and current. The results are then used to characterize faults in HVDC-connected wind farm with FCG that later used to determine the fault detection strategy and protection system topologies.

In order to do this study, FCG model and HVDC model were first developed using PSCAD/EMTDC. Both model should be able to limit their SCC contribution up to 10% above normal current.

## 1.3 Scope of the report

This report proposed the fault detection methods in the HVDC-connected wind farm with FCG. Both FCG and HVDC models are built in the PSCAD/EMTDC. In order to limit short-circuit current contribution from FCG and HVDC, the hysteresis current control is implemented in the grid-side converter of FCG and the sending-end HVDC converter.

Short-circuit analysis are also performed for different locations within the wind farm collection grid and different system conditions.

## 1.4 Limitations of the study

This study only investigates the behavior of the case system under three-phase fault. Although three-phase fault is not the most frequent grid fault, it is usually considered as the most severe fault condition, and uncleared faults may also lead to three-phase fault. System transients other than fault transient, such as system start up and fault clearance are not studied.

The delay time and loss optimization of the converters are not considered in this study, which means that the converter used in FCG and HVDC is assumed to be ideal. The potential of the system being asynchronous due to phase-lock loop (PLL) error is also not considered.

## 1.5 Structure of the report

This thesis studies three-phase short-circuit behavior of HVDC-connected wind farm with FCG in order to determine fault detection methods. The present report is structured in six chapters.

The second chapter discusses the wind farm configuration that is used in this study. Typical layout of wind farm and installed wind farm around the world are also presented to support the explanation.

The third chapter presents the modeling of the main components of the case study system. The grid-side FCG converter control strategy and the HVDC control strategy are investigated. The simulation results of the FCG model when subjected to a fault are also presented and discussed.

Short circuit analysis of the system is given in Chapter 4. Different simulation scenarios are also presented in this chapter.

In the fifth chapter digital signal processing (DSP) analysis of the measurements output is performed in order to characterize the three-phase short-circuit fault within the wind farm. Fault detection methods are also proposed in this chapter.

Finally, conclusions of the thesis and also ideas for the future work are pointed out in Chapter 6.

# Chapter 2

## Simulation setup

*In this chapter, the description of the case study system and the modeling of the main system components (FCG, HVDC, and cable) are discussed. The simulation result of a single FCG connected to the grid is also presented.*

### 2.1 Wind Farm Description

#### 2.1.1 Wind farm size and capacity

Many of the largest onshore wind farms are located in the USA, while the offshore ones are located in Europe [17, 18]. By the end of year 2010, Roscoe Wind Farm (Texas, USA) becomes the largest operational wind farm in the world at 781.5 MW and covering 404 km<sup>2</sup>. There are a total of 627 turbines installed, 209 of them having 1 MW rating, 160 wind turbines having 1.5 MW rating, and the rest having 2.3 MW rating [19].

The top ten installed offshore wind farms are given in Table 2.1. Six wind farms are located in the North Sea, while the rest are located in Irish Sea (Robin Rigg and Walney I) and Baltic Sea (Rødsand I & II). The average offshore wind farm capacity is 155.3 MW and the average location is 27.1 km from the shore [4]. By the end of year 2010, Thanet offshore wind farm is the biggest offshore wind farm in the world with 100 turbines giving 300 MW power. Total area of Thanet offshore wind farm is 35 km<sup>2</sup> with 500 meters space between turbines in a row and 800 meters between rows [20].

Table 2.1: The top ten installed offshore wind farms [17, 21]

Offshore wind farm	Capacity (MW)	Turbines Rating	Distance from shore (km)	Country
Thanet	300	100 × 3 MW	11.3 - 11.5	UK
Horns Rev II	209	91 × 2.3 MW	30	Denmark
Rødsand II	207	90 × 2.3 MW	8.8	Denmark
Lynn & Inner Dowsing	194	54 × 3.6 MW	5 - 9	UK
Walney I	184	51 × 3.6 MW	14.4	UK
Robin Rigg	180	60 × 3 MW	8	UK
Gunfleet Sands	172	48 × 3.6 MW	7	UK
Nysted (Rødsand I)	166	72 × 2.3 MW	10.8	Denmark
Belwind (Bligh Bank)	165	55 × 3 MW	46	Belgium
Horns Rev I	160	80 × 2 MW	14 - 20	Denmark

BARD offshore 1 wind farm will be the first wind farm to employ HVDC transmission

and is located 90-101 km from the shore. There are 80 x 5 MW turbines installed in the wind farm. As of December 2010, 15 out of 80 turbines have been installed [22].

## 2.1.2 Wind farm layouts

The common layouts of wind farm grid are string and star connected WTGs depicted in Fig. 2.1 [1]. The advantages of using string layout are uncomplicated cable installation,

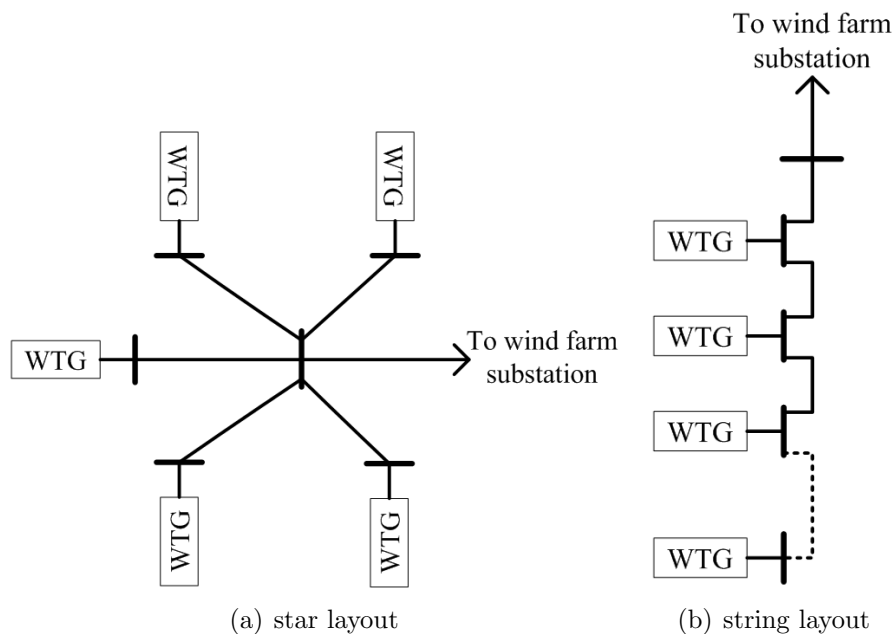


Figure 2.1: Offshore wind farm grid layout

and shorter cable length as compared to star connection. The drawbacks are the maximum WTGs that can be connected into a string depends on the current carrying capability of the cable used, and if there is cable failure within the string, all WTGs downward have to be disconnected. This problem can be solved using star connected WTGs, since in the star layout every WTGs connected directly to a collection point. By using star layout, lower rating equipment can be used [23]. In large offshore wind farm, combined string and star layout is often used, e.g. Horns Rev 1 offshore wind farm. As can be seen in Fig. 2.2, Horns Rev 1 has 80 WTGs placed in 10 rows. Two rows are grouped to form one radial feeder.

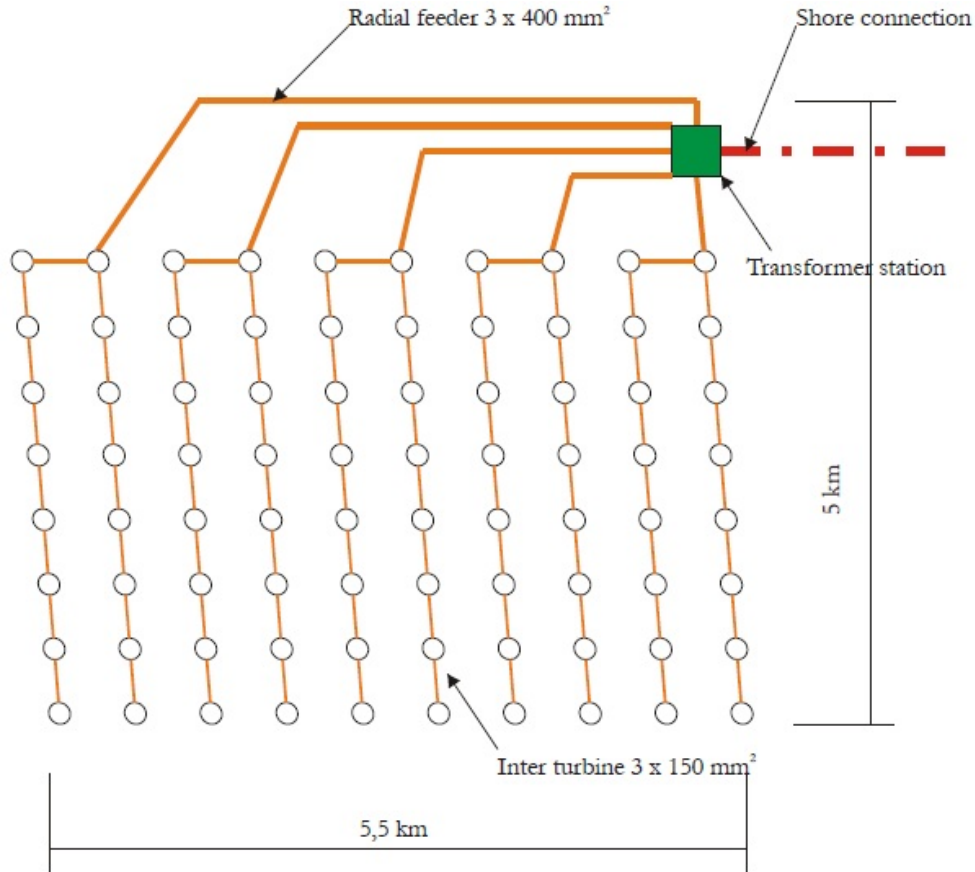


Figure 2.2: Horns Rev 1 layout [1]

### 2.1.3 Case study system

The case study is depicted in Fig. 2.3. In order to simplify the simulation and analysis, the case study system only consists of 9 WTGs placed in 3 rows. The distance between wind turbines is equal to 1 km, while between each rows is equal to 1.5 km. The rating of each wind turbines are 3 MW and the rating of the HVDC is equal to 27 MVA.

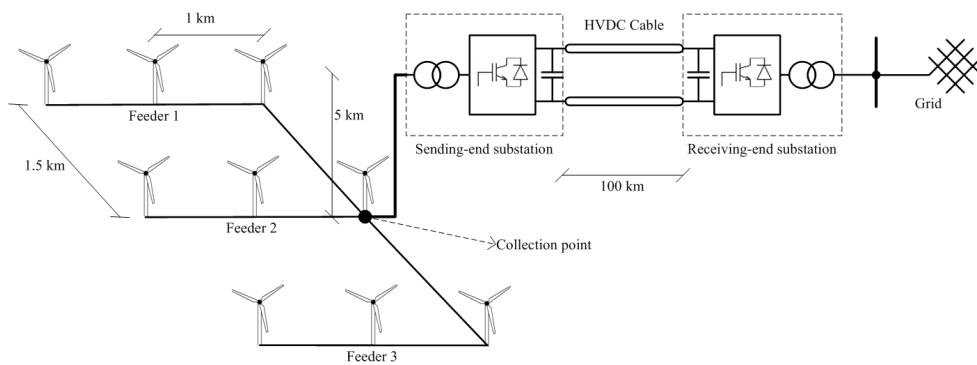


Figure 2.3: The case study system layout

All wind turbines in Fig. 2.3 are equipped with FCGs and connected to the 35 kV wind farm collection grid. Each FCG also has a 0.69/35 kV transformer to step-up the converter voltage. The DC voltage level used in the HVDC transmission system is 115 kV and the infinite grid voltage level is 130 kV.

The cable size connecting each part of the system is chosen based on its current rating and voltage rating. A 3 x 95 mm<sup>2</sup> XLPE cable is used to connect each FCG, while 5 km

of 3 x 400 mm<sup>2</sup> XLPE cable is used to connect the collection point to the HVDC station. The specification of the XLPE cable is given in Table 2.2.

Table 2.2: The ABB XLPE cable specification (Cu conductor) [24]

Cross-section area (mm <sup>2</sup> )	Current rating (A)	R (Ω/km)	L (mH/km)	C (μF/km)
95	275	0.193	0.69	0.17
400	515	0.047	0.57	0.28

## 2.2 Main Components Modeling

### 2.2.1 FCG model

Figure 2.4 shows the typical configuration of FCG with a permanent magnet synchronous generator (PMSG) and a six-pulse IGBT back to back converter. The generator-side converter is used to control the PMSG speed in order to maximize the wind power extraction by optimizing the tip speed ratio (TSR) of the wind turbine. Further explanation on aerodynamic, PMSG, and generator-side converter model can be found in Appendix A.

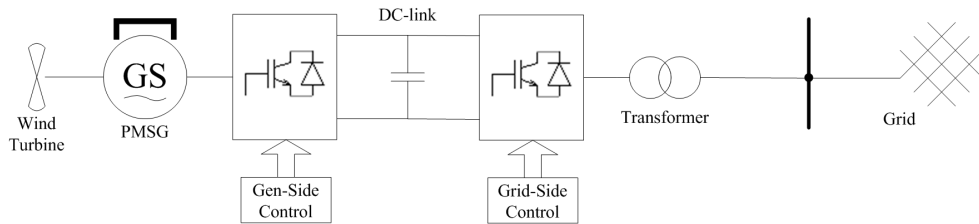


Figure 2.4: PMSG with back-to-back PWM converter

As explained in Appendix A, the speed control in the PMSG is usually realized by adjusting the output electrical torque with the mechanical torque from the wind turbine. The amount of the electrical torque depends on the permanent magnet flux, stator inductance, and stator current. Both flux and inductance are constant, while the stator current is controlled by the generator-side converter. The three phase stator current then rectified by the generator-side converter into DC quantity. If the wind speed is constant and the TSR of the wind turbine is at the optimum value, the current injected to the DC-link is also constant. Therefore, the FCG model depicted in Fig. 2.4 can be simplified into the one depicted in Fig. 2.5.

In the simplified FCG model, the aerodynamic, PMSG, and the generator-side converter are represented by a DC current source. The DC-link model and the grid side converter will be explained in the following subsection.

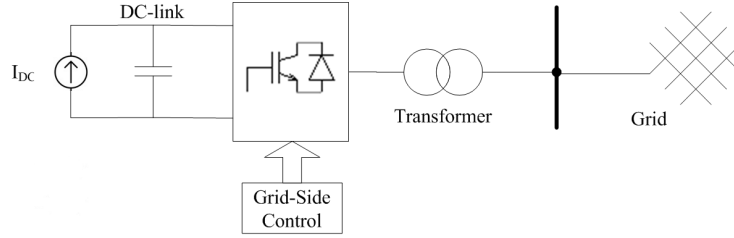


Figure 2.5: Simplified model of FCG

## DC-link model

**DC-link voltage level** The minimum value of DC voltage level in the back-to-back converter to avoid the sinusoidal pulse width modulation converter from being saturated is given as follows:

$$v_{DCmin} = \frac{2\sqrt{2} \cdot v_{l-l}}{\sqrt{3}} \quad (2.1)$$

where  $v_{DCmin}$  is the minimum DC voltage and  $v_{l-l}$  is the rms line to line voltage of the converter output [25]. It is common to use modulation index of the converter ( $m$ ) less than 0.9 for commercial application [26], therefore (2.1) become:

$$v_{DCmin} = \frac{2\sqrt{2} \cdot v_{l-l}}{\sqrt{3} \cdot m} \quad (2.2)$$

The value of  $v_{l-l}$  is usually assumed to be equal to the maximum allowable voltage (105 percent of the nominal voltage).

**DC-link capacitor** The current waveform flowing from the generator-side converter contains harmonics, which will introduce ripple in the voltage waveform. The control of the converter require a constant DC value, therefore it is needed to reduce the DC voltage ripple by using a capacitor. The amplitude of voltage ripple depends on the capacitance and switching frequency of the converter.

Selection of capacitor size is usually a trade-off between amplitude of voltage ripple and capacitor time constant [27]. A large capacitor can reduce DC-link voltage ripple, but it has slow response to the voltage change. On the other hand, a small capacitor allows fast control of DC-link voltage at the expense of higher DC-link voltage ripple. The DC time constant ( $\tau$ ) can be calculated as:

$$\tau = \frac{\frac{1}{2}C \cdot v_{DCN}^2}{S_N} \quad (2.3)$$

where  $v_{DCN}$  is the rated DC voltage, and  $S_N$  is the converter power rating. In the wind power technology applications, the capacitor size of back-to-back converter depends also on the fault ride-through (FRT) strategy of the FCG.

**FRT strategy** Power flow dynamic in the DC-link is shown by Fig. 2.6, where  $P_{Gen}$  is the power coming in to DC-link,  $P_{Grid}$  is the power coming out from the DC-link, and  $P_{Cap}$  is the power flowing to the capacitor ( $C$ ). During normal condition (assuming no power losses in DC-link),  $P_{Gen}$  is equal to  $P_{Grid}$  and there is no stored energy in the capacitor ( $P_{Cap}=0$ ). In the event of a grid fault,  $P_{Grid}$  is rapidly reduced ( $P_{Grid} \approx 0$ ) but due to the fact that mechanical dynamic is slower than electrical dynamic,  $P_{Gen}$  cannot be reduced

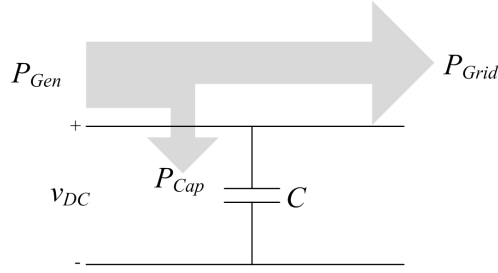


Figure 2.6: Power flow dynamic in the DC-link

quickly to keep  $P_{Gen}=P_{Grid}$ , therefore  $P_{Cap}$  is no longer zero. The power flow into capacitor can be written as follows:

$$v_{DC} \times C \frac{dv_{DC}}{dt} = P_{Gen} - P_{Grid} \quad (2.4)$$

This excess power from generator accumulates in the capacitor resulting in rapid increase in DC-link voltage. Overly DC-link voltage can destroy both capacitor and converter; therefore action must be taken to avoid system failures. In [28] several types of FRT strategies are discussed. In this study, only over-dimensioned DC-link capacitor and full power braking resistor are applied since both methods are giving the best dynamic performance [28]. Typical value of DC-link capacitor is approximately 55 to 270  $\mu\text{F}$  per horsepower or 70 to 400 mF for a 2 MW wind turbine [28].

The amount of energy dissipated in the braking resistor is controlled by IGBT. It is called full power braking resistor, because the energy dissipated in the resistor is equal to the energy generated by the wind. The schematic diagram of full power braking resistor is depicted in Fig. 2.7.

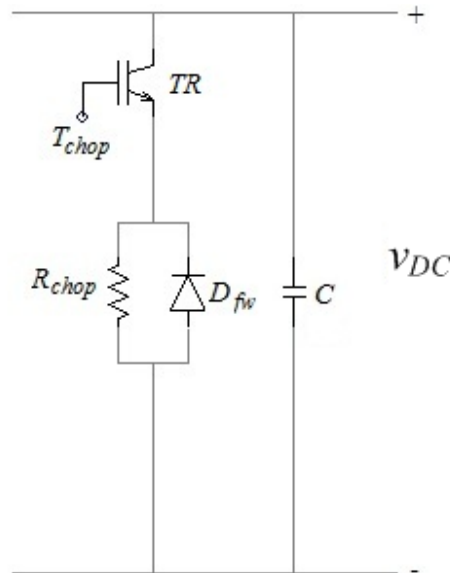


Figure 2.7: DC chopper schematic

In Fig. 2.7, the switch  $TR$  will conduct only if the DC-link voltage increase beyond the allowable limit (vary between 10 to 20 percent above the nominal voltage), and the power from generator is dissipated in the resistor  $R_{chop}$ . In the steady-state operation of FRT, the value of  $R_{chop}$  should be 1 per unit. There is no maximum limit of  $R_{chop}$ , but too large resistance will give large effects during fault clearance condition [29].

## Grid side converter model

The purpose of the grid-side converter is to interface active and reactive power exchange between DC-link and AC grid. As can be seen in (2.4), the DC-link voltage should be kept constant in order to maximize active power transfer to the grid, therefore DC-link voltage control is implemented in the grid-side converter. The reactive power support from FCG can be realized by controlling reactive current output from the grid-side converter [8,9].

The grid-side converter control is based on the  $dq$ -frame rotating synchronously with the AC grid. The most beneficial factor of using vector control is that the AC voltage and current are represented in constant vectors, therefore PI controller can be used to remove static errors of the control system hence simplify the controlling scheme. Clark and Park power invariant transformation is used to transform three-phase quantities into  $dq$ -axis representation. The transformation from stationary reference frame to rotational reference

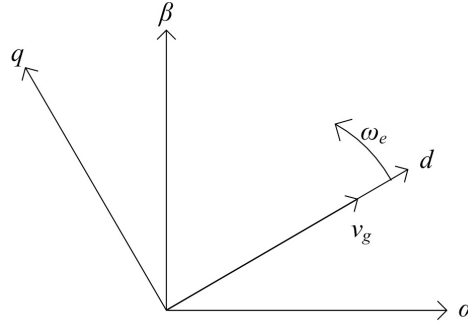


Figure 2.8: Transformation of axis for vector control

frame is shown in Fig. 2.8, where  $\omega_e$  represents the angular speed of AC grid.

The active power ( $p_g$ ) and reactive power ( $q_g$ ) transferred to the grid in  $dq$ -axis representation can be calculated as follows:

$$\begin{aligned} p_g &= \frac{3}{2}(v_{gd}i_{gd} + v_{gq}i_{gq}) \\ q_g &= \frac{3}{2}(v_{gq}i_{gd} - v_{gd}i_{gq}) \end{aligned} \quad (2.5)$$

where  $v_{gd}$  and  $v_{gq}$  represent the grid phase voltage magnitude in  $dq$ -axis, while  $i_{gd}$  and  $i_{gq}$  are the current that flow to the AC grid in  $dq$ -axis. In this study, the  $dq$  rotating frame is aligned with the grid voltage such that  $v_{gq} = 0$  and  $v_{gd} = |v_g|$ , therefore (2.5) becomes:

$$\begin{aligned} p_g &= \frac{3}{2}(v_{gd}i_{gd}) \\ q_g &= \frac{3}{2}(-v_{gd}i_{gq}). \end{aligned} \quad (2.6)$$

As can be seen in (2.6), the active and reactive power can be controlled independently by controlling the  $dq$  current that flows to the grid.

The grid-side converter control structure is depicted in Fig. 2.9. In this study, hysteresis current control is implemented to inject current into the grid. The diagram of hysteresis control can be seen in Fig. 2.10. The advantages of using hysteresis control are this control is simple to be implemented (control and PWM are combined), and it has quick response to reference change [30].

The converter current output can be limited by limiting one of  $i_{gdref}$  or  $i_{gqref}$  in Fig. 2.9 and adjusting the other. In this study,  $d$ -axis current is adjusted in order to allow an

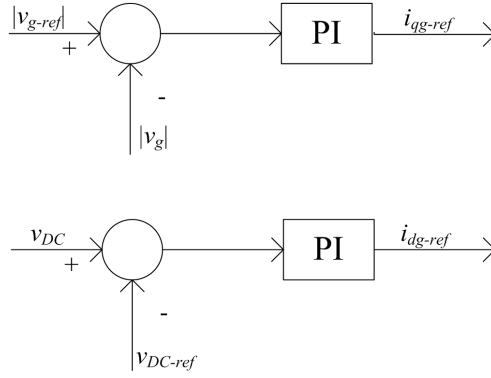


Figure 2.9: Grid-side converter control

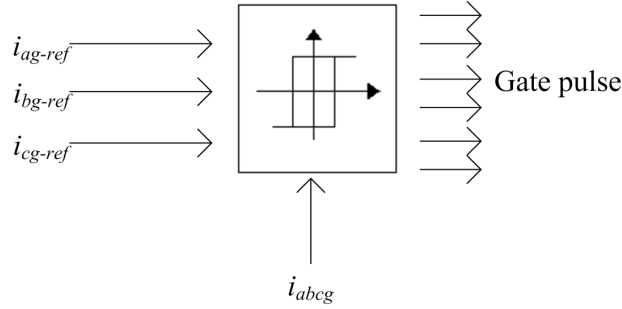


Figure 2.10: Hysteresis band current controller

increase of the reactive power transferred to the grid, as formulated in (2.7).

$$\begin{aligned}
 i_{gq-ref-max} &= i_{g-max} \\
 i_{gd-ref-max} &= \sqrt{i_{g-max}^2 - i_{gq-ref}^2}
 \end{aligned} \tag{2.7}$$

### FCG model implementation

In this subsection, FCG model behavior under fault is validated by comparing the results with the one presented in [16] and [9]. The test system is depicted in Fig. 2.11. Assumed that the line impedance is equal to  $0.15 + j 0.8 \Omega/\text{km}$  and the grid short-circuit capacity is equal to 9 MVA. Three-phase to ground fault is occurred in the grid busbar at 2.1 second. The simulation results can be seen in Fig. 2.12.

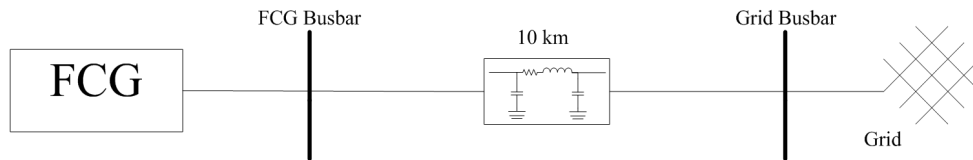
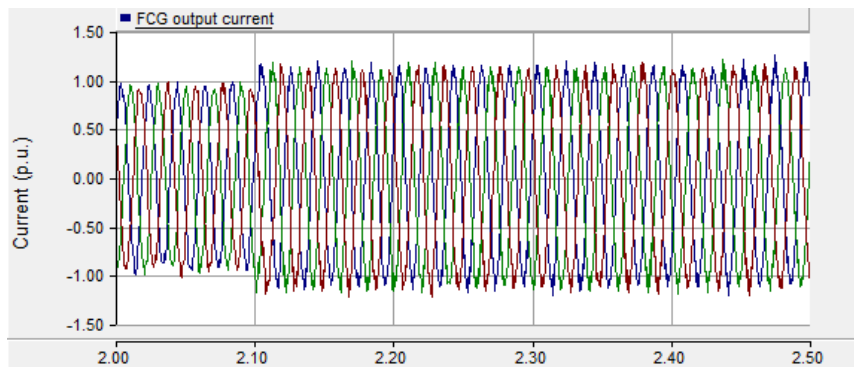


Figure 2.11: FCG test system

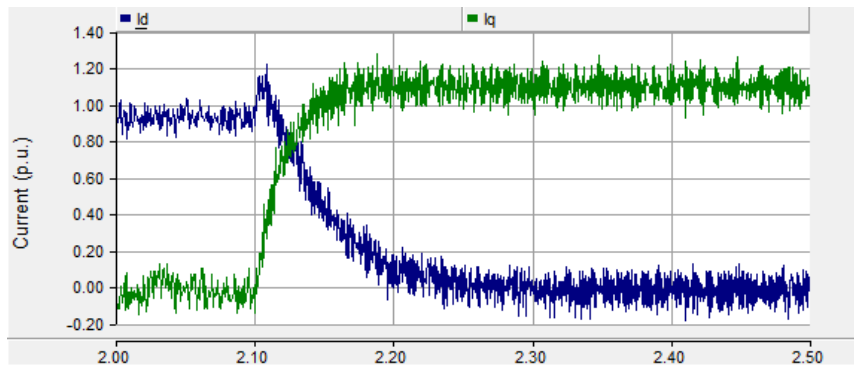
When fault occurred in the grid busbar, the grid voltage is decreased to zero while the FCG voltage drops to 0.18 p.u. due to the line impedance between the grid and FCG (depicted in Fig. ??). Since the voltage decreased, the active power injected from the FCG is also decreased. During the fault, the FCG voltage is less than its reference value (1 p.u.), therefore the  $q$ -axis current starts to grow as the result of PI-control as depicted in Fig. 2.12(b). Recalling (2.6), reactive power injection from the FCG is equal to the  $q$ -axis current, therefore in Fig. 2.12(d), the reactive power injected from the FCG during the

fault is increased. The aim of limiting the FCG short-circuit current contribution to 1.1 p.u is fulfilled by the model as can be seen in Fig. 2.12(a).

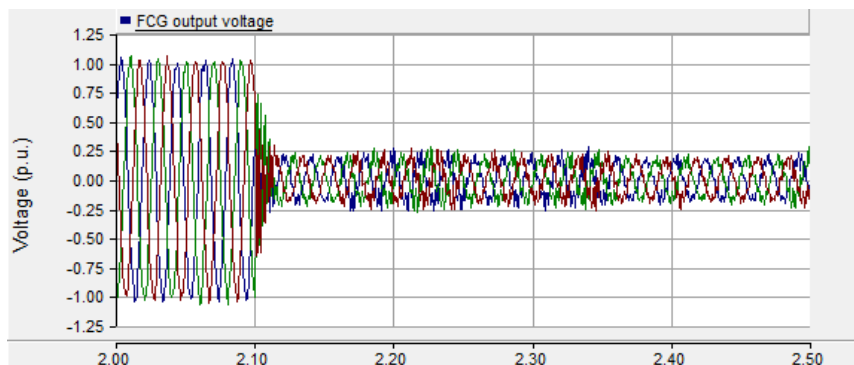
Figure 2.13 illustrated the simulation results for the same FCG test system but with reduced wind speed (5 m/s), so that the FCG produce only 20% of its rated power capacity. It can be seen in Fig. 2.13(a) that short-circuit current contribution from the FCG does not depend on the wind condition, since during fault only the reactive power is injected from the FCG.



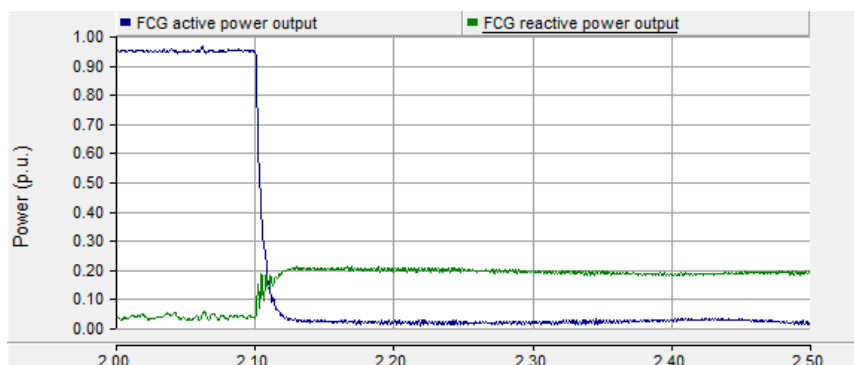
(a)



(b)

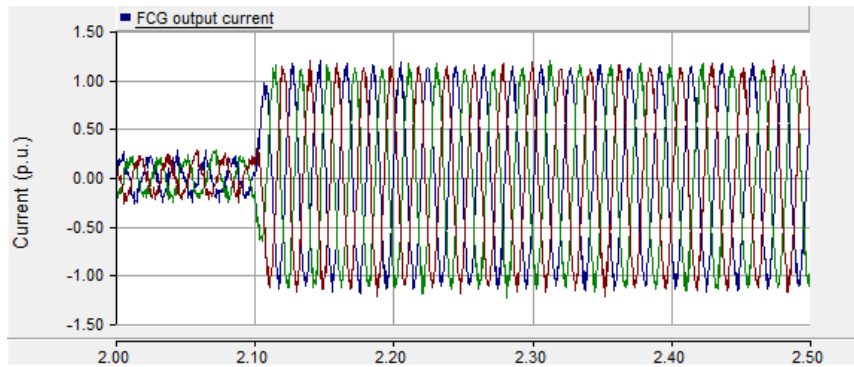


(c)

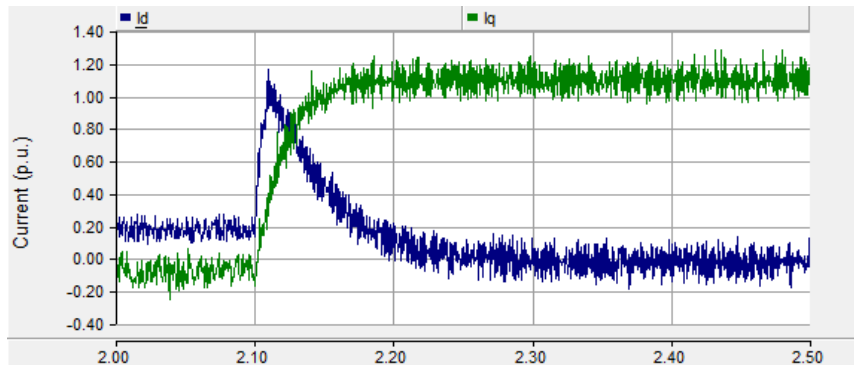


(d)

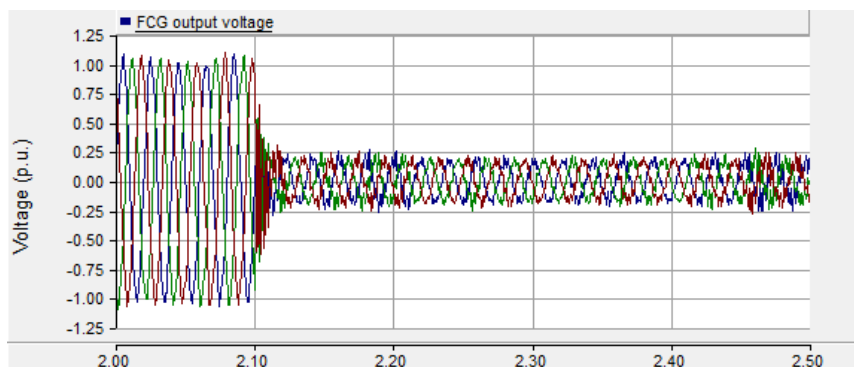
Figure 2.12: (a) Instantaneous current measured in FCG busbar, (b) dq-axis current measured in FCG busbar, (c) Instantaneous voltage measured in FCG busbar, and (d) Active and reactive power measured in FCG busbar



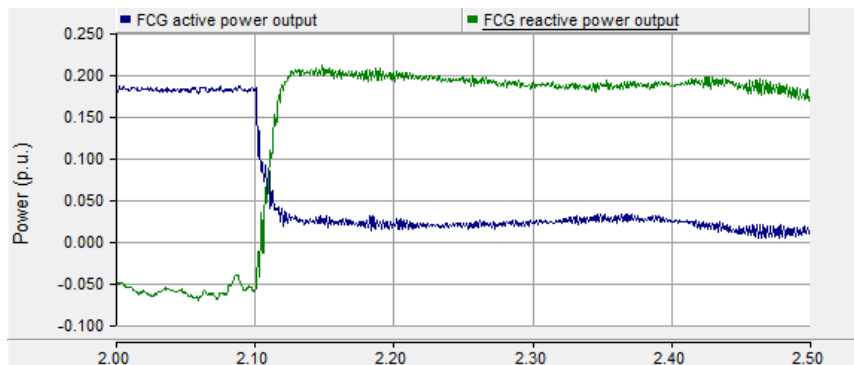
(a)



(b)



(c)



(d)

Figure 2.13: Measurement output during low wind condition:(a) Instantaneous current measured in FCG busbar, (b) dq-axis current measured in FCG busbar, (c) Instantaneous voltage measured in FCG busbar, and (d) Active and reactive power measured in FCG busbar

## 2.2.2 HVDC model

The VSC-HVDC transmission system is primarily composed of two converter stations and DC cables as depicted in Fig. 2.14. Each converter station consist of an IGBT-VSC, phase

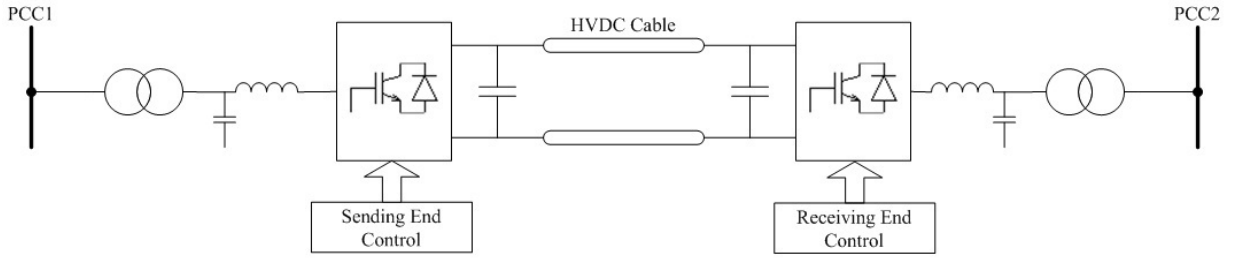


Figure 2.14: VSC-HVDC transmission system

reactor, filter, and transformer [27].

In this study, the sending-end HVDC (SE-HVDC) converter station is connected to the wind farm collection grid, while the receiving-end HVDC (RE-HVDC) converter station is connected to the main AC grid. The SE-HVDC converter station is used to maintain the wind farm voltage and frequency, while the RE-HVDC converter station is used to control HVDC voltage level and reactive power flow to the main AC grid [31]. The SE-HVDC converter control is realized using sinusoidal PWM. The sinusoidal reference waveform has constant frequency and the magnitude is set so that the output voltage of SE-converter station equals to wind farm grid nominal voltage. The RE-converter is using the same control strategy as in the grid-side converter of FCG model which has been explained in section 2.2.1 [9].

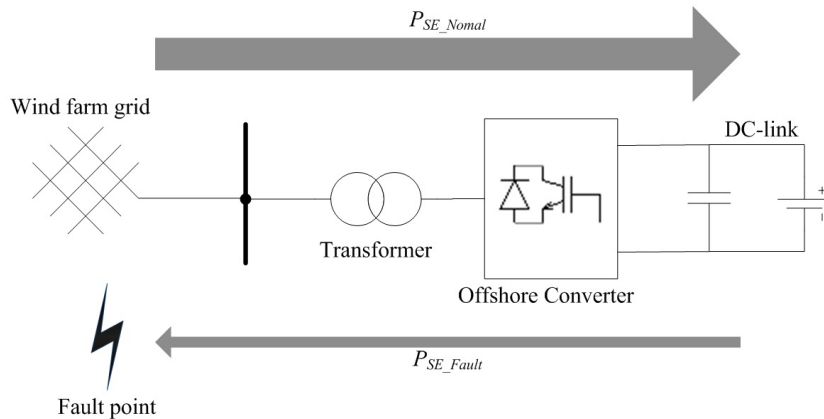


Figure 2.15: During normal condition, active power flows from wind farm grid to DC-link, while during fault in the wind farm grid, active power flows in reverse direction

When fault occurred in the wind farm collection grid, the magnitude and direction of the active power flow measured in the SE-HVDC converter is changed as depicted in Fig. 2.15. Since the short circuit current contribution from the HVDC is defined and restrained, the SE-HVDC converter switch mode from voltage-regulated mode in normal condition to current-regulated mode during fault [15].

Figure 2.16 depicted the control mode alteration method in the SE-HVDC converter station. In Fig. 2.16, instantaneous voltage ( $v_{SE-HVDC}$ ) and current ( $i_{SE-HVDC}$ ) are measured in the connection point of the SE-HVDC converter station. If the measured peak current reach more than its threshold value (10% above nominal current) or the measured

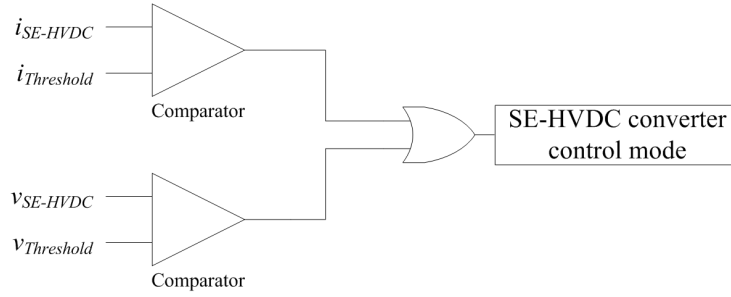


Figure 2.16: SE-HVDC converter control mode switch is implemented by sensing the instantaneous voltage ( $v_{SE}$ ) and current ( $i_{SE}$ ).

peak voltage goes below its threshold value (70% of nominal voltage), then the SE-HVDC converter alters from voltage source mode to current source mode. When current source mode is activated, SE-HVDC converter uses the same control strategy as explained in section 2.2.1.

### 2.2.3 Cable model

For a short AC transmission line (less than 35 km), pi line section model is used to represent the transmission line. This is because for a short transmission line, the propagation time is less than a simulation time step [32]. The pi line section model is depicted in Fig. 2.17. In PSCAD/EMTDC, coupled pi line section component is used in this study, which means

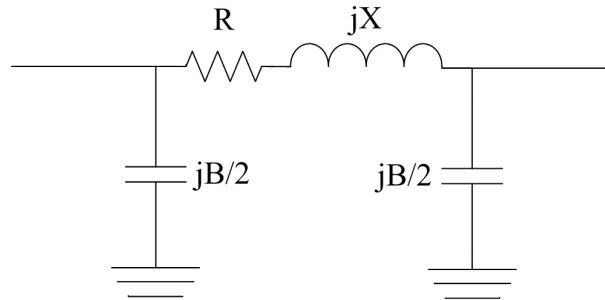


Figure 2.17: Pi line section model

that the conductor voltages are always measured to true ground or earth [33]. The line data used in this study are given in Table 2.2.

The DC cable used in the HVDC system uses frequency dependant (phase) model to represents the DC cable. By using the frequency dependant (phase) model, the frequency response of a cable is duplicated using curve fitting method [32]. The geometry of the DC cable is given in Fig. 2.18.

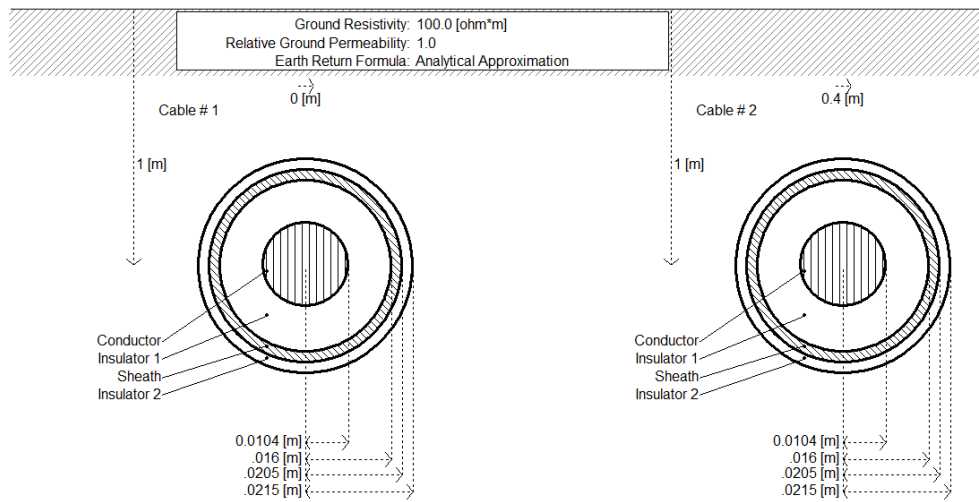


Figure 2.18: HVDC cable geometry implemented in PSCAD/EMTDC

# Chapter 3

## Short-Circuit Studies

*The chapter starts with a briefly introduction about short-circuit studies. Next the short-circuit simulation results for different fault scenarios are discussed. Hand calculation of the fault current is also presented.*

### 3.1 Short-circuit studies

Short-circuit studies are carried out to gather information of the system under fault. These information used to design the protective scheme of the system and to obtain the rating of electrical apparatus (e.g.: cables, circuit breakers, transformers) used in the system.

Unlike AC machines, during fault, converter used in FCG and HVDC can be represented as current source [34]. As depicted in Fig. 3.1, the left-side of busbar  $i$  represents the FCG/HVDC, while the right-side of busbar  $i$  represents the synchronous generator (SG) under fault condition. When three-phase fault occurs in busbar  $i$ , short-circuit current contribution from SG depends on the equivalent impedance of the generator and the line between the generator and the busbar, while the short-circuit current contribution from FCG/HVDC is known and limited to 10% above nominal current. Under unbalance short-circuit faults, e.g. single phase to ground fault or line to line fault, the converter control is designed to continue to supply balanced three-phase currents irrespective of the degree of its voltage unbalance. In both balance and unbalance fault, the current control strategy is normally very fast so that short-circuit current contribution from FCG/HVDC does not change with time.

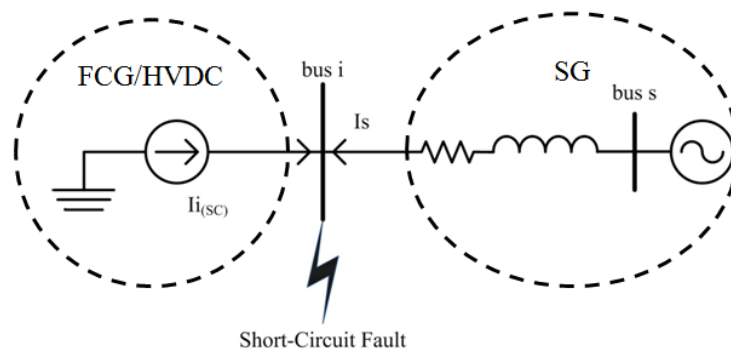


Figure 3.1: Equivalent circuit of FCG/HVDC and synchronous generator (SG) during short-circuit fault

## 3.2 Simulation scenarios

Three-phase to ground fault for different fault locations in the wind farm collection grid were simulated. The fault is located in the PCC of the FCG as can be seen in Fig. 3.2 and has a resistance ( $R_{fault}$ ) of  $0.001 \Omega$ . The fault location 1 is defined as the fault occurred in the terminal of FCG 01, and location 2, 3, 4, 5, 6 respectively.

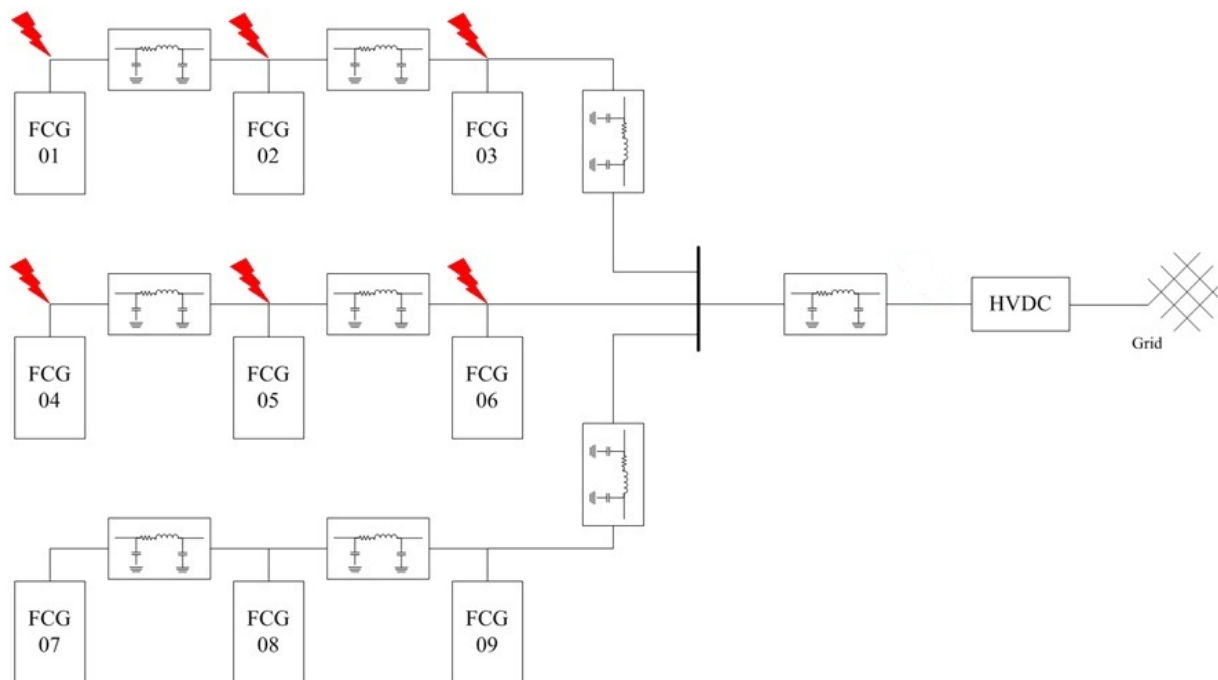


Figure 3.2: Different fault locations for the short-circuit simulation

As the base case, all FCGs are producing power at their rated capacity and short-circuit current contribution from FCG and HVDC are equal to 10% above their rated current.

## 3.3 Simulation results

Typical protection zones in wind farm are explained in [35]. Since the fault is assumed to occur only in the wind farm collection grid, the affected zones are the collector feeder relay zone (feeder line) and the collector bus relay zone (collection point) as can be seen in Fig. 3.3. In the collection point, the concern is to investigate the behavior of the currents exchange from the wind farm feeder to the HVDC station. While in the feeder line, current flowing from each FCG are observed.

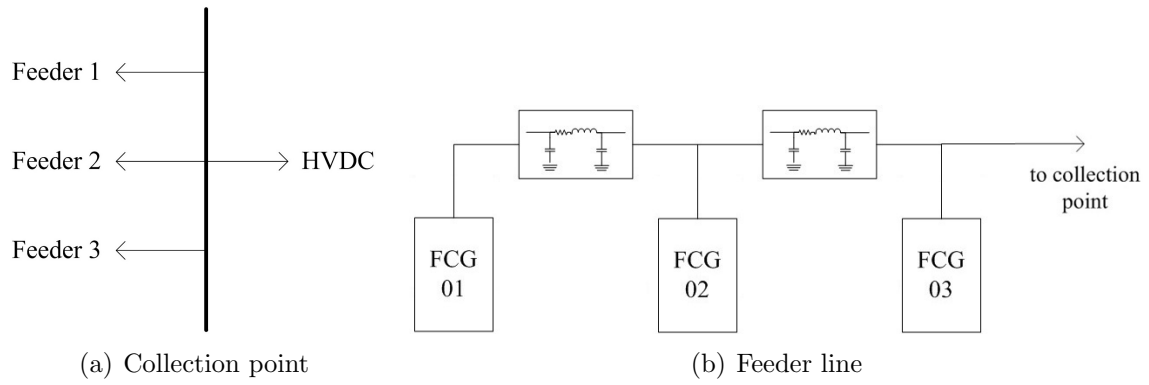


Figure 3.3: Two observation points in the case system

### 3.3.1 Collection point

If the fault occurs in feeder 1, currents are flowing from feeder 2, feeder 3, and HVDC into feeder 1, as can be seen in Fig. 3.4. The amount of the current flowing into feeder 1 can

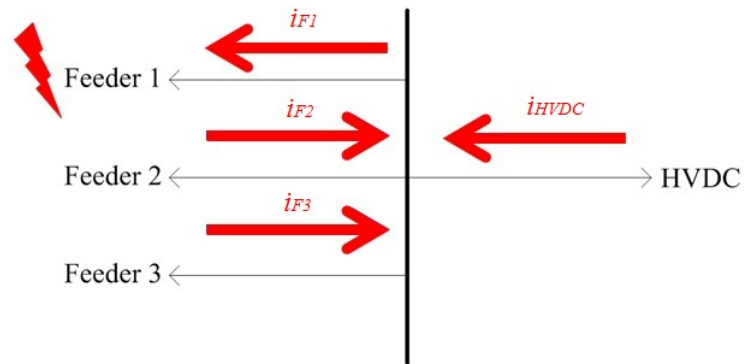


Figure 3.4: Current behavior when fault occurs in feeder 1

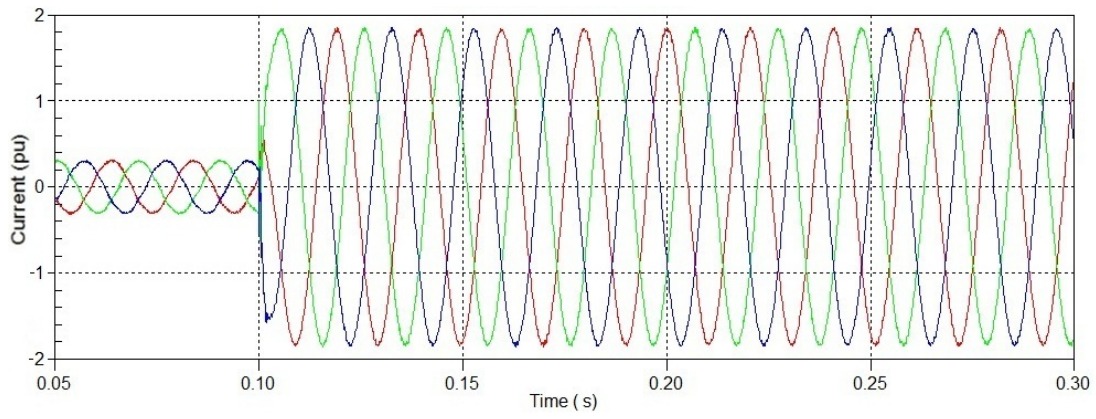
be calculated as follows:

$$\begin{aligned}
 i_{HVDC} &= 1.1 \text{ p.u.} \\
 i_{F2} &= \frac{1}{3} \times 1.1 \text{ p.u.} \\
 i_{F3} &= \frac{1}{3} \times 1.1 \text{ p.u.} \\
 i_{F1} &= 1.8333 \text{ p.u.}
 \end{aligned} \tag{3.1}$$

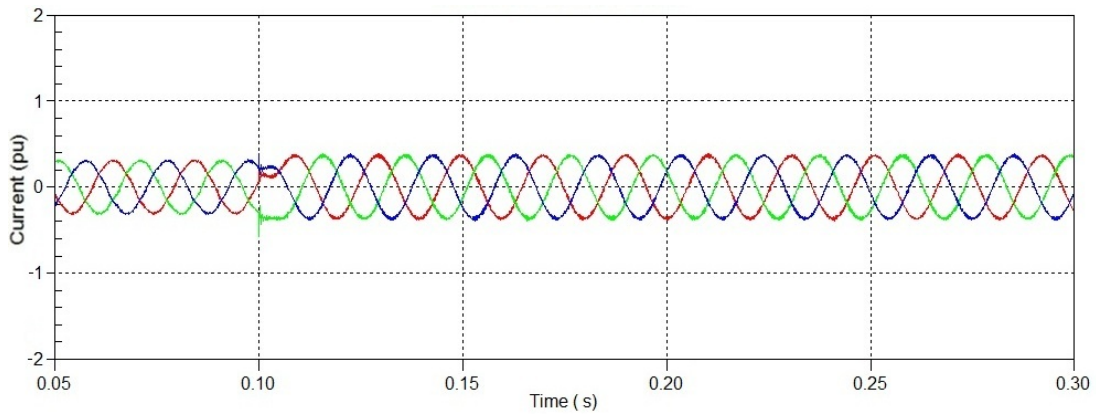
where  $i_{F1}$ ,  $i_{F2}$ ,  $i_{F3}$ , and  $i_{HVDC}$  are the current measured in feeder 1, feeder 2, feeder 3, and HVDC feeder respectively. Current measured in feeder 1 (Fig. 3.5(a)) is increased from 0.33 p.u. during normal condition (all FCGs are producing power at their rating) to 1.83 p.u. during fault.

If the fault occurs in feeder 2 (depicted in Fig. 3.6), the current flows into feeder 2 can be calculated as follows:

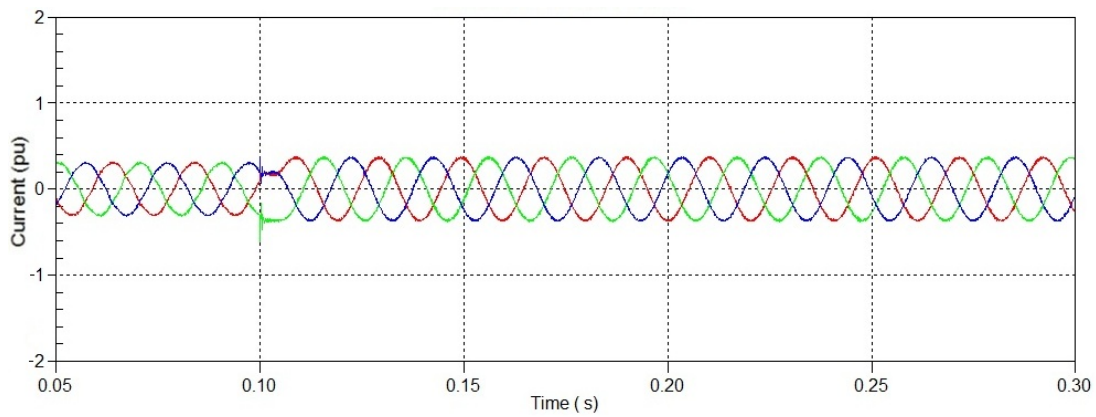
$$\begin{aligned}
 i_{HVDC} &= 1.1 \text{ p.u.} \\
 i_{F1} &= \frac{1}{3} \times 1.1 \text{ p.u.} \\
 i_{F3} &= \frac{1}{3} \times 1.1 \text{ p.u.} \\
 i_{F2} &= 1.8333 \text{ p.u.}
 \end{aligned} \tag{3.2}$$



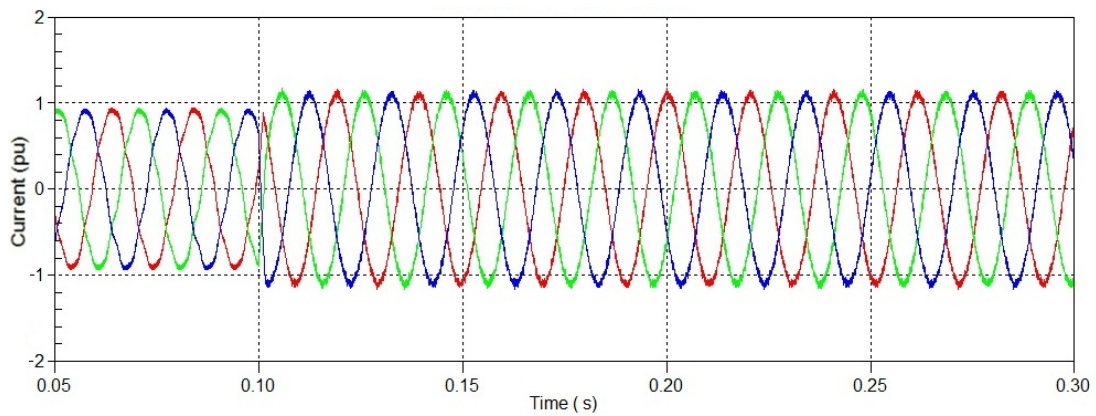
(a)



(b)



(c)



(d)

Figure 3.5: Current flowing in: (a) feeder 1; (b) feeder 2; (c) feeder 3; and (d) HVDC feeder

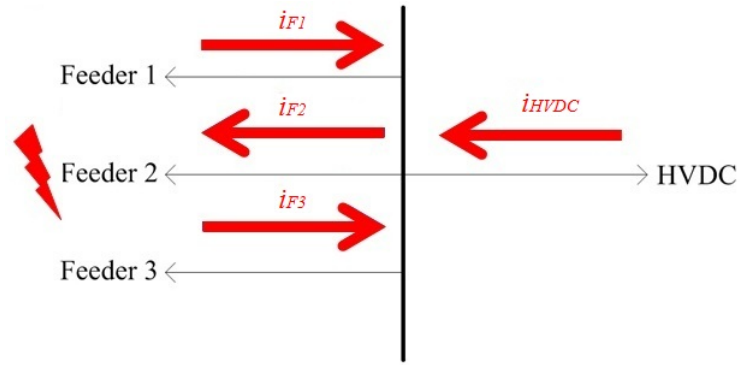
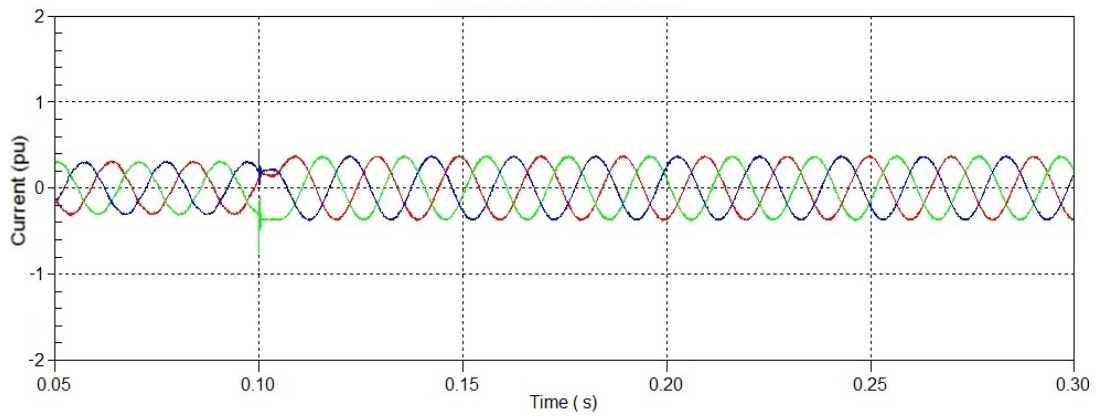


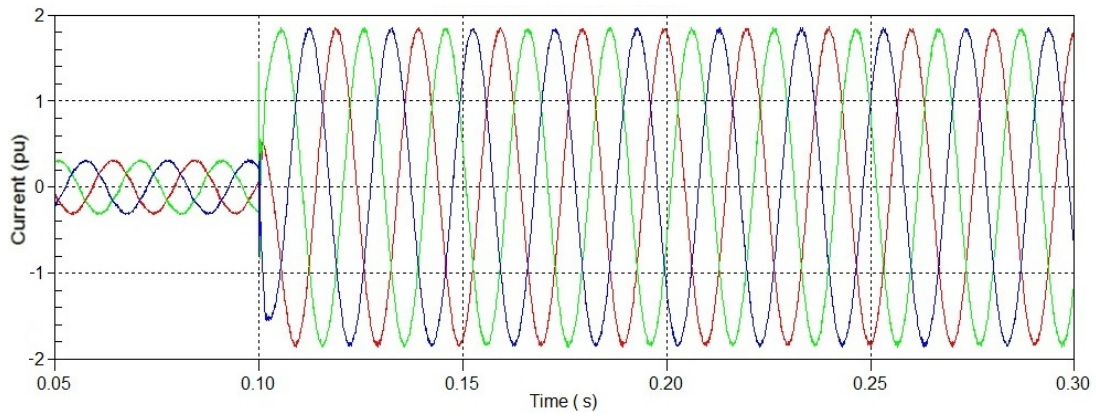
Figure 3.6: Current behavior when fault occurs in feeder 2

Current measured in feeder 2 (Fig. 3.7(b)) is increased from 0.33 p.u. during normal condition to 1.83 p.u. during fault.

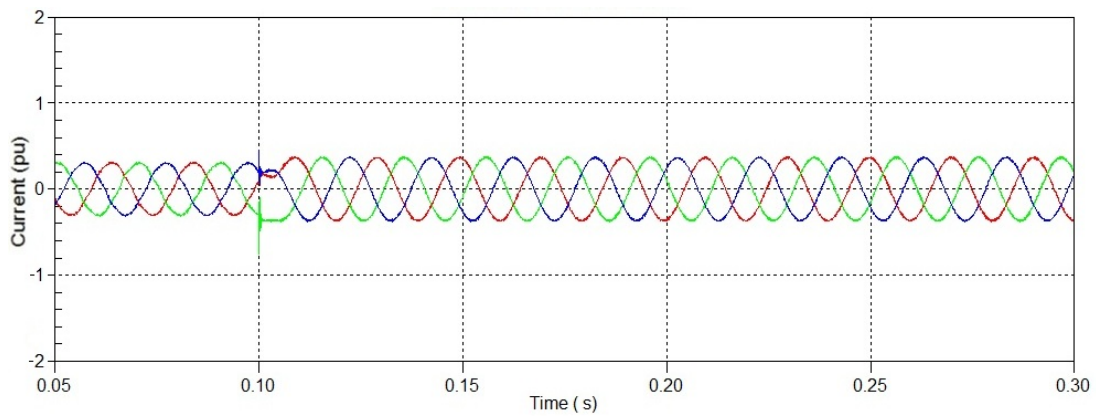
As can be seen in Fig. 3.5 and Fig. 3.7, current flows into the faulty feeder equals 1.83 p.u. which is the sum of short-circuit current contribution from healthy feeders and HVDC. Discontinuity in the current waveform of the healthy feeders occur due to the FCG status change from full active power support to full reactive power support.



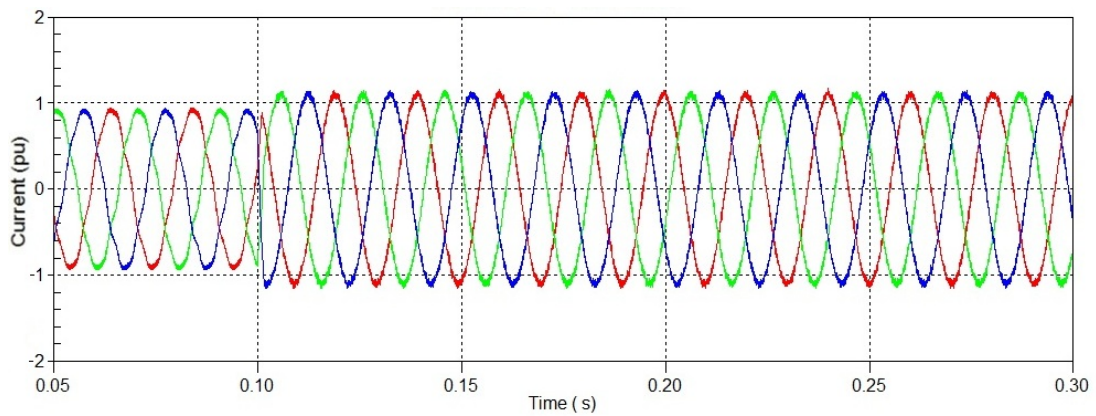
(a)



(b)



(c)



(d)

Figure 3.7: Current flowing in: (a) feeder 1; (b) feeder 2; (c) feeder 3; and (d) HVDC feeder

### 3.3.2 Feeder line

If fault is located in location 1 (as depicted in Fig. 3.8), short-circuit current contribution

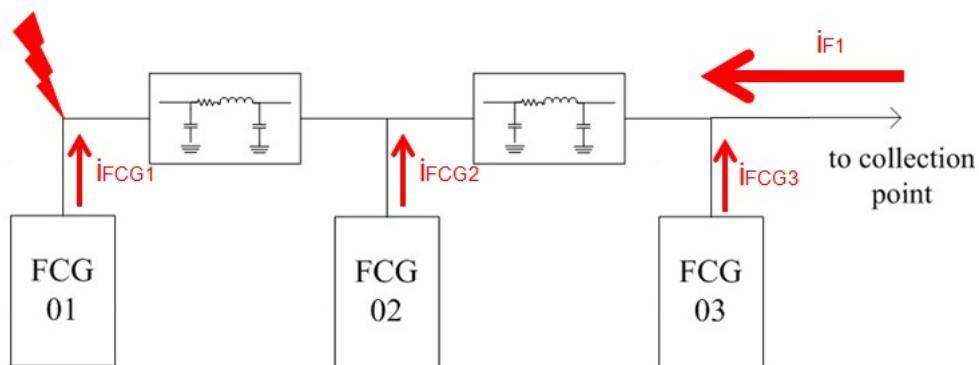


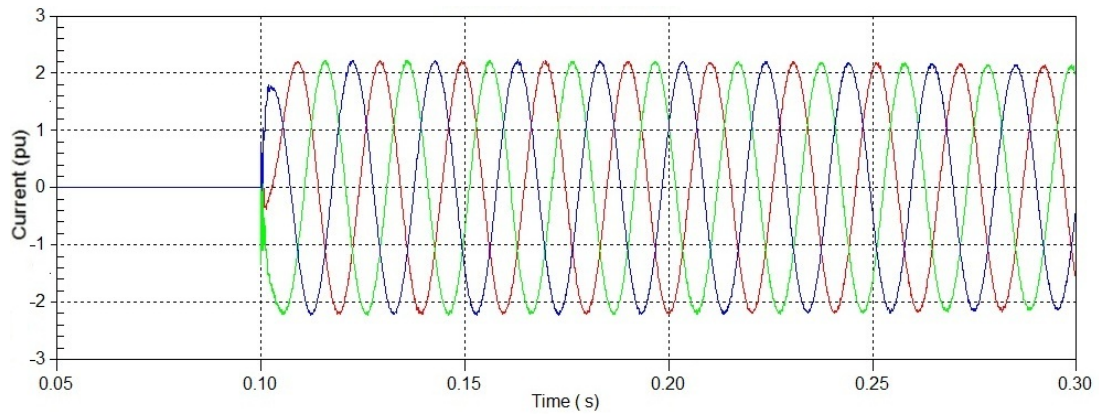
Figure 3.8: Current behavior when fault is in location 1

from each FCGs are 10% above their nominal current, therefore fault current ( $i_{Fault}$ ) can be calculated as follows:

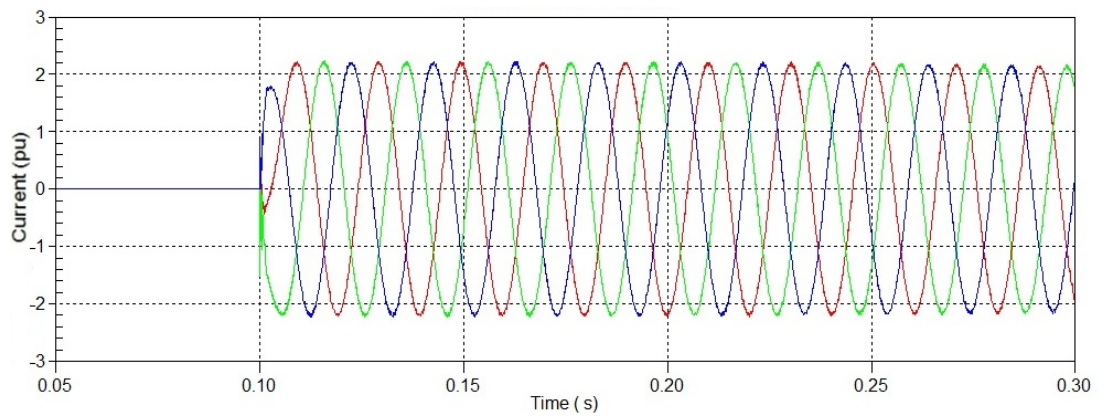
$$\begin{aligned}
 i_{F1} &= 1.8333 \text{ p.u.} \\
 i_{FCG} &= \frac{1}{9} \times 1.1 \text{ p.u.} \\
 i_{Fault} &= 2.2 \text{ p.u.}
 \end{aligned} \tag{3.3}$$

where  $i_{FCG}$  is the short-circuit current contribution from FCG.

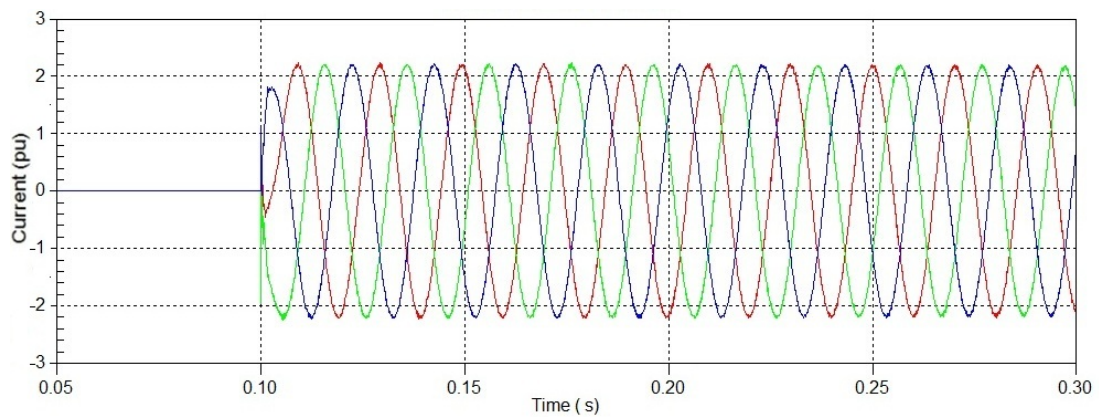
The fault current when fault occurred in location 1 as well as location 2 and 3 is shown in Fig. 3.9. Since the converter can be represented as current source, the amounts of short circuit current contribution from FCGs are not depending on the line impedance. Therefore, the calculated fault current in (3.3) is also valid for the other fault locations. This can be seen in Fig. 3.9 where all the fault current for three different locations along feeder 1 are having the same magnitude. In the other words, the fault current can be calculated as the sum of short-circuit current contribution from wind farm and HVDC.



(a)



(b)



(c)

Figure 3.9: Fault current when fault is located in: (a) location 1; (b) location 2; and (c) location 3

### 3.4 Fault clearing time

During a short-circuit fault, the thermal energy is developed in the cable and depends on the short-circuit magnitude and duration. The maximum short-circuit current allowed to flow in the cable due to thermal limitation can be formulated as follows [24]:

$$i_{sh} = \frac{i_{1s}}{\sqrt{t_{sh}}} \quad (3.4)$$

where  $i_{sh}$  is the short-circuit current [kA] during time  $t_{sh}$ ,  $i_{1s}$  is the short-circuit rating during 1 second (provided in [24]), and  $t_{sh}$  is the short-circuit duration [second]. For XLPE insulated conductors, the maximum allowable short circuit temperature is 250°C.

From the previous subsection, short-circuit current that flows in the wind farm collection grid is equal to 2.2 p.u. or equal to 0.979 kA, inserting this into (3.4), the maximum fault clearing time for the feeder line cable is equal to 1.7 minute. The short-circuit current contribution from HVDC is 1.1 p.u. or equal to 0.490 kA, the maximum fault clearing time for the cable connecting collection grid to the SE-HVDC terminal is equal to 2 hours.

# Chapter 4

## Fault Detection

*The voltage and current signals from the PSCAD/EMTDC simulations are further analyzed in MATLAB. The signal processing methods that are used in the digital protective relays are explained in this chapter. The signal analysis results for different simulation scenarios and the proposed fault detection methods are presented. In the end of this chapter, the signal processing results for different system conditions are also presented.*

### 4.1 Digital protective relaying

The development of microprocessor in early 1970s has opened the possibility of using computers in power system protection. In the beginning of 1980s, the first digital or numerical protective relays were implemented in the system [36]. By using microprocessor, one or more protective functions, i.e. voltage, overcurrent, distance protection, and differential protection, can be implemented in a single protective device resulting in reduced panel space. The modern digital protective relays also include additional functions such as fault reporting and data recording, remote communication, and self-calibration [37]. The disadvantages of digital protective relays as mentioned in [38] are short lifetime because of rapid technology development makes the relays disused quickly, easily affected by power system transients, and sophisticated relays need trained-personals to handle.

The main difference of digital and conventional relays is in the method of signal processing. In digital relays, analog signals are sampled into digital signals before processed, while in conventional relays, this digitations method does not occur, and the analog signals are directly connected to the electromagnetic winding or electronic circuits. The basic block



Figure 4.1: Block diagram of digital protective relay

diagram of digital relay is depicted in Fig. 4.1.

The signal conditioning part consists of transducers and analog filters. The most common transducer used is the instrument transformers, i.e. current transformers (CT), voltage or potential transformers (CT or PT), and capacitive voltage transformers (CVT). The analog signal from the measurement devices output then converted into digital signal (A/D conversion) by signal conversion part. Different method of A/D conversion can be found in [39] and [40].

The digitized signal then processed in digital signal processing (DSP) part. In this study, the DSP is done for one data window. Figure 4.2 illustrates the moving rectangular data window when new sample is included and the oldest one is discarded. The window

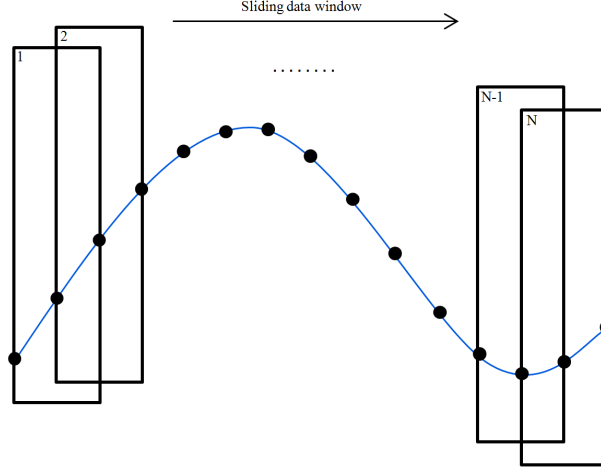


Figure 4.2: Sliding data window method

width used in this study is equal to one cycle of the power frequency (20 ms). The DSP method that are used in this study are instantaneous peak value, DFT analysis, instantaneous active power ( $p_{inst}$ ), differential value, and positive sequence line-ground impedance ( $z$ ) [37, 41, 42]. Instantaneous peak value ( $z_p$ ), DFT analysis ( $Z_k$ ), and differential value ( $z_{diff}$ ) are calculated using the following equations.

$$z_p = \text{maximum of } |z_k|_{k=0}^{N-1} \quad (4.1)$$

$$Z_k = \sum_{n=0}^{N-1} z_k e^{-j \frac{2\pi}{N} kn} \quad k = 0, \dots, N-1 \quad (4.2)$$

$$z_{diff} = z_{k+1} - z_k \quad k = 0, \dots, N-1 \quad (4.3)$$

where  $j$  denotes the imaginary unit,  $N$  is the number of the sample in one window, and  $z_k$  is the sampled signal. While instantaneous active power ( $p_{inst}$ ), is calculated from instantaneous value of phase current ( $i$ ) and voltage ( $v$ ) and given as follows:

$$p_{inst} = \frac{1}{N} \sum_{n=0}^{N-1} v \cdot i \quad (4.4)$$

The result of the DFT analysis in (4.2) is the signal spectrums. By using the fundamental phase current ( $I_{(1)}$ ) and voltage ( $V_{(1)}$ ), positive sequence line-ground impedance ( $Z$ ) can be calculated as:

$$Z = \frac{V_{(1)}}{I_{(1)}} \quad (4.5)$$

In this study, the short-circuit analysis results for different fault scenarios simulated in PSCAD/EMTDC are sampled and post-processed using MATLAB. Since the fault is balanced three-phase to ground fault, only phase A is considered for the post-processing. The results of the post-processing are discussed in the following sections.

## 4.2 Results and analysis

### 4.2.1 Collection point

The main objective of having the fault detection method in the collection point is to discriminate between the faulty and the healthy feeder. The measurement units (voltage and current meters) are placed in the incoming feeder (feeder 1, 2, and 3) and outgoing feeder (HVDC feeder), as depicted in Fig. 4.3.

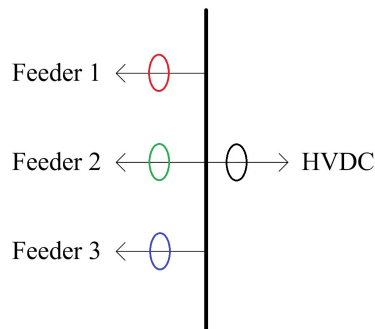


Figure 4.3: The ellipses indicate the measurement units (MUs) in the collection point

### Peak current behavior

As can be seen in Fig. 4.4, the peak current flowing into the faulty feeder has the same magnitude regardless the location of the fault. The peak current in the faulty feeder equals to 1.16 kA ( $\approx 1.83$  p.u.), while in the healthy feeders equals to 0.23 kA (10% above their normal current). Therefore the discrimination between faulty and healthy feeder can be achieved by observing the peak current during the fault.

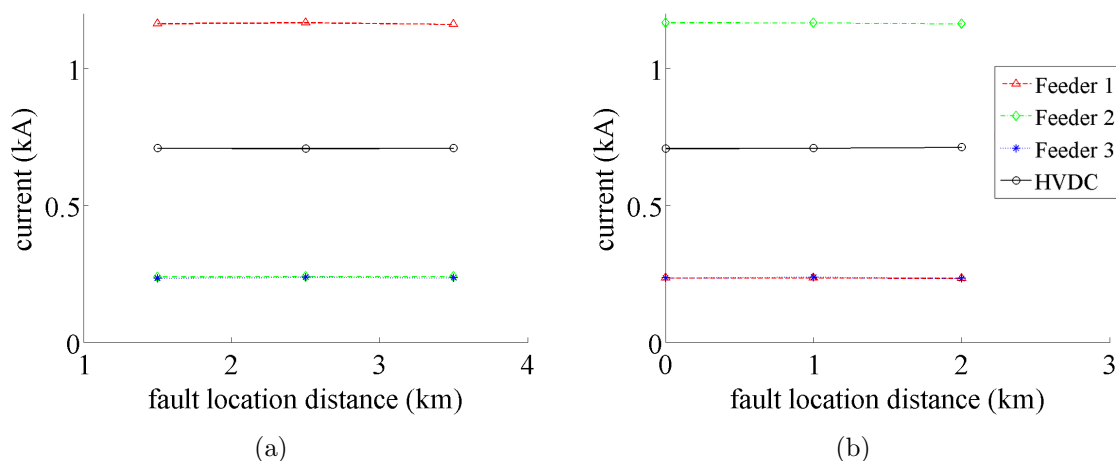


Figure 4.4: Peak current magnitude during fault located in (a) feeder 1, and (b) feeder 2

### Instantaneous active power behavior

When fault occurred in the system, the system voltage and the active power flow are reduced. The direction of the active power also changes toward the faulty point. As can be seen in Fig. 4.5(a), the direction of the instantaneous active power in the HVDC feeder and feeder 1 are changed after the fault occurs in feeder 1, while when the fault is occurred

in the HVDC terminal, there are no reverse direction of the instantaneous active power flow. The instantaneous active power behavior during the fault is shown in Fig. 4.6. By

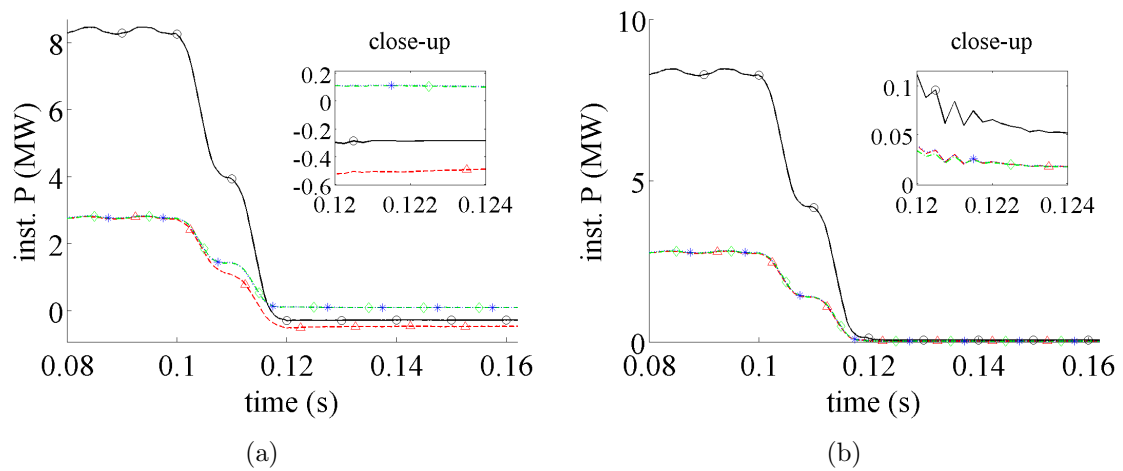


Figure 4.5: Instantaneous active power behavior when the fault is occurred in (a) location 1, and (b) SE-HVDC terminal

observing the instantaneous active power sign (flow direction), the faulty feeder can be identified.

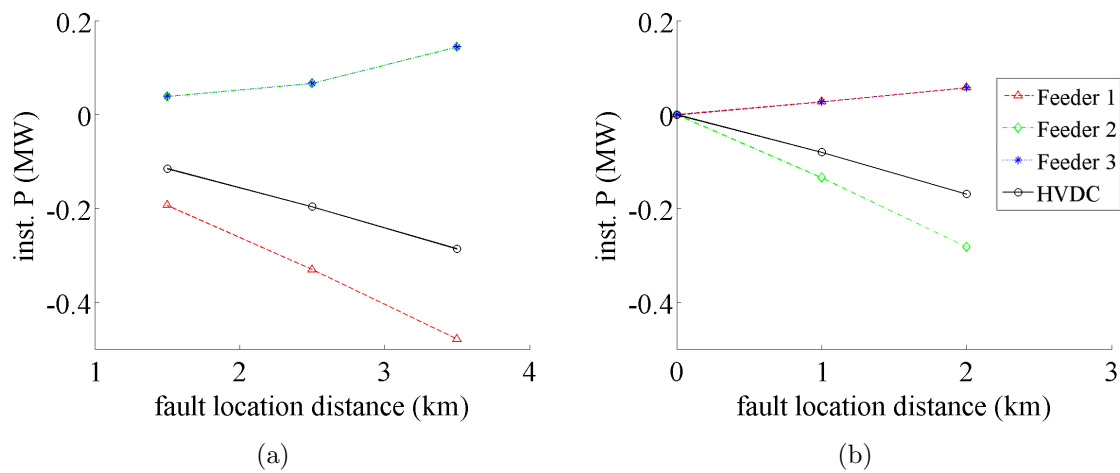


Figure 4.6: Instantaneous active power during fault in (a) feeder 1, and (b) feeder 2

### Current differential behavior

As can be seen in Fig. 4.7, the current differential signal is too noisy to be used to discriminate the faulty and healthy feeder.

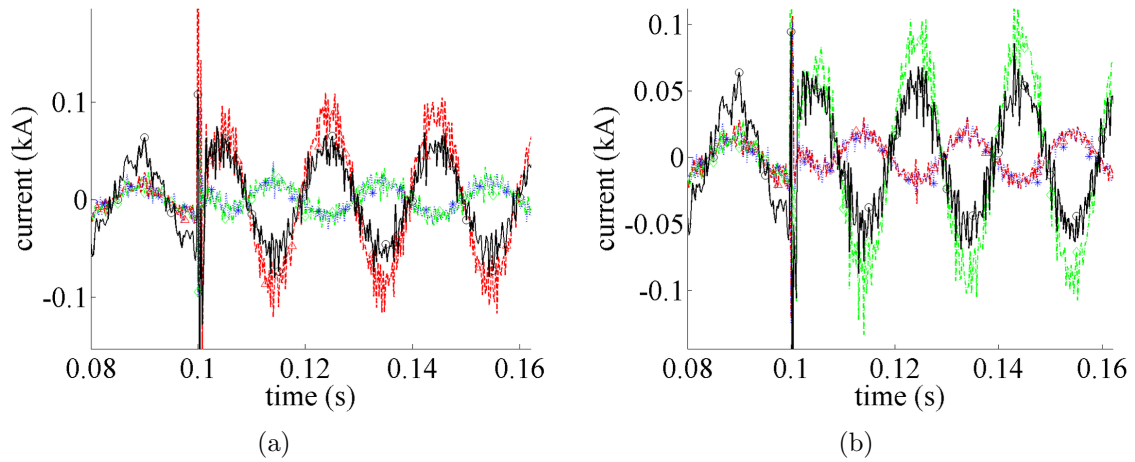


Figure 4.7: Current differential behavior when fault occurred in (a) feeder 1, and (b) feeder 2

### Current harmonics behavior

As can be seen in Fig. 4.8 and 4.9, discontinuity occurs in the current harmonics other than the fundamental frequency. This behavior does not depend on the fault location. It is also shown that the magnitude of the discontinuity in the faulty feeder is much larger than the healthy one. Therefore, there is possibility to use the current harmonics spectrum to detect the faulty feeder.

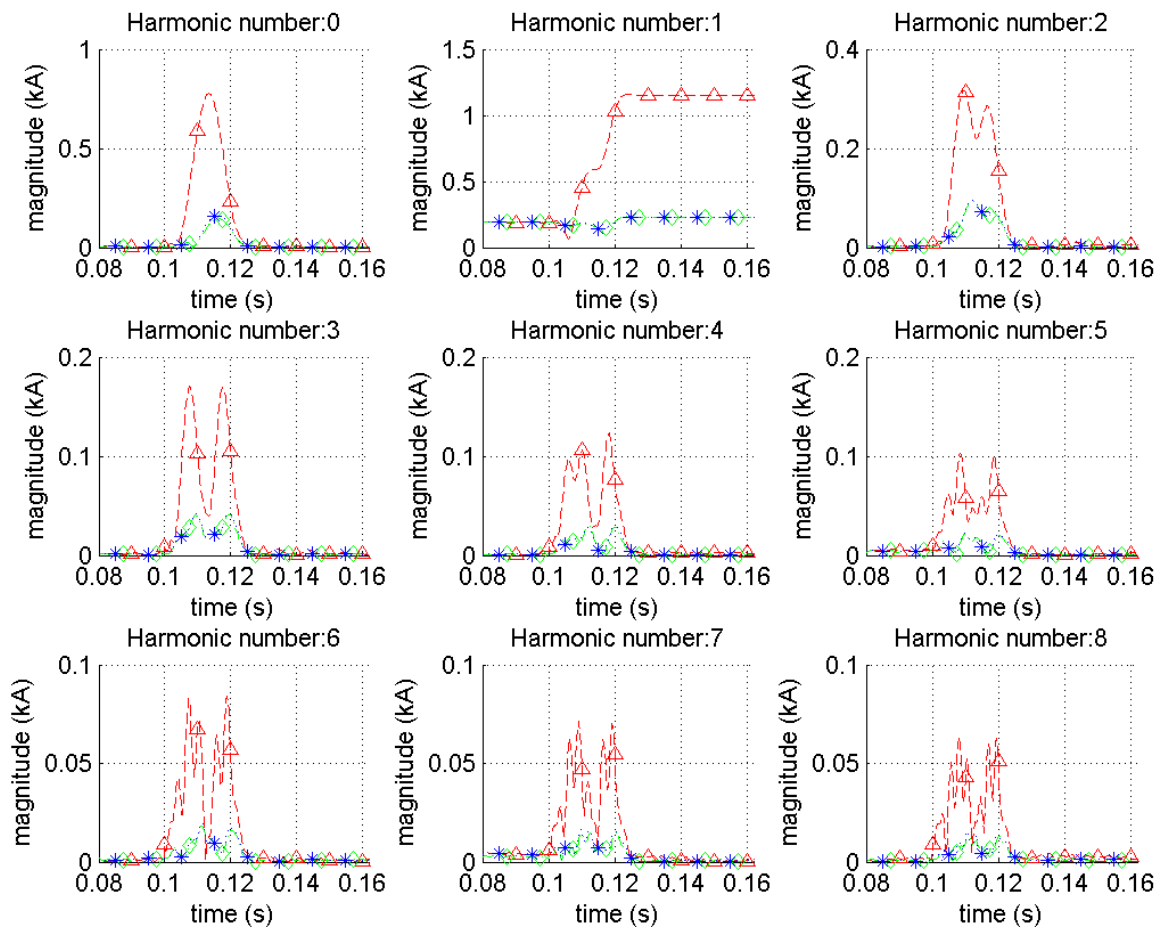


Figure 4.8: Current harmonics behavior when fault occurred in feeder 1

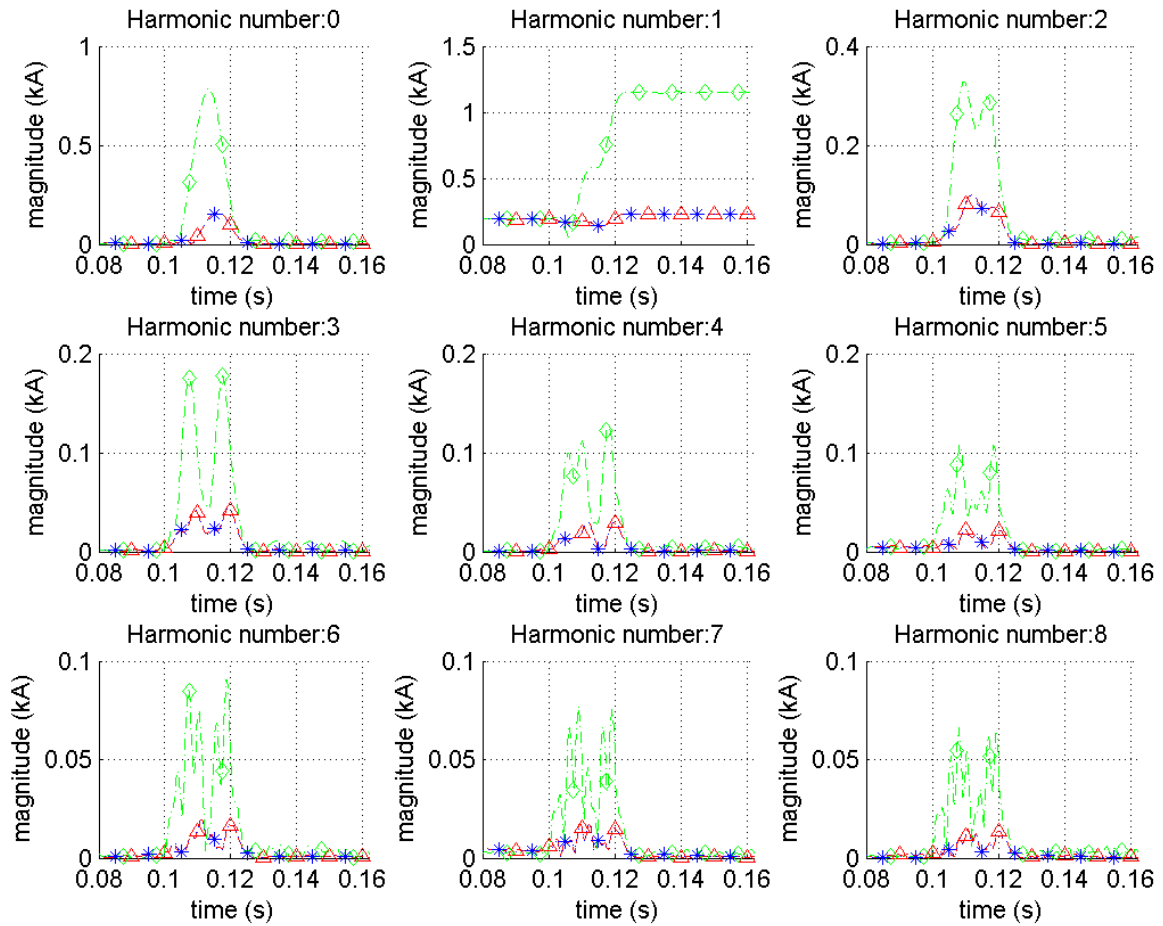


Figure 4.9: Current harmonics behavior when fault occurred in feeder 2

### Detection of faulty feeder

After observing the behavior of the signals in the collection point, the detection of faulty feeder can be done using the flowchart depicted in Fig. 4.10. The first step is to observe the instantaneous active power direction in the HVDC feeder. Then the next step is to investigate the peak current value or the harmonic spectrum of the current. If the conditions in both step are fulfilled by feeder  $x$ , then the fault is occurred in feeder  $x$ .

Fault detection by observing only the instantaneous active power direction is not suggested, because during the starting state of the system, instantaneous active power from the HVDC may flow towards the wind farm (reverse direction).

Fault detection by observing only the peak current is also not suggested, since the peak current may introduce a problem due to fast transient occurred in the system.

Further study in the harmonic spectrum of the current is needed in order to use this in the fault detection method. Other transient status in the system, e.g. switching of the circuit breaker, may also interference the harmonic spectrum of the current. Therefore, it is needed to differentiate between fault and other transient conditions.

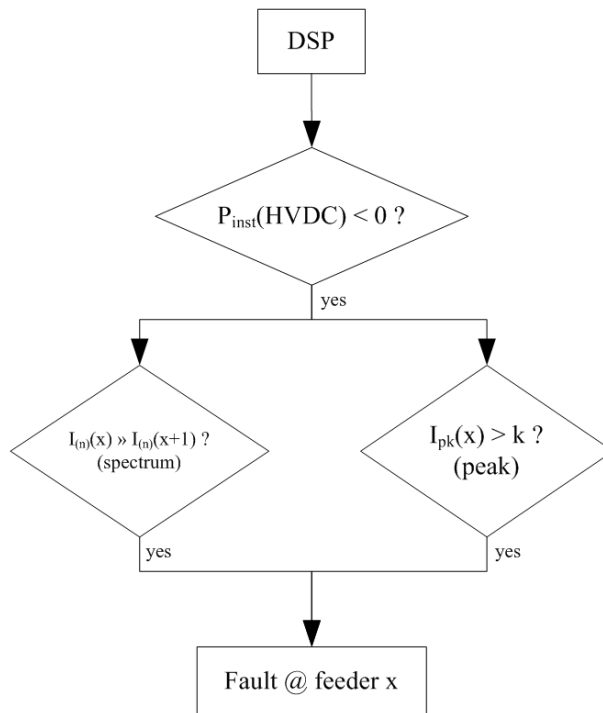


Figure 4.10: Proposed method for detecting the faulty feeder

## 4.2.2 Feeder line

The main objective of having the fault detection method in the feeder line is to identify the faulty section within a feeder line. It is assumed that the fault is occurred in feeder 1. Three MUs are placed in three different locations as depicted in Fig. 4.11.

In order to see the difference between faulty and healthy section within a feeder, the following analysis will be focused only when the fault is occurred in location 2 and 3. Which means that when the fault is occurred in location 2, the faulty section is the one between FCG 01 and 02, while if the fault is occurred in location 3, the faulty section is the one between FCG 02 and 03.

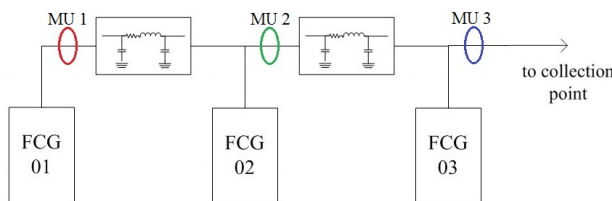


Figure 4.11: The ellipses indicate the measurement points along the feeder line

### Peak current behavior

In Fig. 4.12(a), the peak current difference during fault between MU 1 and MU 2 is 1.15 kA ( $\approx 1.83$  p.u.), while between MU 2 and MU 3 is only 0.075 kA ( $\approx 0.12$  p.u.). When the fault is occurred in location 3 (Fig. 4.12(b)), the peak current difference during fault between MU 2 and MU 3 is 0.99 kA ( $\approx 1.5$  p.u.), while between MU 1 and MU 2 is only 0.082 kA ( $\approx 0.12$  p.u.). This behavior shows the possibility to use the peak current difference between two contiguous MUs for detecting the faulty section within a feeder.

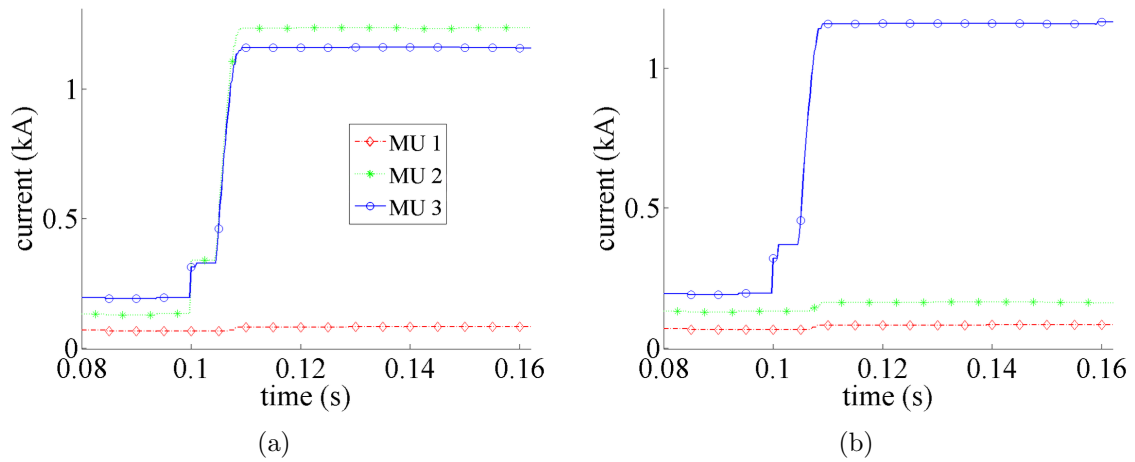


Figure 4.12: Peak current behavior when fault is occurred in (a) location 2, and (b) location 3

### Peak voltage behavior

Figure 4.13 indicates that during the fault, peak voltage in three different locations is less than 500 volt (or less than 0.017 p.u.). This means that it will be hard to use the magnitude of the voltage to discriminate the healthy and the faulty feeder.

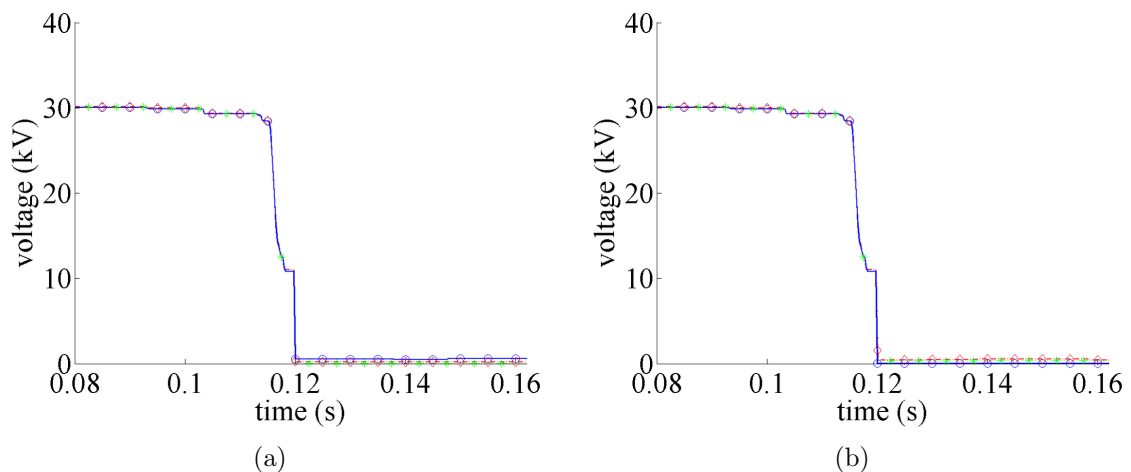


Figure 4.13: Peak voltage behavior when fault is occurred in (a) location 2, and (b) location 3

### Instantaneous active power behavior

As explained before, the direction of the active power flow during fault is toward the faulty point. As can be seen in Fig. 4.14(a), when fault occurred in location 2, the instantaneous active power in MU 3 is equal to -0.13 MW, and in MU 1 is equal to 798 W. In Fig. 4.14(b), instantaneous active power in MU 1 is equal to 2.9 kW and in MU 2 is equal to 3.3 kW. The instantaneous active power in the faulty point is equal to zero, since the voltage at that point is also zero. It may be hard to have the relay selectivity based on the magnitude of the instantaneous active power, but if communication link between two contiguous MUs is available, the direction comparison of the instantaneous active power may be used for detecting the faulty section within a feeder.

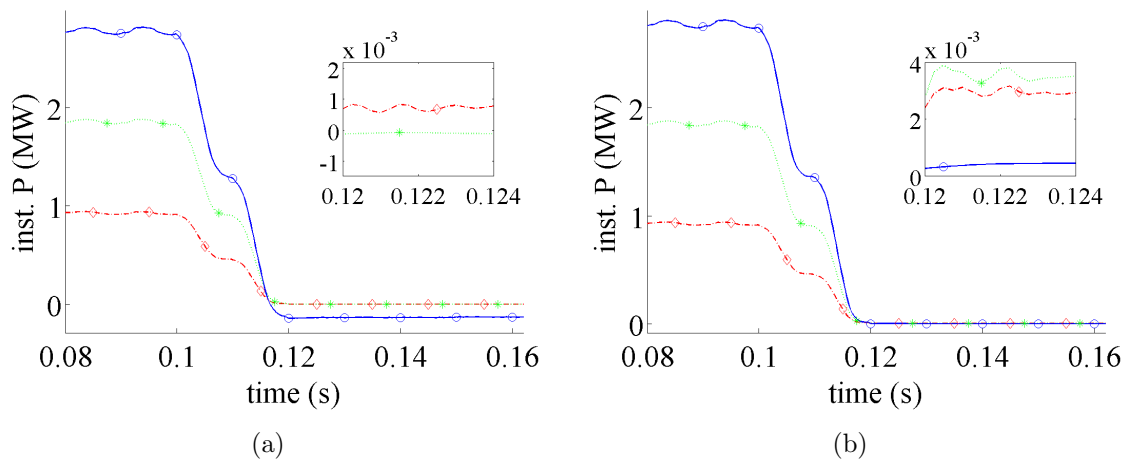


Figure 4.14: Instantaneous active power behavior when fault is occurred in (a) location 2, and (b) location 3

### Voltage differential behavior

The differential of the voltage as depicted in Fig. 4.15 cannot be used to identify the faulty section since the signal is too noisy and the magnitude is very low.

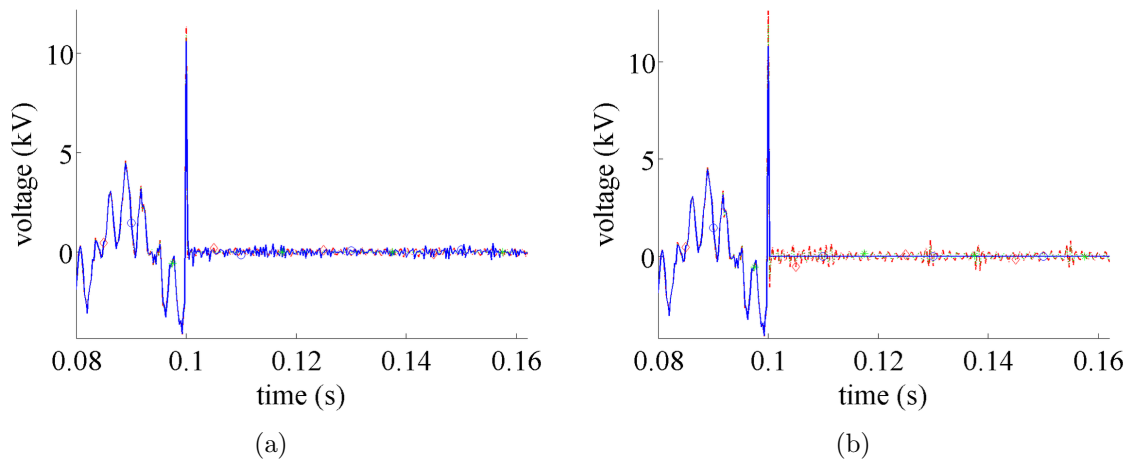


Figure 4.15: Voltage differential behavior when fault is occurred in (a) location 2, and (b) location 3

### Positive sequence line-ground impedance behavior

The positive sequence line-ground impedance value, as can be calculated using (4.5), is changing right after the fault initiated. As can be seen in Fig. 4.16, in the normal condition all positive sequence line-ground impedance in three MUs are having the positive resistance (real value of impedance). When fault is initiated these impedance is reduced and equal to zero after reaching fault steady-state.

The trajectory of the positive sequence line-ground impedance in different MUs may be different for the different fault location. Figure 4.17 shows the closer look on the impedance behavior 0.0073 seconds after the fault is initiated. It can be clearly seen in Fig. 4.17(a) that the impedance in MU 1 is moving towards zero through the positive imaginary values, while the other two MUs are moving through the negative imaginary values. When the

fault is occurred in location 3 (Fig. 4.17(b)), the impedance in MU 1 and MU 2 are moving through the positive imaginary value. By comparing the impedance trajectory between two MUs, the faulty section within the line can be identified.

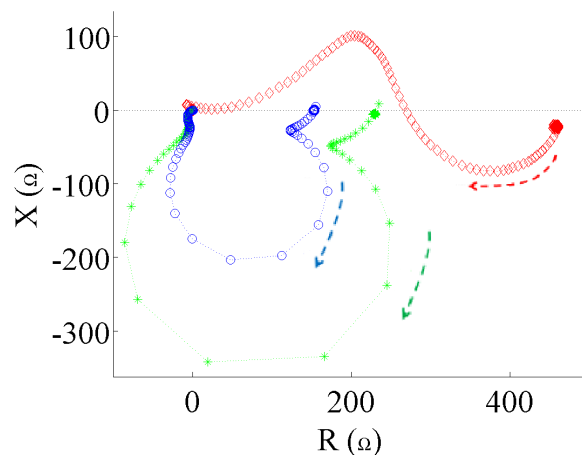


Figure 4.16: Positive sequence line-ground impedance behaviors when the fault is occurred in location 2, the dashed arrows represent the movement direction

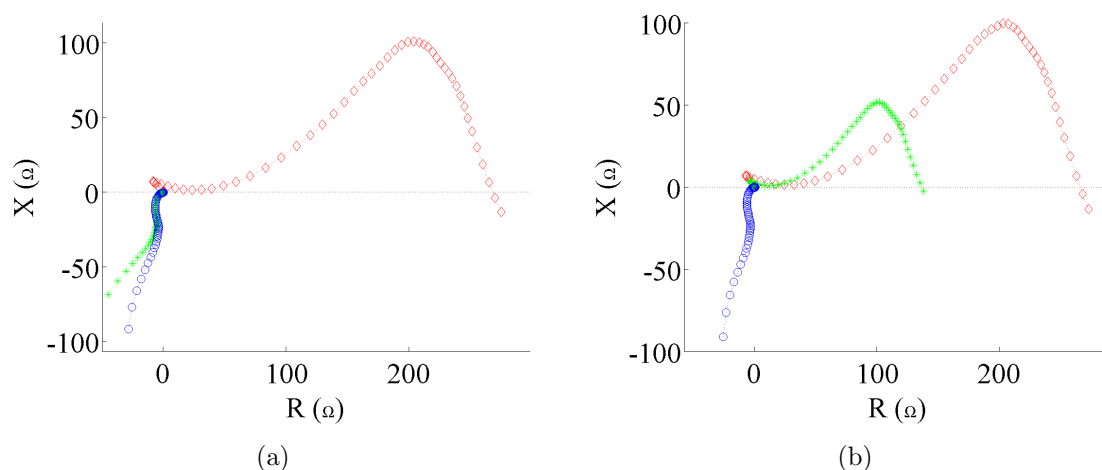


Figure 4.17: Closer look in positive sequence line-ground impedance behavior when the fault is occurred in (a) location 2 and (b) location 3

### Detection of faulty section within a feeder line

After observing the behavior of the signals in the collection point, the detection of faulty feeder can be done using the flowchart depicted in Fig. 4.18. The faulty section can be detected by comparing the peak current between two contiguous MUs, or comparing the direction of the instantaneous active power or the positive sequence line-ground impedance between MUs. It means that the communication line between MUs is needed to have selectivity in the feeder line protection system.

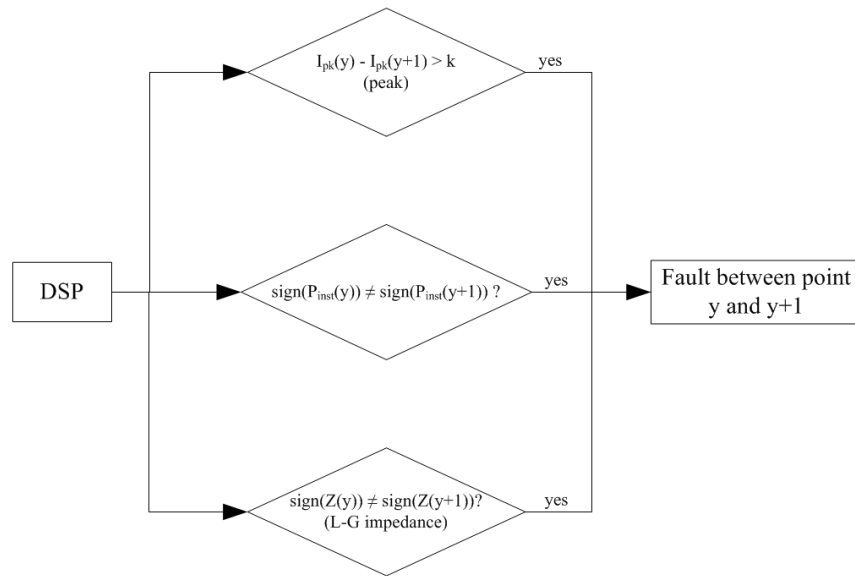


Figure 4.18: Proposed method for detecting the faulty section within a feeder

### 4.3 Different simulation conditions

In the following subsections, short-circuit simulations are performed for different system conditions. The purpose of these simulations is to test the proposed fault detection method for different system conditions. The presented results in the following figures are for fault located in location 2 (feeder 1).

#### 4.3.1 Different sampling frequency

By changing the sampling frequency of the A/D converter, the accuracy of the DSP analysis can be changed. The DSP result when using two different sampling frequencies (4 and 10 kHz) are shown.

As can be seen in Fig. 4.19 - Fig. 4.22, there are no significant difference between 4 kHz and 10 kHz sampling frequency DSP results.

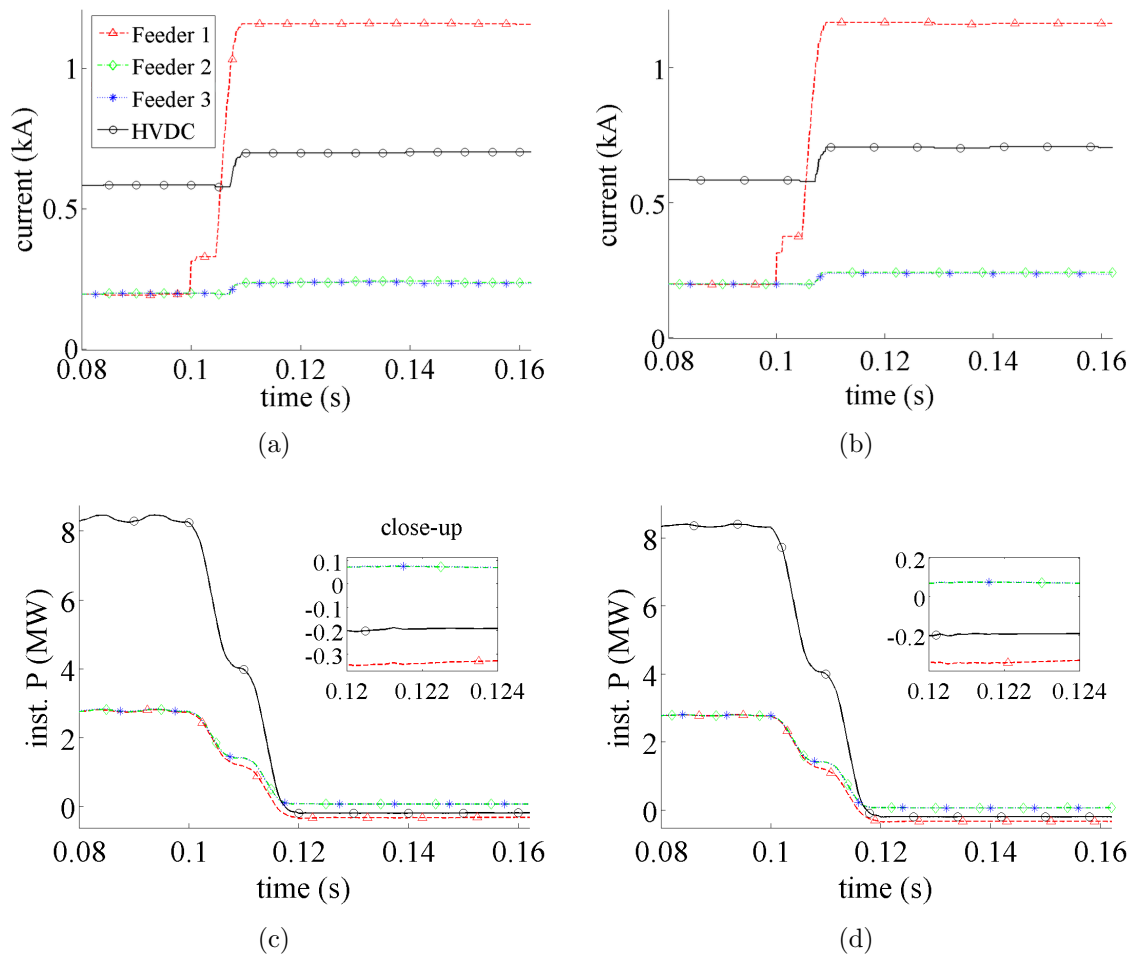


Figure 4.19: (a) and (c) show the peak current and the instantaneous active power behavior in the collection point for 4 kHz sampling frequency, while (b) and (d) are for 10 kHz sampling frequency

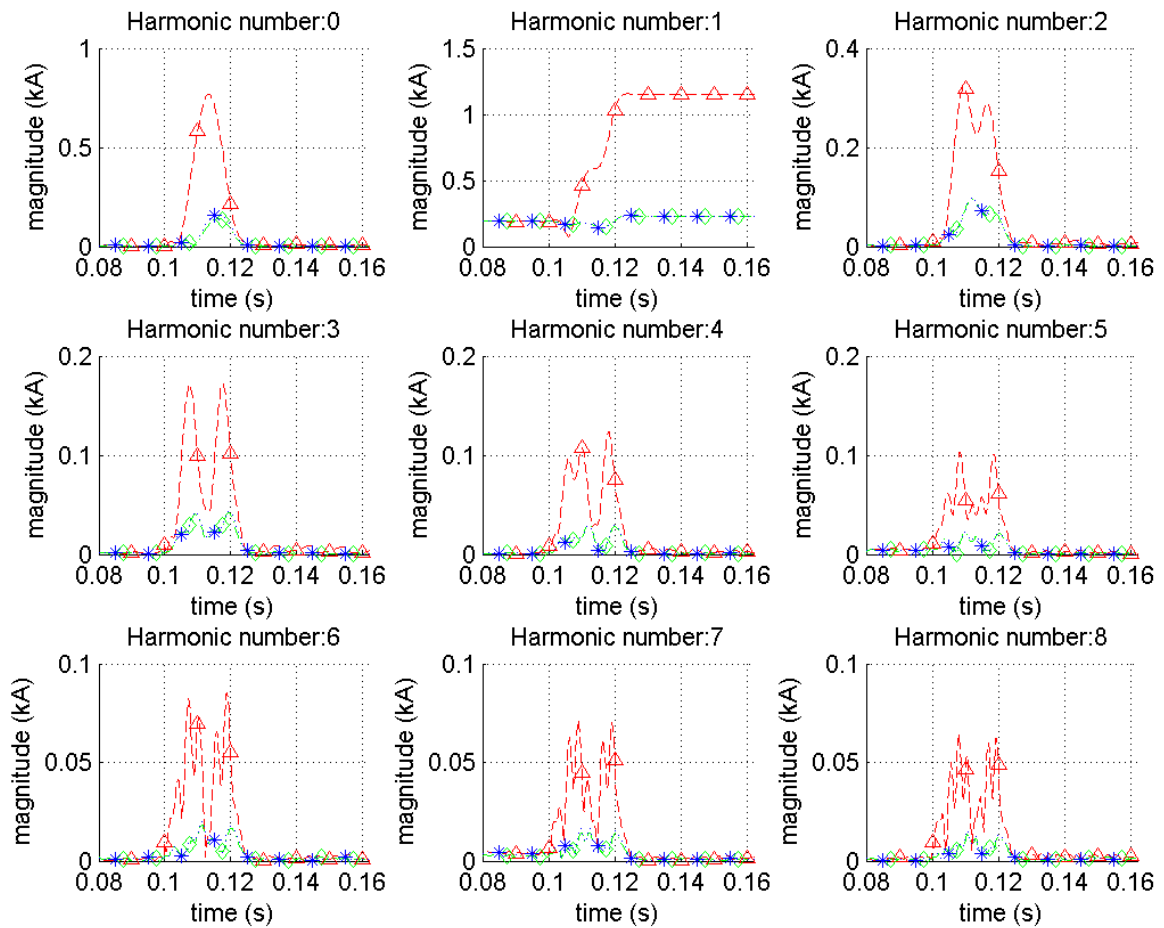


Figure 4.20: Current harmonic spectrum in the collection point for 4 kHz sampling frequency

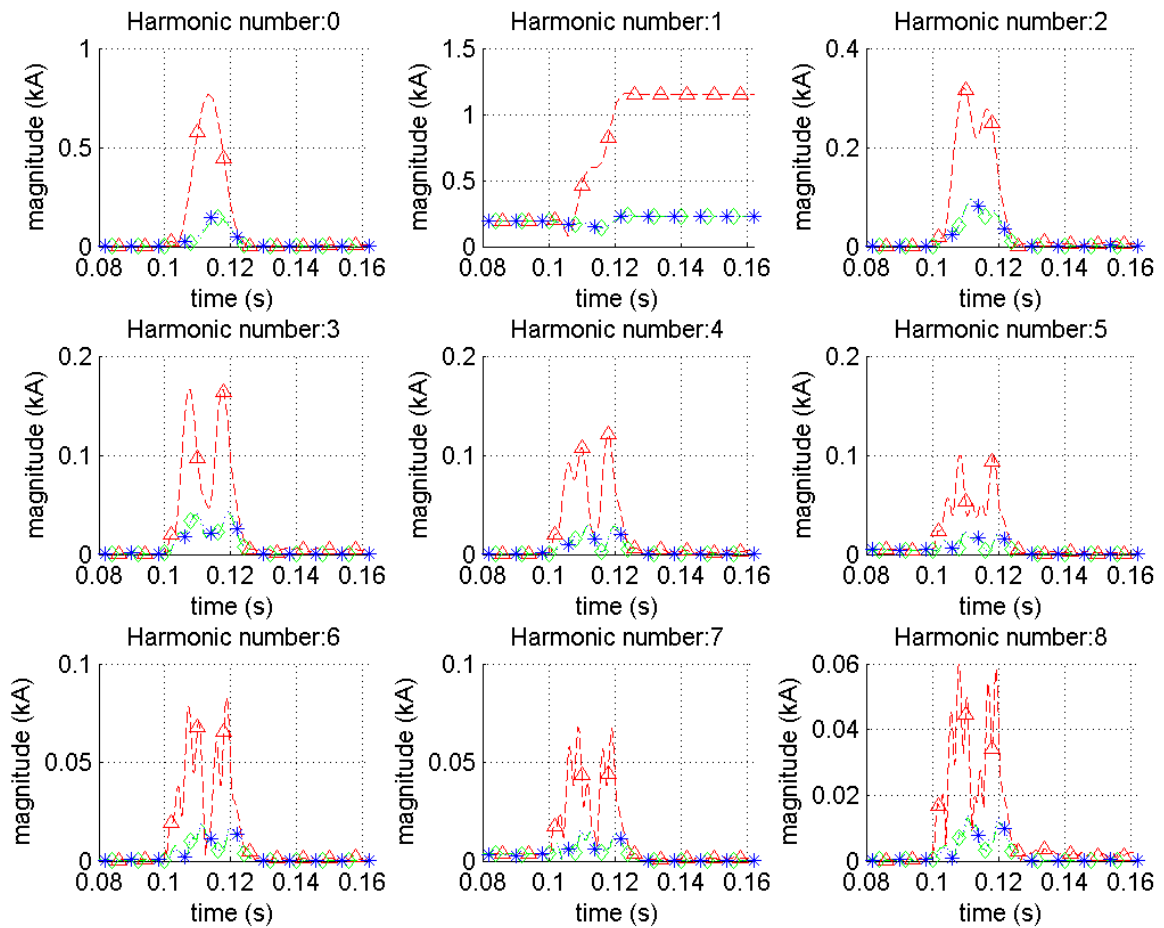


Figure 4.21: Current harmonic spectrum in the collection point for 10 kHz sampling frequency

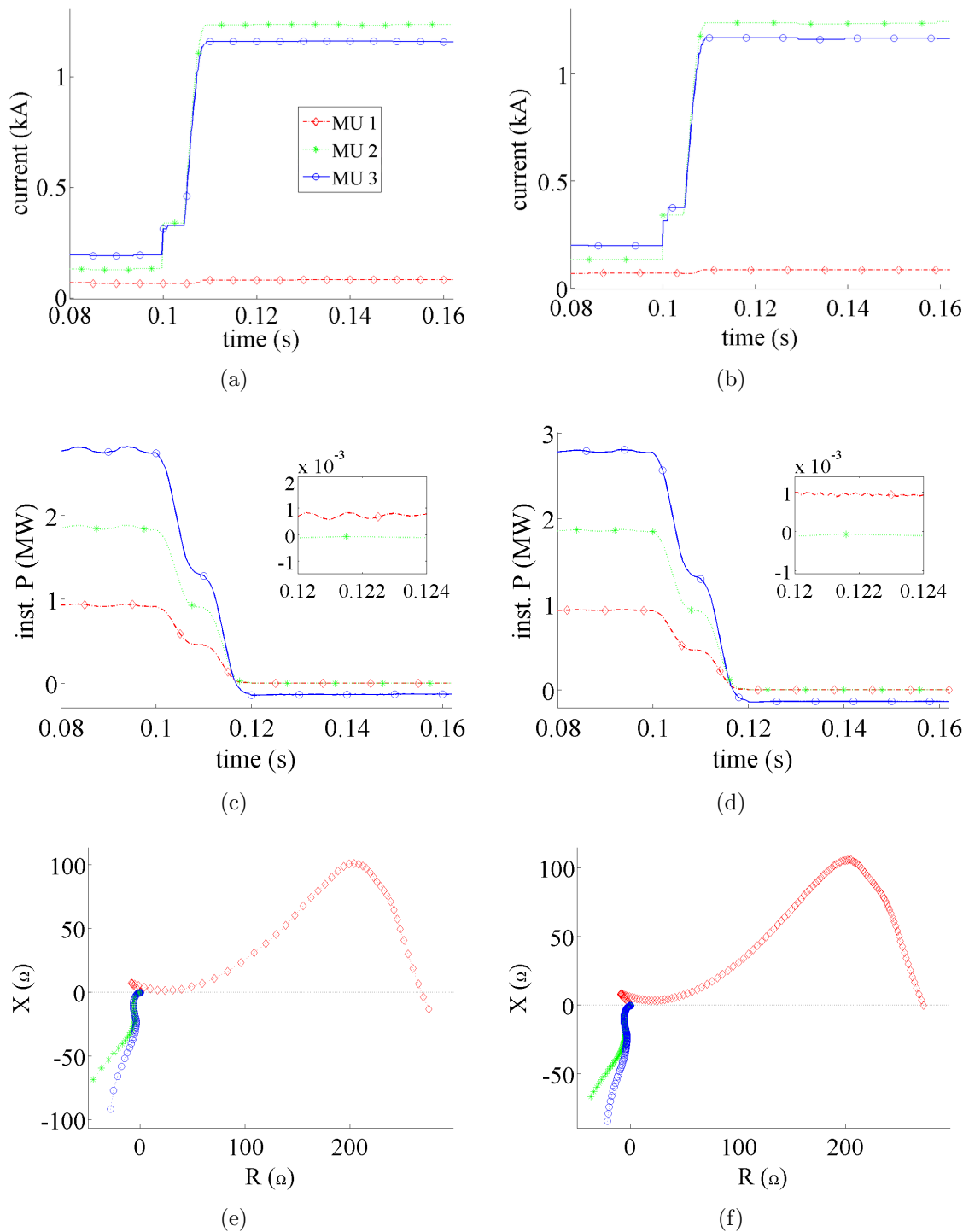


Figure 4.22: (a), (c), and (e) show the peak current, the instantaneous active power, and the positive sequence line-ground impedance behavior in feeder 1 for 4 kHz sampling frequency, while (b), (d), (f) are for 10 kHz sampling frequency

### 4.3.2 Different wind turbines condition

Due to some reasons, e.g. maintenance, FCG 02, 04, 06, 08, and 09 are disconnected from the system. This means that when fault occurs, only 4 FCGs are contributing to the fault. The fault current is reduced from 2.2 p.u. to 1.59 p.u. The DSP results when only 4 FCGs connected to the system are shown in the following figures.

The current peak behavior, as depicted in Fig. 4.23(a), has higher value right after the fault is initiated. This is due to the transient current that occurred in the system. During the fault steady-state, peak current in feeder 1 is equal to 0.85 kA ( $\approx 1.34$  p.u.) or decreased 0.31 kA as compared to the base case (when all turbines are in service).

The behavior of the instantaneous active power (Fig. 4.23(b)) and the discontinuity of the current spectrum (Fig. 4.24) are as same as their behavior in the base case. This also happens in the feeder line, Fig. 4.25.

It can be concluded that the proposed fault detection methods still work properly for this condition.

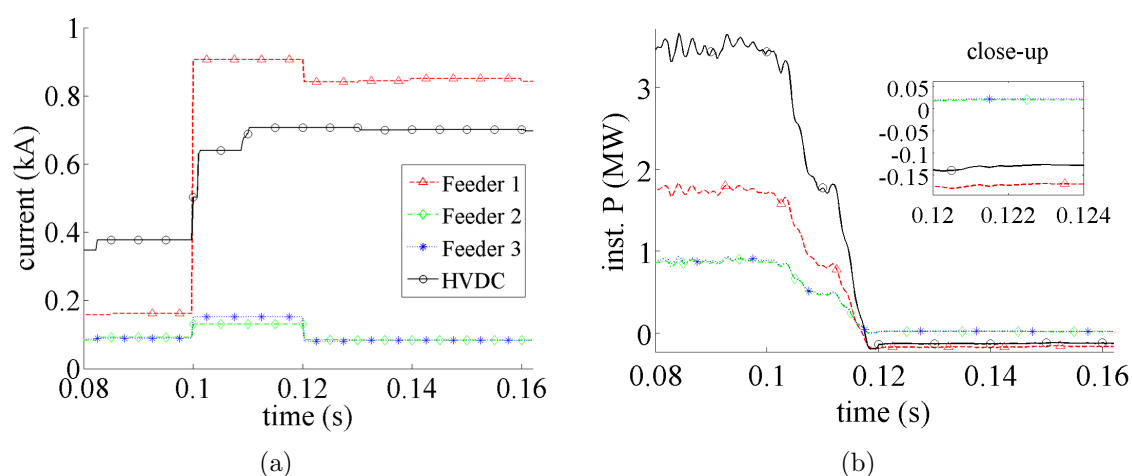


Figure 4.23: (a) the peak current behavior, (b) the instantaneous active power behavior in the collection point

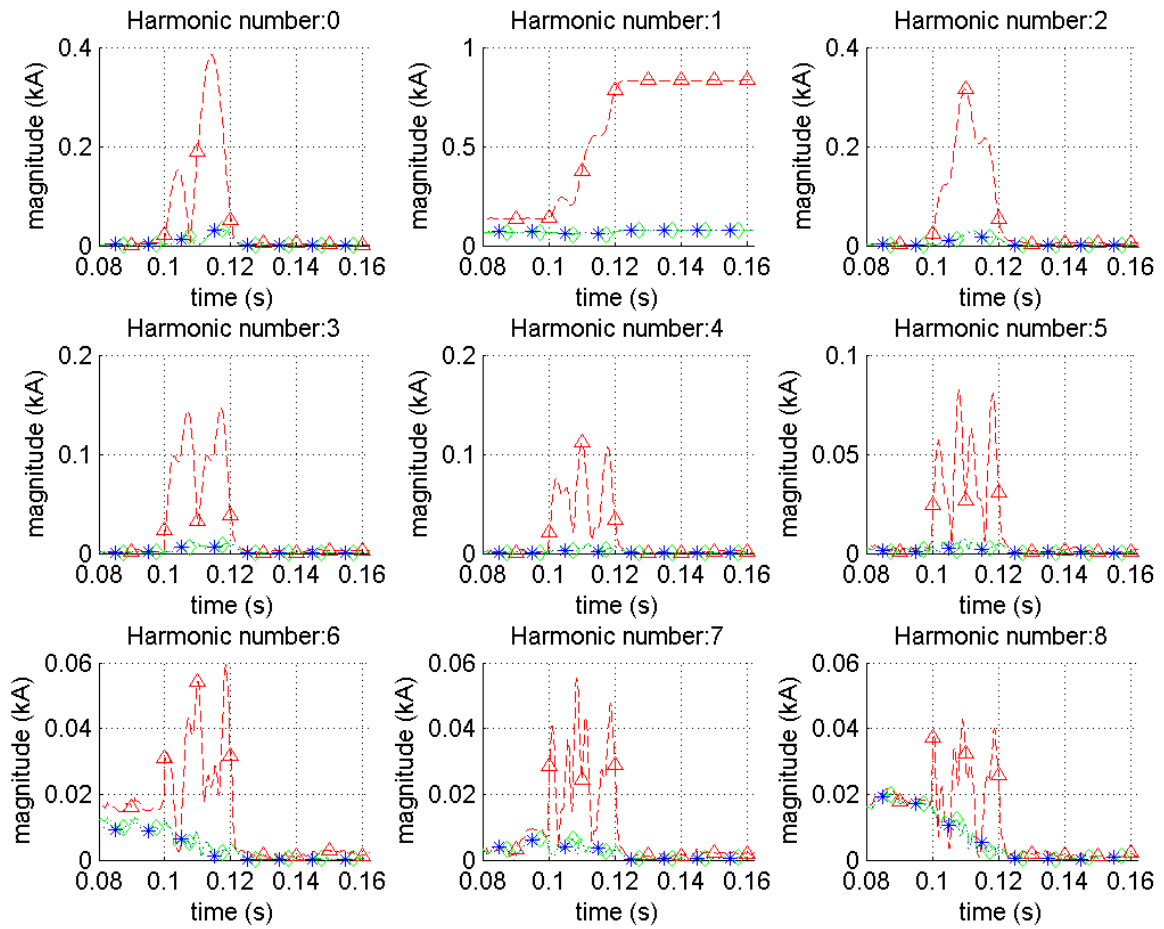


Figure 4.24: Current harmonic spectrum in the collection point

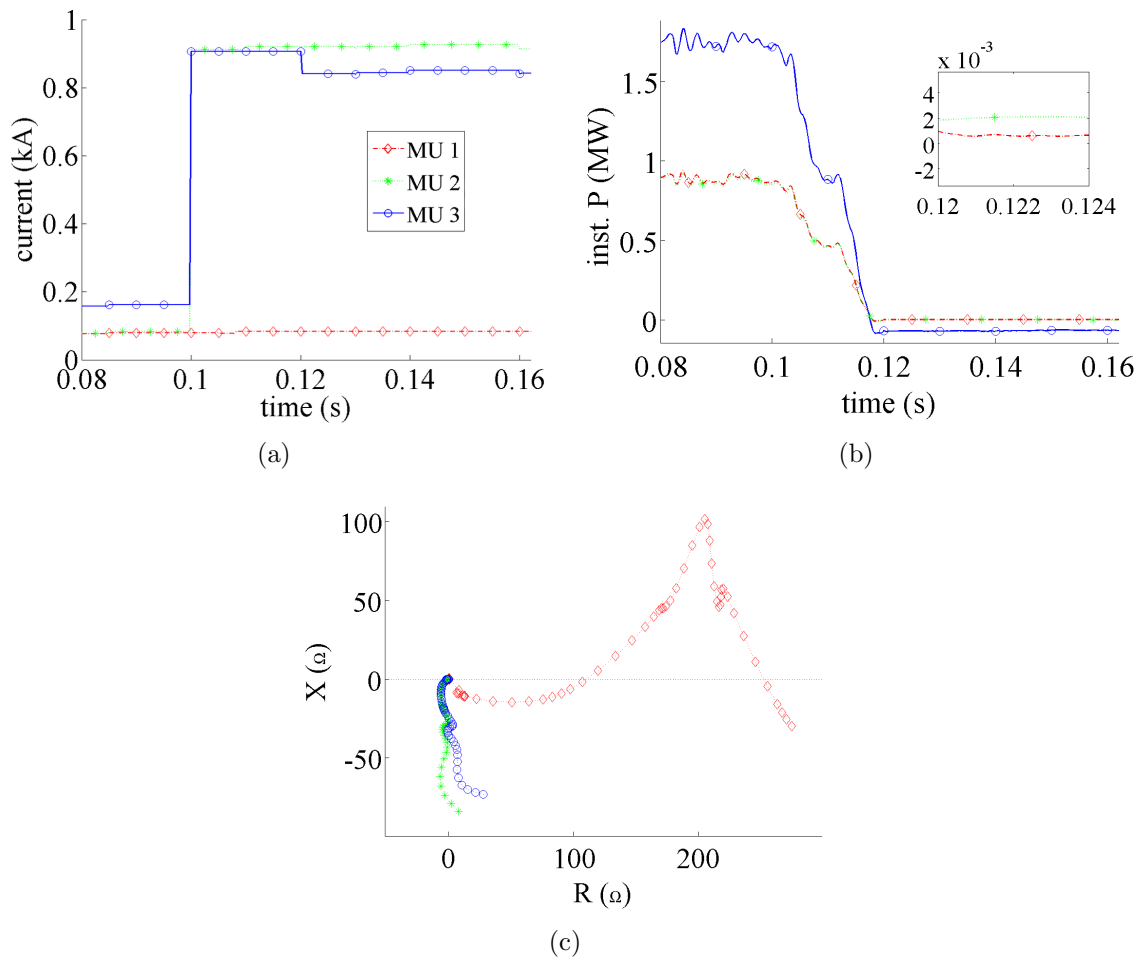


Figure 4.25: (a) the peak current behavior, (b) the instantaneous active power behavior, (c) the positive sequence line-ground impedance behavior in feeder 1

### 4.3.3 Reduced HVDC short-circuit current contribution

If the fault current is reduced, the rating of the equipments used in the system can also be reduced. The fault current magnitude in this case system depends on the short-circuit contribution from the HVDC. Therefore, by reducing HVDC short-circuit current contribution from 1.1 p.u. to 0.1 p.u., the fault current is reduced from 2.2 p.u. to 1.2 p.u. The DSP results are shown in the following figures.

As can be seen in Fig. 4.26(a), during the fault, the peak current in the HVDC feeder is reduced to 0.071 kA ( $\approx 0.1$  p.u.), therefore the peak current in the faulty feeder is equal to 0.52 kA or reduced 0.64 kA as compared with the base case. The peak current difference between the faulty feeder and healthy feeder is equal to 0.28 kA.

Since short-circuit current contribution from the HVDC is reduced, the instantaneous active power during fault in the HVDC feeder (Fig. 4.26(b)) and in the line (Fig. 4.28(b)) are also reduced, but the behavior of its direction is still as same as in the base case.

The difference of the peak current between MU 1 and MU 2 as depicted in Fig. 4.28(a) is equal to 0.52 kA ( $\approx 0.83$  p.u.) or decreased 0.63 kA as compared to the base case.

The behavior of the current spectrum depicted in Fig. 4.27 and positive sequence line-ground impedance depicted in Fig. 4.28(c) are also as same as in the base case.

It can be concluded that the proposed fault detection methods still work properly for this condition, but the setting of the peak current threshold in the collection point must be reduced and the MUs should be able to observe small value of instantaneous active power (several hundred watts).

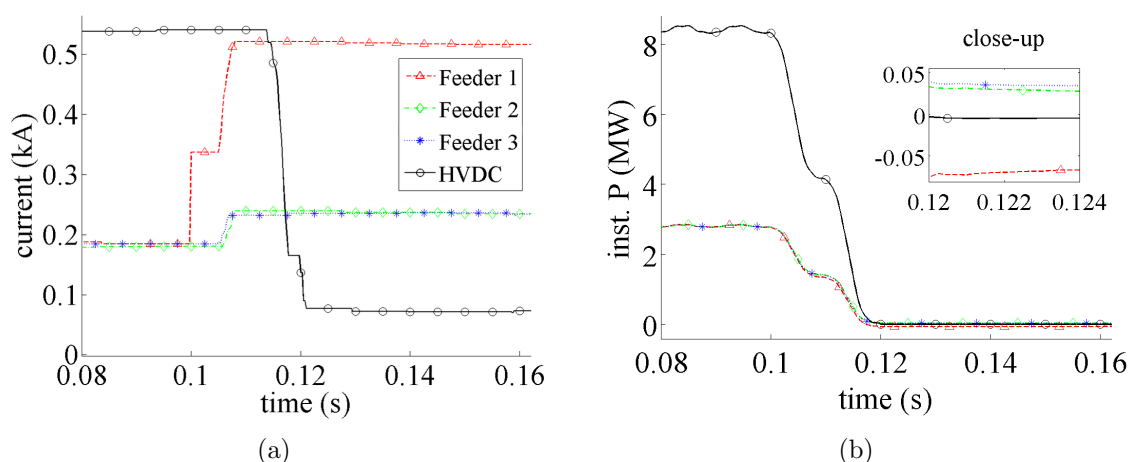


Figure 4.26: (a) the peak current behavior, (b) the instantaneous active power behavior in the collection point

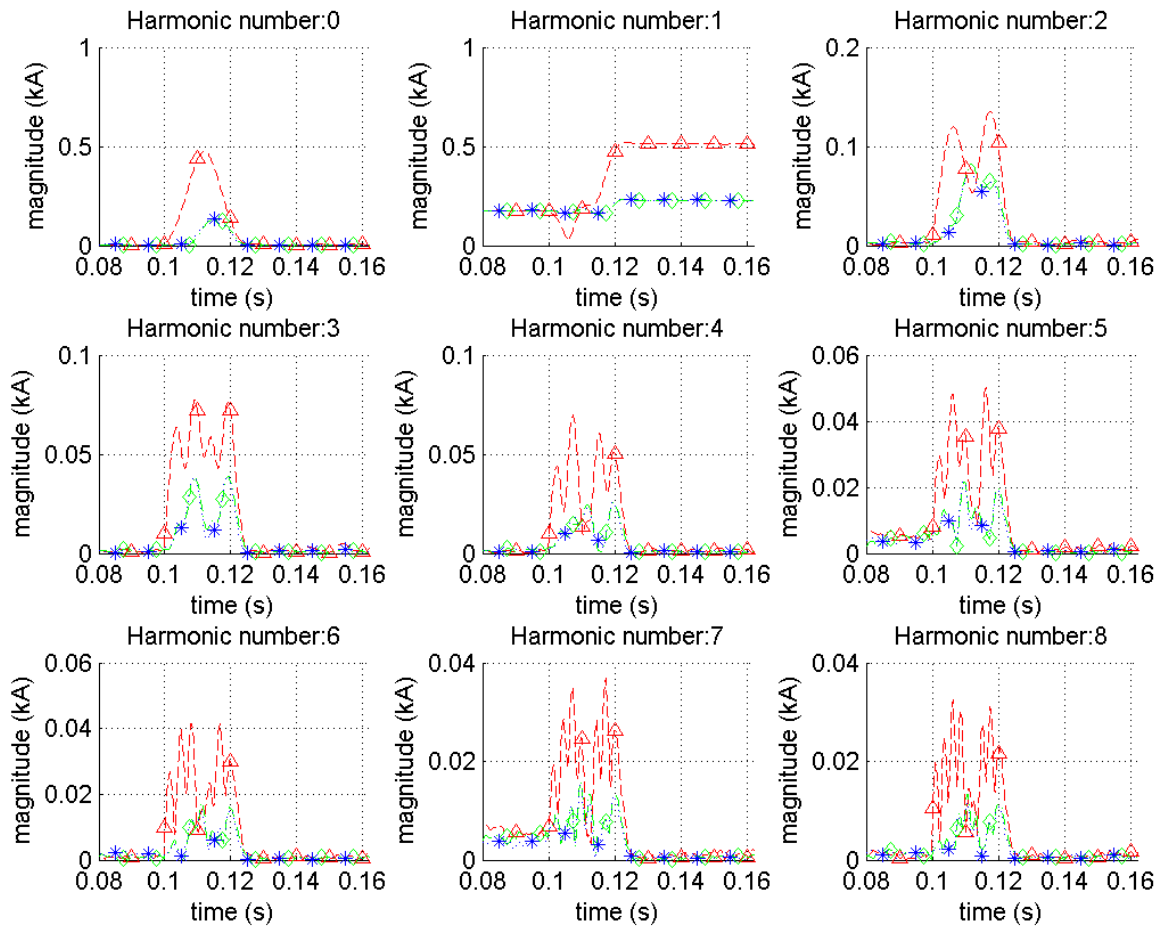


Figure 4.27: Current harmonic spectrum in the collection point

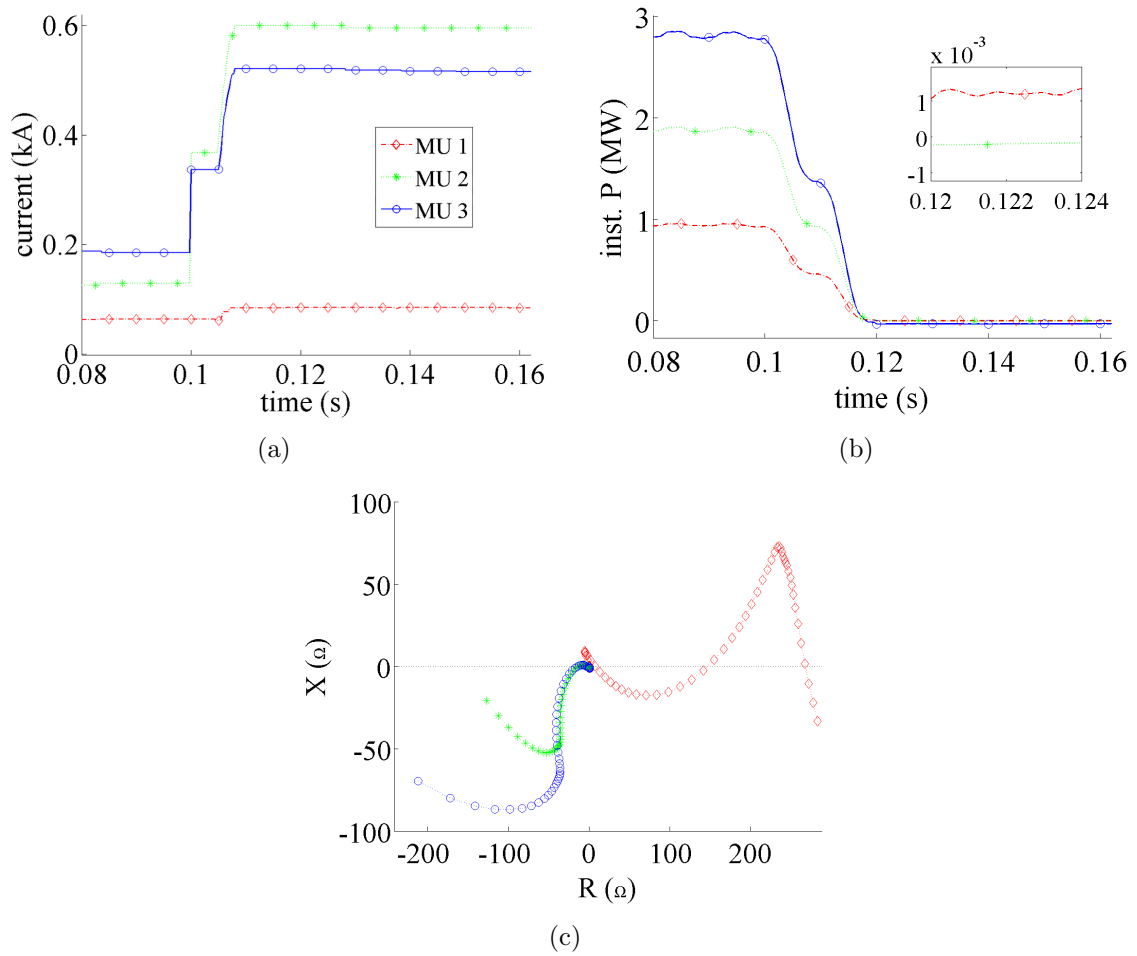


Figure 4.28: (a) the peak current behavior, (b) the instantaneous active power behavior, (c) the positive sequence line-ground impedance behavior in feeder 1

### 4.3.4 Reduced HVDC short-circuit current contribution and different wind turbines condition

In this case, the short-circuit contribution is reduced to 0.1 p.u. and only several wind turbines are connected to the system. It means that the fault current is very low (0.6 p.u.) as compared to the base case. The DSP results for this case are shown in the following figures.

Figure 4.29(a) shows that the peak current of the faulty feeder is equal to 0.22 kA ( $\approx 0.35$  p.u.) or only 6% above the normal current (when all turbines in feeder 1 are in service). This means that the peak current behavior can no longer be used to detect the faulty feeder.

The instantaneous active power during fault in the HVDC feeder (Fig. 4.26(b)) and in the line (Fig. 4.28(b)) is also reduced, but the behavior of its direction is still as same as in the base case. In order to use the direction of the instantaneous active power to detect the fault, the MUs should be able to observe small value of instantaneous active power (several hundred watts).

The difference of the peak current between MU 1 and MU 2 (Fig. 4.31(a)) is equal to 0.21 kA ( $\approx 0.33$  p.u.), while the difference between MU 2 and MU 3 is equal to 0.07 kA ( $\approx 0.11$  p.u.). Therefore, the peak current difference between MUs can still be used to detect the faulty section within a line.

The behavior of the current spectrum depicted in Fig. 4.30 and positive sequence line-ground impedance depicted in Fig. 4.31(c) are as same as in the base case.

It can be concluded that the proposed methods for detecting faulty feeder may not working properly for this condition, while the proposed faulty section detection can still be used.

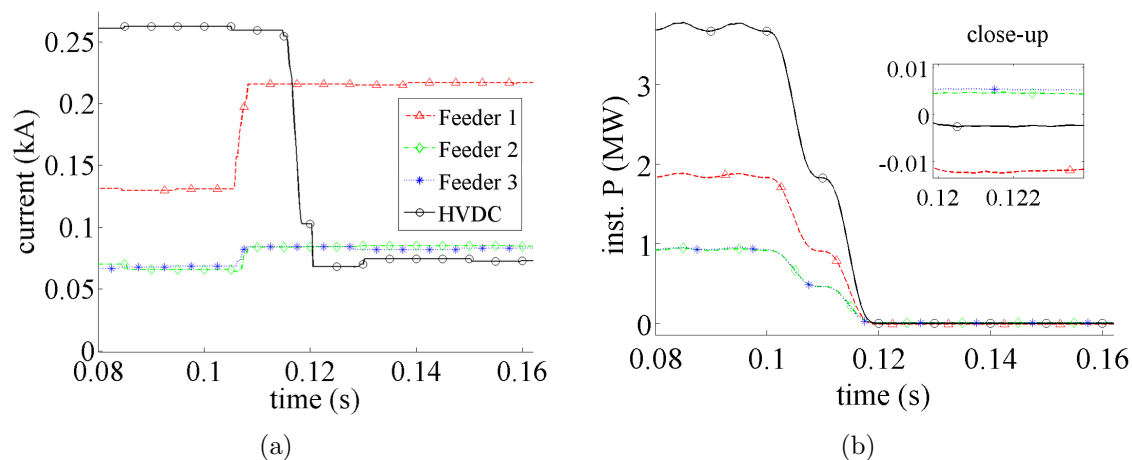


Figure 4.29: (a) the peak current behavior, (b) the instantaneous active power behavior in the collection point

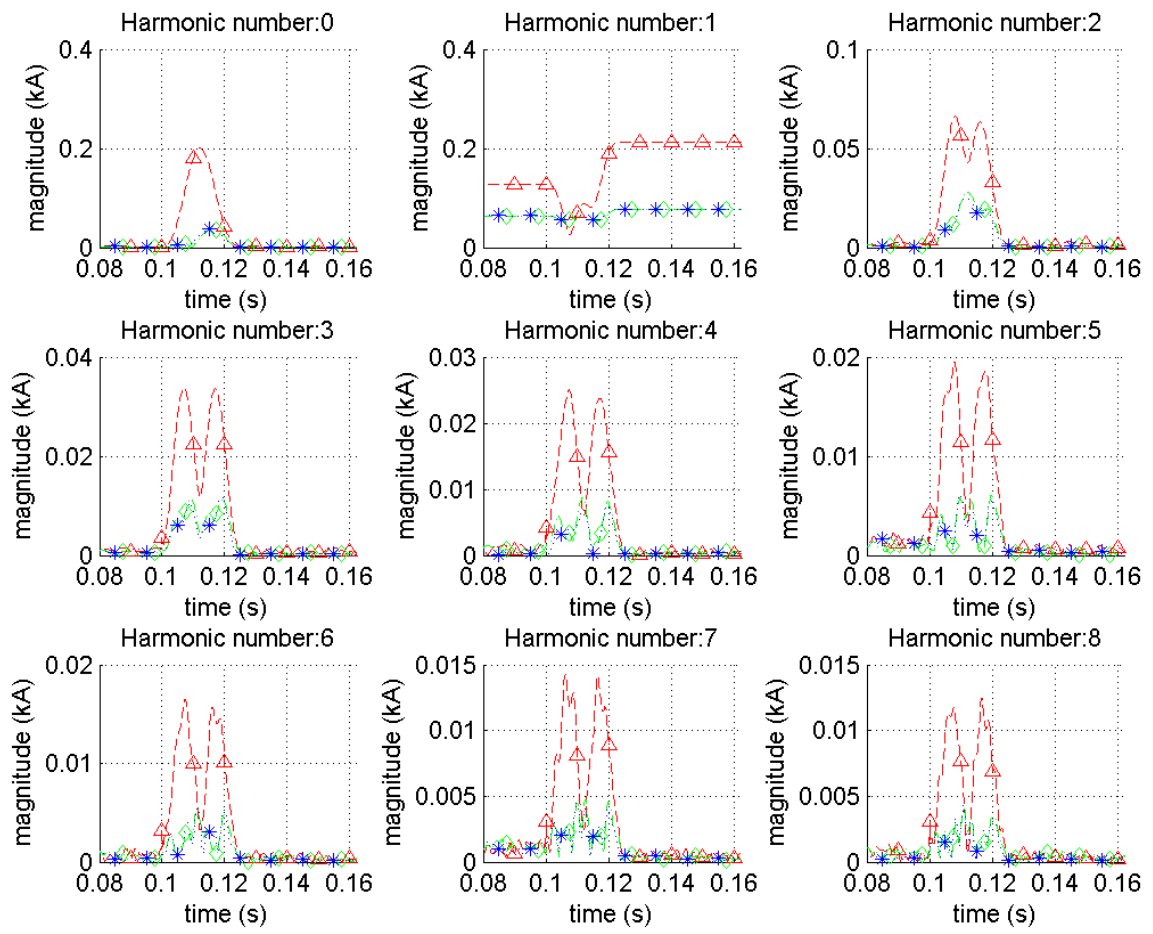


Figure 4.30: Current harmonic spectrum in the collection point

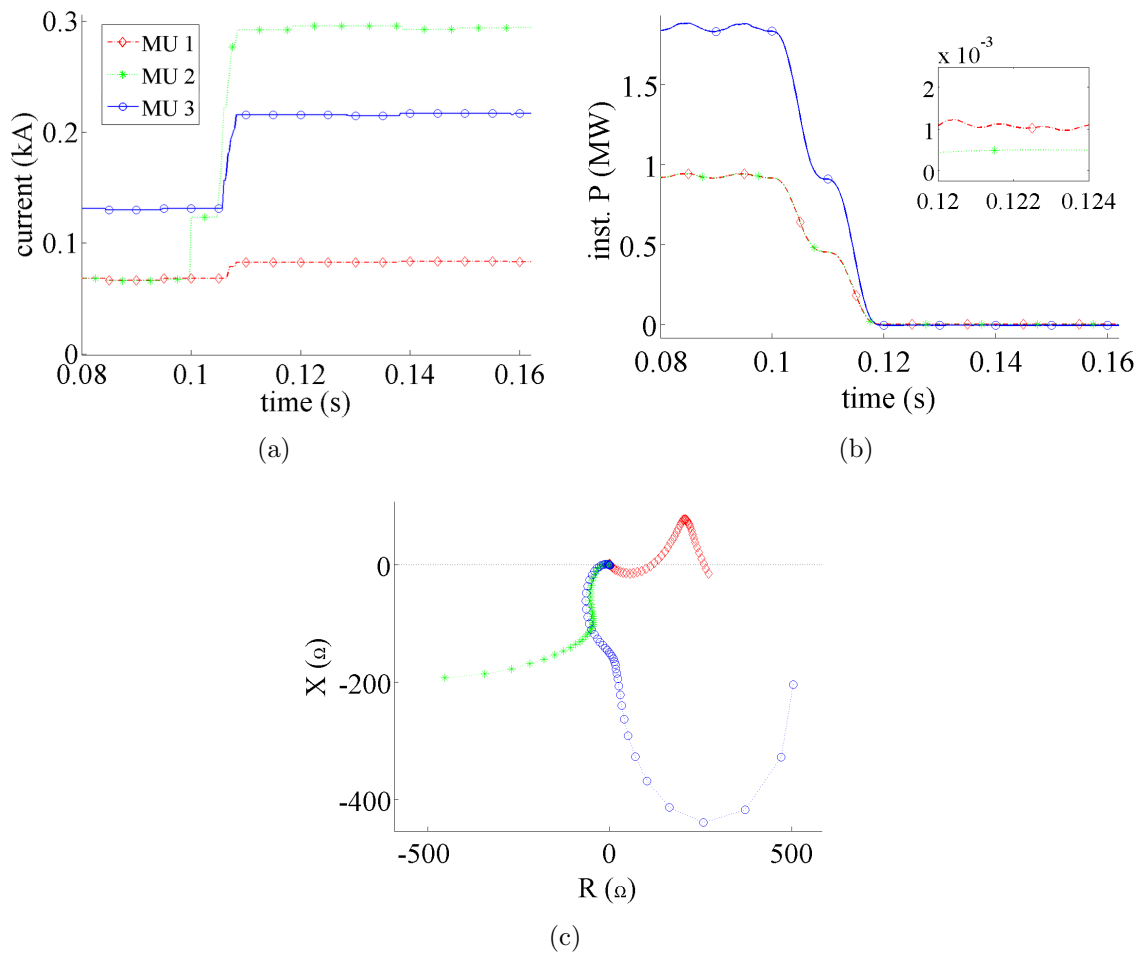


Figure 4.31: (a) the peak current behavior, (b) the instantaneous active power behavior, (c) the positive sequence line-ground impedance behavior in feeder 1

### 4.3.5 Different wind turbines and HVDC power rating

In this case, the turbines power rating is changed into 5 MW and 1.5 MW, and the HVDC power rating is changed into 45 MVA and 13.5 MVA respectively. In this study, all converters are assumed to be ideal, therefore the scaling of the system can be achieved easily by scaling up the FCG and HVDC rated power. While in the real system, a lot of things, such as the power electronic switches, controller gain, transformers, circuit breakers, are need to be considered before changing the system rating. The DSP results are shown in the following figures.

As can be seen in Fig. 4.32(a) - Fig. 4.37, the behavior of the results are all the same. The differences in magnitude are due to the difference of the system rating. Therefore, the proposed method can still be used for different system rating.

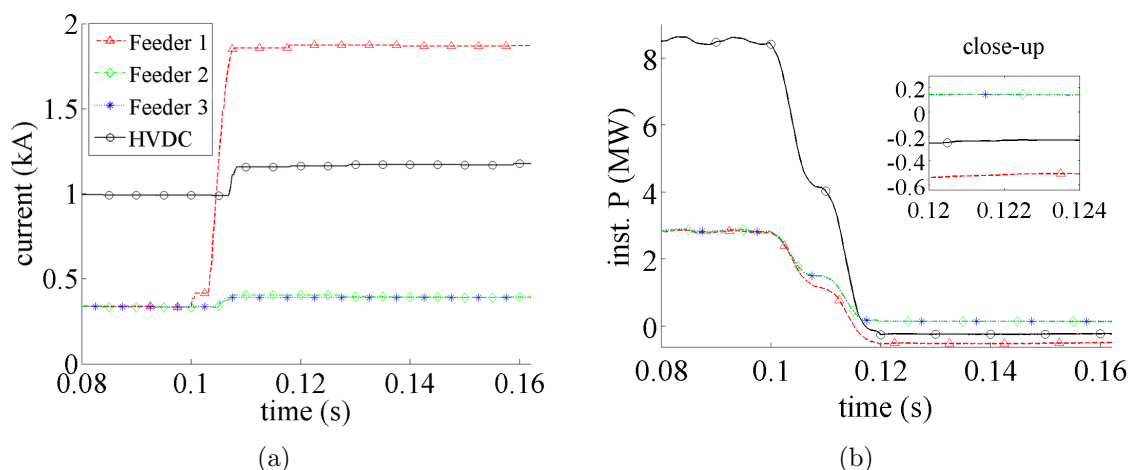


Figure 4.32: (a) the peak current behavior, (b) the instantaneous active power behavior in the collection point for 5 MW turbines

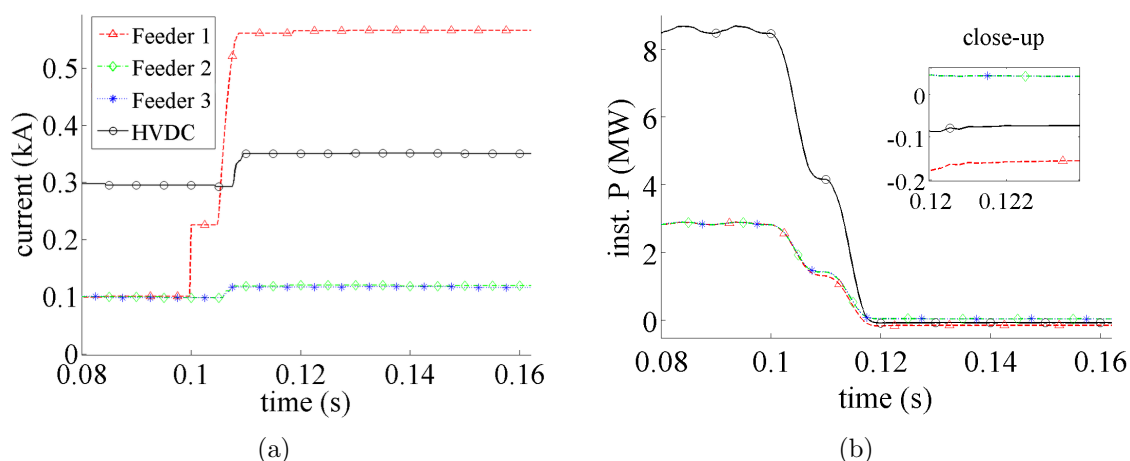


Figure 4.33: (a) the peak current behavior, (b) the instantaneous active power behavior in the collection point for 1.5 MW turbines

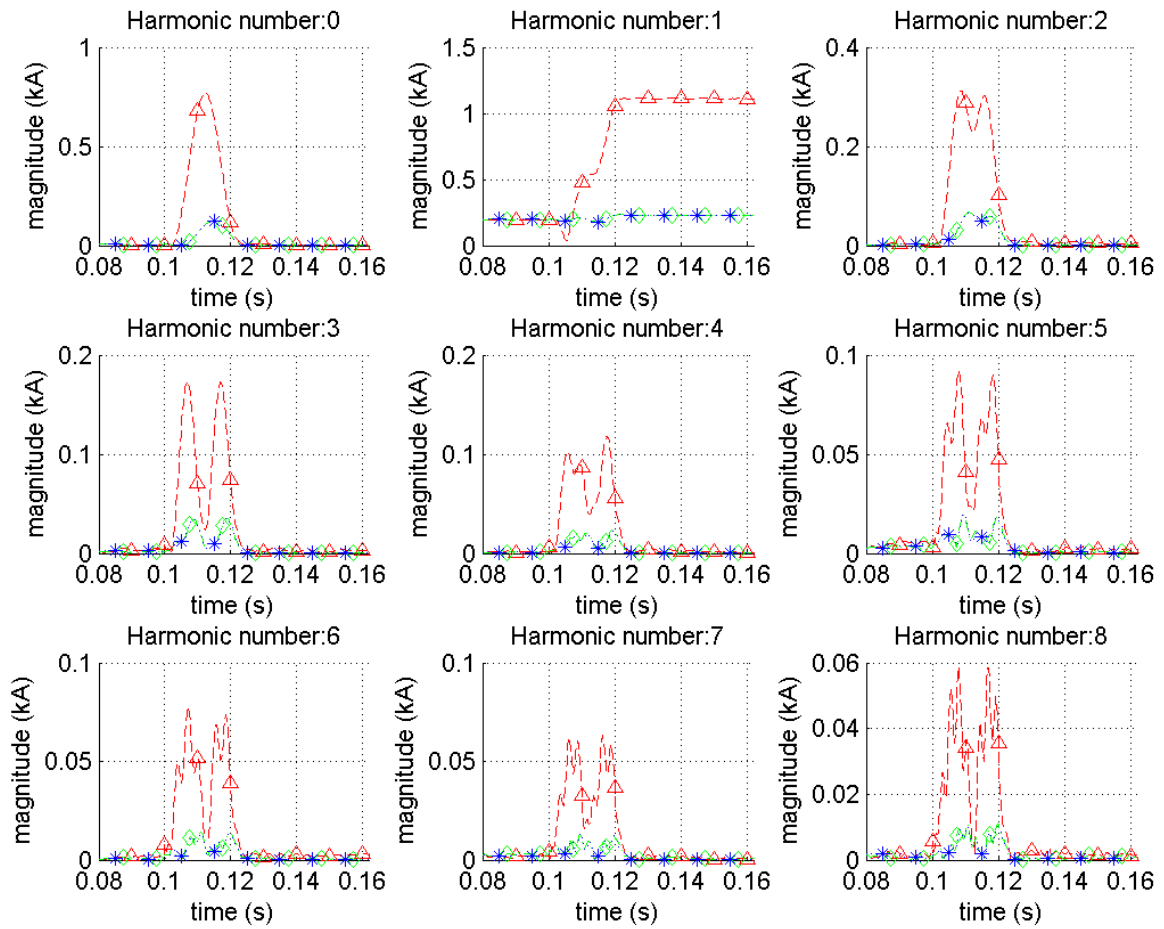


Figure 4.34: Current harmonic spectrum in the collection point for 5 MW turbines

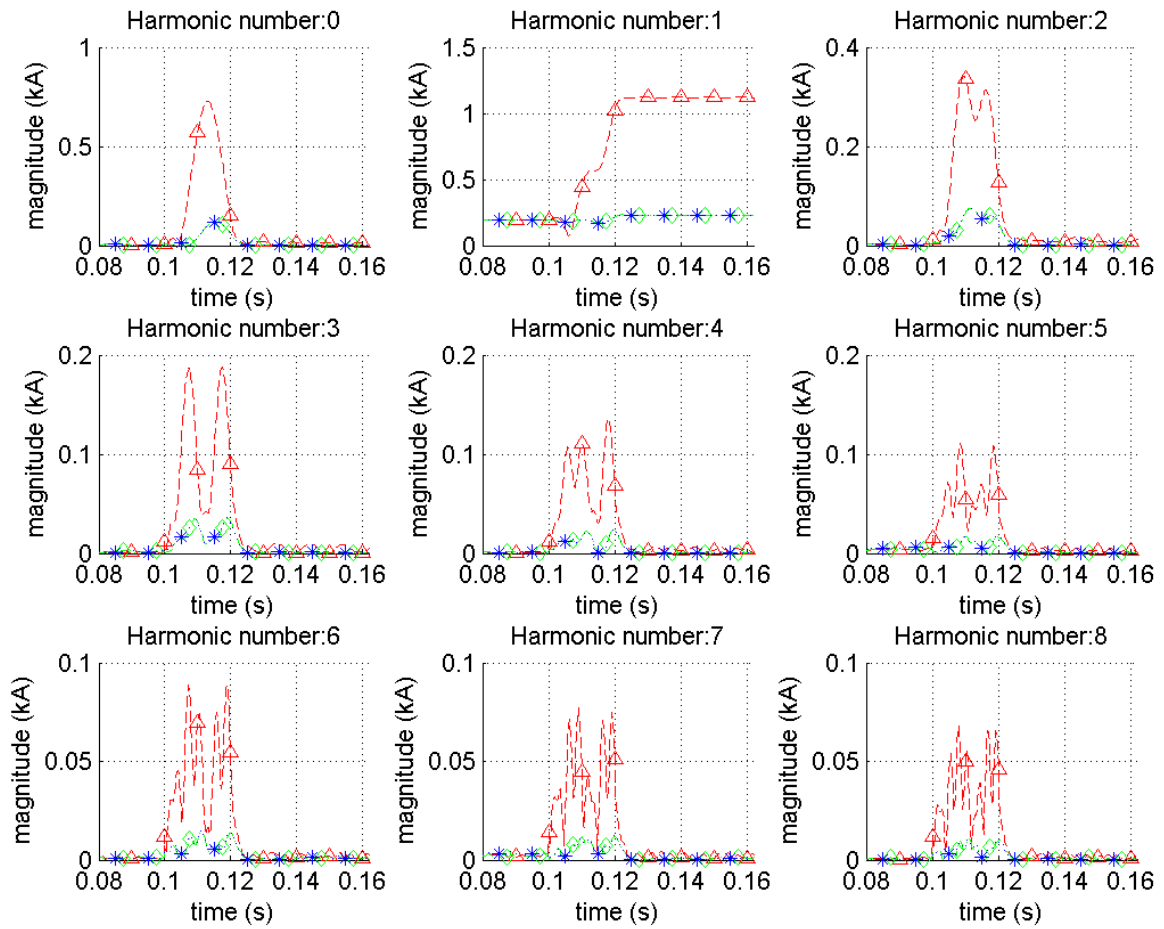


Figure 4.35: Current harmonic spectrum in the collection point for 1.5 MW turbines

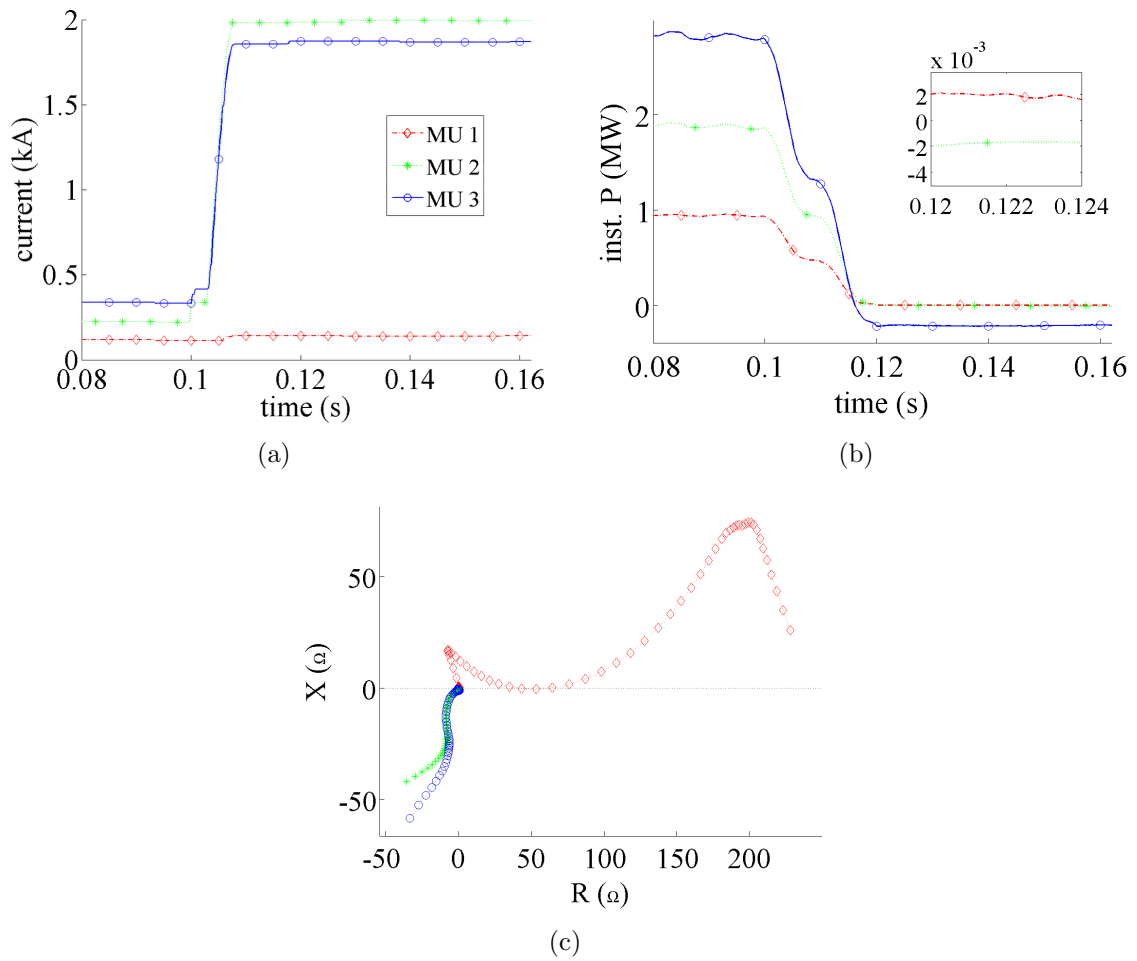


Figure 4.36: (a) the peak current behavior, (b) the instantaneous active power behavior, (c) the positive sequence line-ground impedance behavior in feeder 1 for 5 MW turbines

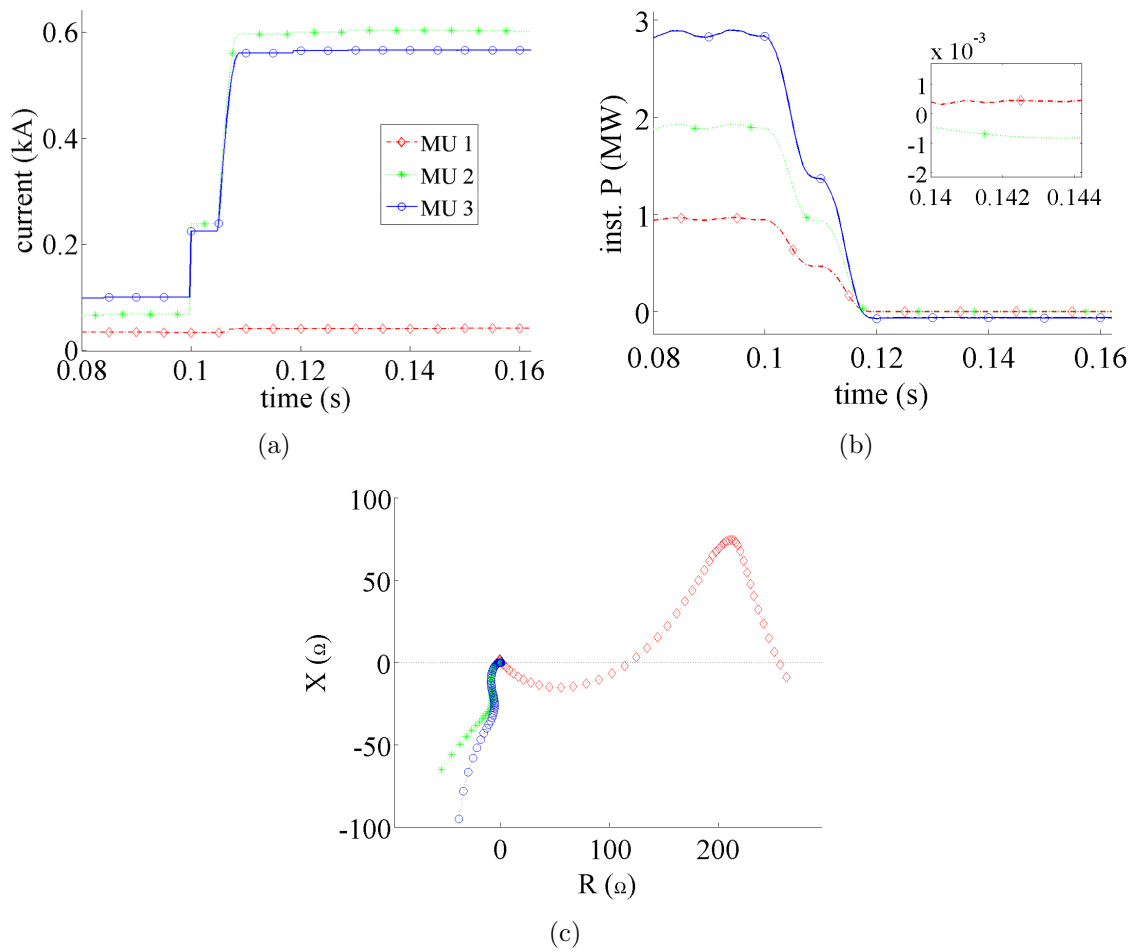


Figure 4.37: (a) the peak current behavior, (b) the instantaneous active power behavior, (c) the positive sequence line-ground impedance behavior in feeder 1 for 1.5 MW turbines

# Chapter 5

## Conclusions and Future Works

### 5.1 Conclusions

Wind farm is located in remote site, especially in offshore in order to gain more stable wind speed, which in turn increases turbine efficiency, without increasing the environmental impacts. HVDC transmission system becomes the best solution for connecting this remote wind farm to the main AC grid, if the connection exceeds 80 km offshore or 500 km onshore.

During short-circuit fault in the terminal of a converter, short-circuit current flowing from the converter is usually limited (10% above rated current is used in this study), due to power electronic switch safety reason. Having the limited short-circuit current contribution from the converter, fault detection in the HVDC-connected wind farm with FCG becomes a challenging task.

In order to study the behavior of the system under faulty condition, a case study has been built and implemented in PSCAD/EMTDC software. The case study consists of 9 wind turbines distributed in 3 feeders.

Six-pulses IGBT converter is implemented in FCG and HVDC. The grid-side converter control of FCG system is based on the rotating  $dq$ -frame aligned with the FCG terminal voltage. The hysteresis band method is used to generate the IGBT firing pulse signal, since it has a quick response to the current dynamic.

During normal condition, the sending-end HVDC (SE-HVDC) converter, which collect the power coming from the wind farm, acts like a voltage source having constant voltage and frequency. At this condition, sinusoidal PWM converter control is implemented in the SE-HVDC converter. If the fault is occurred in the wind farm collection grid, the SE-HVDC converter acts as a current source injecting limited current to the faulty point. At this condition, SE-HVDC use the same converter control as in the grid-side converter of FCG.

Since the converter found in FCG or HVDC system is giving the limited short-circuit contribution, the converter can be represented as a current source during the fault. The amount of the current injected from the converter does not depend on the fault location. The fault current can be calculated as the sum of short-circuit current contribution from FCG and HVDC. Since during the fault FCG only contribute reactive current, short-circuit current contribution from the FCG does not depend on the wind speed.

In order to imitate the work of digital protective relays, simulation output signals are sampled and post-processed. Sliding data window method is implemented in MATLAB. Instantaneous peak value, instantaneous active power, discrete Fourier transform (DFT) analysis, differential value, and positive sequence line-ground impedance calculation are applied in the DSP part.

By analyzing the DSP outputs, the faulty feeder can be detected by observing the

instantaneous active power direction of the HVDC feeder together with the peak current measurement or the current spectrum magnitude of the wind farm feeder. While the faulty section within a feeder can be detected either by comparing the peak current or the instantaneous active power direction or the trajectory of positive sequence line-ground impedance between two contiguous measurement units.

In the last part of this report, the DSP results for different system conditions are given. The proposed fault detection method tends to fail to detect the fault when the short-circuit current contribution from HVDC is reduced to 0.1 p.u., since the peak current and instantaneous active power in the collection point and along the feeder become very small.

## 5.2 Future works

- Investigate the behavior of the system when subjected to unbalance and high resistance short-circuit fault.
- Research the possibility to change the converter control scheme in the FCG and HVDC model.

# References

- [1] J. Schachner and I. Leoben, “Power connections for offshore wind farms,” Master’s thesis, Delft University/University of Leoben, 2004.
- [2] “Co-generation and renewables: Solutions for a low-carbon energy future,” tech. rep., International Energy Agency, 2011. available at <http://goo.gl/EHk8B>.
- [3] “Clean energy progress report,” tech. rep., International Energy Agency, 2011. available at <http://goo.gl/oUWHT>.
- [4] “Wind in power: 2010 european statistics,” tech. rep., The European Wind Energy Association, February 2011. available at <http://goo.gl/214rh>.
- [5] “Benefits of wind energy.” Website, 2009. available at <http://goo.gl/NT6a7>.
- [6] “Global wind report 2010,” tech. rep., Global Wind Energy Council, March 2011. available at <http://goo.gl/Jzlec>.
- [7] “Growth of wind turbine size.” Website. available at <http://goo.gl/5KAcD>.
- [8] D. Mehrzad, J. Luque, and M. C. Cuenca, “Vector control of PMSG for grid-connected wind turbine applications,” Master’s thesis, Institute of Energy Technology, Aalborg University, 2009.
- [9] G. Ramtharan, A. Arulampalam, J. Ekanayake, F. Hughes, and N. Jenkins, “Fault ride through of fully rated converter wind turbines with AC and DC transmission,” *Renewable Power Generation, IET*, vol. 3, pp. 426–438, december 2009.
- [10] Z. Chen, J. Guerrero, and F. Blaabjerg, “A review of the state of the art of power electronics for wind turbines,” *Power Electronics, IEEE Transactions on*, vol. 24, pp. 1859–1875, aug. 2009.
- [11] J. Baroudi, V. Dinavahi, and A. Knight, “A review of power converter topologies for wind generators,” in *Electric Machines and Drives, 2005 IEEE International Conference on*, pp. 458–465, may 2005.
- [12] B. V. Eeckhout, D. V. Hertem, M. Reza, K. Srivastava, and R. Belmans, “Economic comparison of VSC HVDC and HVAC as transmission system for a 300 MW offshore wind farm,” *European Transactions on Electrical Power*, vol. 20, pp. 661–671, 2010.
- [13] K. Meah and S. Ula, “Comparative evaluation of hvdc and hvac transmission systems,” in *Power Engineering Society General Meeting, 2007. IEEE*, pp. 1–5, IEEE, 2007.
- [14] “ABB differences with classic - HVDC light.” Website. available at <http://goo.gl/pbhTL>.

- [15] Y. Jiang-Hafner, M. Hyttinen, and B. Paajarvi, "On the short circuit current contribution of HVDC light," in *Transmission and Distribution Conference and Exhibition 2002: Asia Pacific. IEEE/PES*, vol. 3, pp. 1926 – 1932 vol.3, oct. 2002.
- [16] E. Muljadi, N. Samaan, V. Gevorgian, J. Li, and S. Pasupulati, "Short circuit current contribution for different wind turbine generator types," in *Power and Energy Society General Meeting, 2010 IEEE*, pp. 1 –8, july 2010.
- [17] "List of offshore wind farms." Website. available at <http://goo.gl/YACGU>.
- [18] "List of onshore wind farms." Website. available at <http://goo.gl/KjShq>.
- [19] "The roscoe Wind Farm project, Texas, USA." Website. available at <http://goo.gl/y7LX4>.
- [20] "Thanet offshore wind farm, Kent, United Kingdom." Website. available at <http://goo.gl/prVUn>.
- [21] "Offshore wind farms." Website. available at <http://goo.gl/azBHT>.
- [22] "First high sea wind power from BARD offshore 1." Website. available at <http://goo.gl/65uhW>.
- [23] T. Hansen, "Offshore wind farm layouts: Performance comparison for a 540 MW offshore wind farm," Master's thesis, Department of Electric Power Engineering, Norwegian University of Science and Technology, 2009.
- [24] "XLPE cable systems: User's guide." Website. available at <http://goo.gl/ygxSF>.
- [25] N. Mohan, T. Undeland, and W. Robbins, *Power electronics*. Wiley New York, 1995.
- [26] T. Shire, "VSC-HVDC based network reinforcement," 2009.
- [27] C. Du, "VSC-HVDC for industrial power systems," Master's thesis, Division of Electric Power Engineering, Department of Energy and Environment, Chalmers University of Technology, 2007.
- [28] A. Perdana, *Dynamic models of wind turbines: a contribution towards the establishment of standardized models of wind turbines for power system stability studies*. PhD thesis, Division of Electric Power Engineering, Department of Energy and Environment, Chalmers University of Technology, 2008.
- [29] J. Yang, Y. Gao, and J. O'Reilly, "Permanent magnet synchronous generator converter protection analysis during DC wind farm open-circuit fault condition," in *Electrical Power Energy Conference (EPEC), 2009 IEEE*, pp. 1 –6, oct. 2009.
- [30] L. Harnefors, *Control of variable-speed drives*. Västerås: Applied Signal Processing and Control, Department of Electronics, Mälardalen University, 2002.
- [31] S. Chaudhary, R. Teodorescu, P. Rodriguez, P. Kjær, and P. Christensen, "Modelling and simulation of VSC-HVDC connection for wind power plants," *Ph.D. Seminar on detailed Modelling and Validation of Electrical Components and Systems*, pp. 53–57, 2010.
- [32] D. Woodford, "Introduction to pscad/emtde v3," 2000.

- [33] P. Wilson and M. Craig, “Pscad user’s guide,” *HVDC Research Centre, Canada*, 2003.
- [34] N. Tleis, *Power systems modelling and fault analysis: theory and practice*. Newnes, 2007.
- [35] J. Cardenas, V. Muthukrishnan, D. McGinn, and R. Hunt, “Wind farm protection using an iec 61850 process bus architecture,” in *Developments in Power System Protection (DPSP 2010). Managing the Change, 10th IET International Conference on*, pp. 1–5, IET, 2010.
- [36] B. Lundqvist, “100 years of relay protection, the Swedish ABB relay history.” Website, August 2001. available at <http://goo.gl/oTb72>.
- [37] M. Yalla, “A digital multifunction protective relay,” *Power Delivery, IEEE Transactions on*, vol. 7, pp. 193 –201, jan 1992.
- [38] I. Zamora, A. Mazón, V. Valverde, E. Torres, and A. Dyško, “Power quality and digital protection relays,” in *International Conference on Renewable Energies and Power Quality 2004, Barcelona*, 2004.
- [39] M. Demler, *High-speed analog-to-digital conversion*. Academic Press (San Diego), 1991.
- [40] A. Johns and S. Salman, *Digital protection for power systems*. Peter Peregrinus Ltd, 1997.
- [41] M. Öhrström, *Fast fault detection for power distribution systems*. PhD thesis, Department of Electrical Engineering, Royal Institute of Technology, 2003.
- [42] F. Wang, *Power Quality Disturbances and Protective Relays*. PhD thesis, Division of Electric Power Engineering, Department of Energy and Environment, Chalmers University of Technology, 2001.
- [43] H. Slootweg and E. De Vries, “Inside wind turbines-fixed vs. variable speed,” *Renewable Energy World*, vol. 6, no. 1, pp. 30–41, 2003.
- [44] S. Muyeen, R. Takahashi, T. Murata, and J. Tamura, “A method to calculate initial conditions of wind generator in transient stability simulation,” in *3rd International Conference on Electrical & Computer Engineering*, pp. 175–178, 2004.
- [45] C. Andreea, *Encoderless Vector Control of PMSG for Wind Turbine Applications*. Lambert Academic Publishing, 2011.

# Appendix A

## FCG components modeling

### A.1 Aerodynamic model

Power extraction from wind by wind turbine can be calculated using Betz equation given as:

$$P_m = \frac{1}{2} \rho A v_w^3 C_p(\lambda, \beta) \quad (\text{A.1})$$

where  $P_m$  is the turbine mechanical power,  $\rho$  is the air density,  $A$  is the blade swept area,  $v_w$  is the wind speed,  $C_p$  is the power coefficient of the blade, and  $\beta$  is the blade pitch angle (BPA). The value of tip speed ratio (TSR) or  $\lambda$  can be calculated using (A.2)

$$TSR = \frac{\omega R}{v_w} \quad (\text{A.2})$$

where  $\omega$  is the turbine rotor angular speed, and  $R$  is the turbine blades radius.

From (A.1),  $C_p$  is a nonlinear function of  $\lambda$  and  $\beta$ , and depends on the turbines structure. The  $\lambda$  value of fixed-speed wind turbine cannot be controlled and it gives the optimum  $C_p$  only for particular wind speed. With variable-speed wind turbine,  $C_p$  can be optimized to maximize power extraction for wide range of wind speed [43]. A typical power curve of fixed and variable-speed wind turbine is shown in Fig. A.1. An example of numerical approximation of  $C_p$  is given by [44] in the following form:

$$C_p(\lambda, \beta) = 0.73 \left( \frac{151}{\lambda_i} - 0.58\beta - 0.002\beta^{2.14} - 13.2 \right) e^{-\frac{18.4}{\lambda_i}} \quad (\text{A.3})$$

where

$$\lambda_i = \left( \frac{1}{\lambda - 0.02\beta} - \frac{0.003}{\beta^3 + 1} \right)^{-1} \quad (\text{A.4})$$

From (A.1), if  $v_w$  is invariable then  $P_m$  is directly proportional to  $C_p$ . It can be seen from Fig. A.2 that in order to maximize power extraction from the wind,  $\beta$  must be at the minimum and  $\lambda$  must be at the optimum (within 6-8).

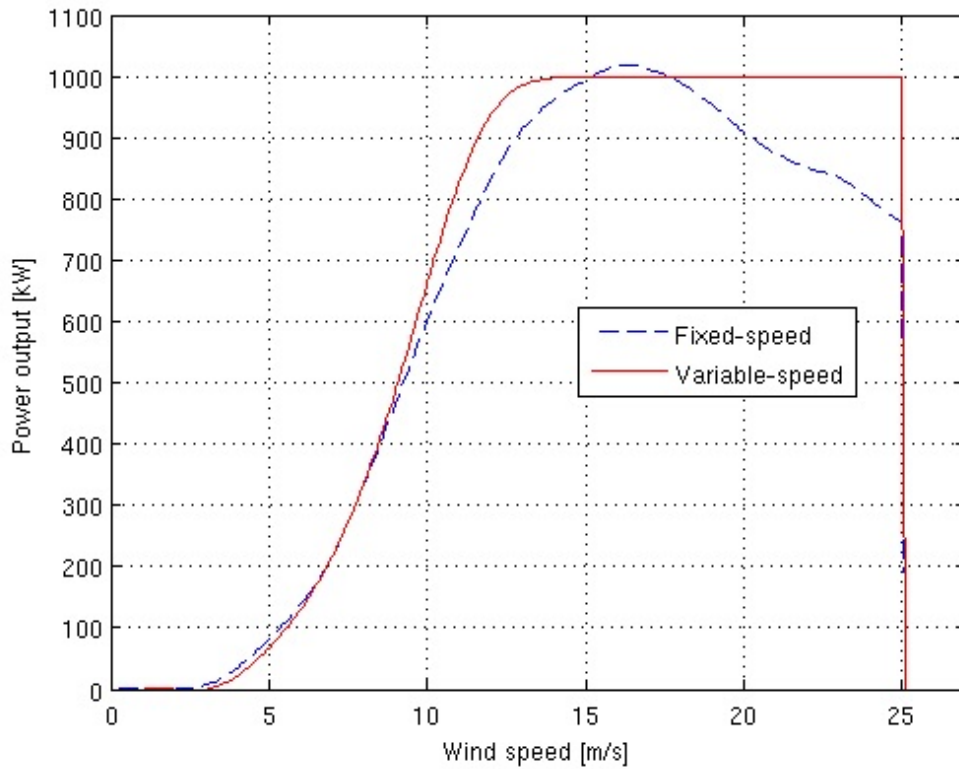


Figure A.1: A typical wind turbine power curve

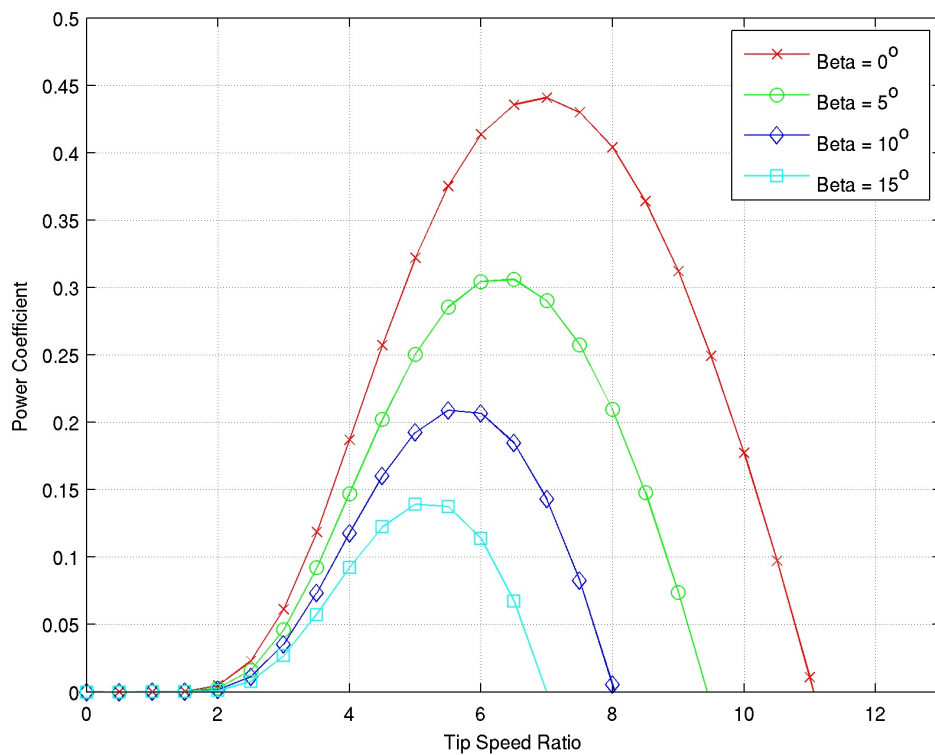


Figure A.2:  $C_p$ - $\lambda$  curve for different  $\beta$

## A.2 Permanent Magnet Synchronous Machine model

The PMSG is modeled in  $dq$ -representation assuming that it has sinusoidal flux distribution in the air gap and no zero components in the three phase quantities. The transformation from three-phase quantities to  $dq$ -axis is done by aligning the  $d$ -axis to the rotor flux as depicted in Fig. A.3. The stator voltage equation can be expressed as:

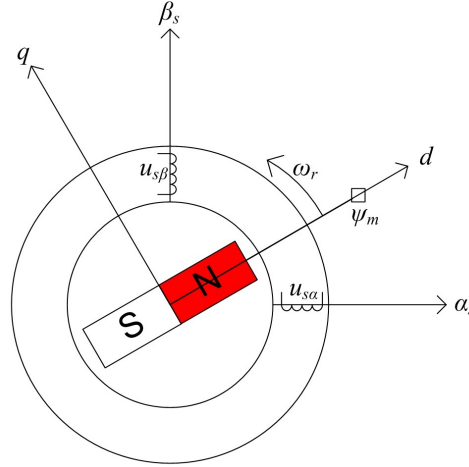


Figure A.3: Simple  $dq$ -axis representation in 2 poles PM machine

$$\begin{aligned} u_{sd} &= R_s i_{sd} - \omega_r \psi_{sq} + \frac{d\psi_{sd}}{dt} \\ u_{sq} &= R_s i_{sq} + \omega_r \psi_{sd} + \frac{d\psi_{sq}}{dt} \end{aligned} \quad (\text{A.5})$$

where  $u_{sd}$  and  $u_{sq}$  are the stator voltage in  $dq$ -axis,  $R_s$  is the stator resistances,  $i_{sd}$  and  $i_{sq}$  are the stator current in  $dq$ -axis,  $\omega_r$  is the rotor electrical speed,  $\psi_{sd}$  and  $\psi_{sq}$  are the  $dq$ -axis representation of stator flux linkage. Flux linkage equations are given in (A.6) as follow:

$$\begin{aligned} \psi_{sd} &= L_{sd} i_{sd} + \psi_m \\ \psi_{sq} &= L_{sq} i_{sq} \end{aligned} \quad (\text{A.6})$$

where  $L_{sd}$  and  $L_{sq}$  are the stator inductance in  $dq$ -axis. By inserting (A.6) to (A.5), stator voltage equations become:

$$\begin{aligned} u_{sd} &= R_s i_{sd} - \omega_r L_{sq} i_{sq} + L_{sd} \frac{di_{sd}}{dt} \\ u_{sq} &= R_s i_{sq} + \omega_r (L_{sd} i_{sd} + \psi_m) + L_{sq} \frac{di_{sq}}{dt} \end{aligned} \quad (\text{A.7})$$

The rotor electrical speed ( $\omega_r$ ) in the previous equations can be calculated as follows:

$$\omega_r = \omega_m n_p \quad (\text{A.8})$$

where  $n_p$  is the number of rotor pole pair. The mechanical angular speed ( $\omega_m$ ) can be expressed as a function of electrical torque ( $T_e$ ) and mechanical torque ( $T_m$ ) as given in the following equation:

$$J \frac{d\omega_m}{dt} = T_m - T_e - B\omega_m \quad (\text{A.9})$$

where  $J$  is the moment inertia of the rotor, and  $B$  is the viscous damping.

The space vector representation of electrical torque ( $T_e$ ) is given by the following equation:

$$T_e = \frac{3n_p}{2} \text{Im}\{\psi_s^* i_s\} \quad (\text{A.10})$$

by inserting (A.6) into (A.10), electrical torque equation become:

$$T_e = \frac{3n_p}{2} (\psi_m i_{sq} + (L_{sd} - L_{sq}) i_{sd} i_{sq}) \quad (\text{A.11})$$

It can be observed from (A.11) that there are two terms of torques which are synchronous torque and reluctance torque. The preceding is produced by the permanent magnet flux and  $q$ -axis current, while the later is produced by the difference of the inductance in  $dq$ -axis [45].

### A.3 Generator-side converter model

Field Oriented Control (FOC) scheme is implemented in this study to control the PMSG. This control scheme relies on the transformation of three-phase quantities into two coordinate system ( $dq$ -representation), so that it similar to DC machine control. The transformation is implemented by aligning the  $d$ -axis to the rotating stator flux. Figure A.4

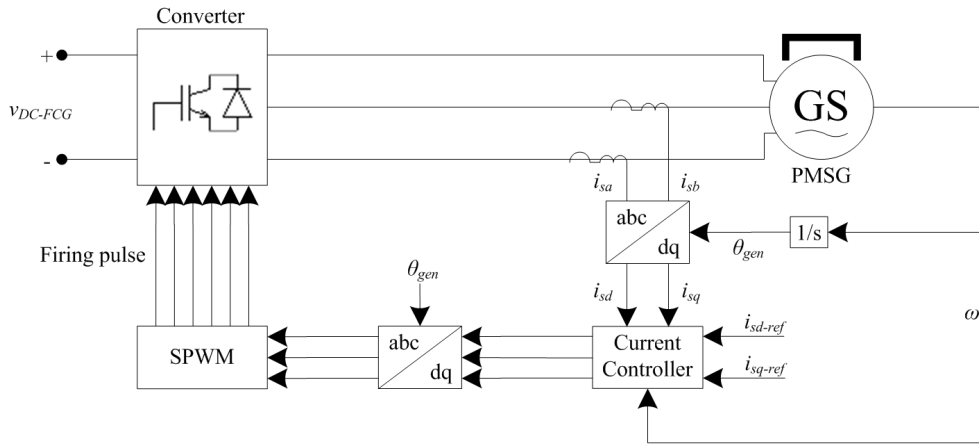


Figure A.4: Basic scheme of FOC for PMSG

represent the scheme of FOC. The current reference of the current controller in Fig. A.4 can be obtained from the outer controller which regulates the speed of PMSG.

As explained in [45] and [28], different control strategies can be applied. In this study, full torque control strategy is implemented. In order to maximize the torque, current reference in  $d$ -axis is always set to zero. The phasor diagram of this control strategy can be seen in Fig. A.5. By inserting current value from Fig. A.5 into (A.11), the electrical torque equation can be written as:

$$T_e = \frac{3n_p}{2} (\psi_m i_{sq}) \quad (\text{A.12})$$

From (A.12), it can be observed that the value of  $i_{sq}$  is linear to the value of  $T_e$ , which simplify the control property [45].

The structure of the current and speed controller of PMSG is represented in Fig. A.6. The  $q$ -axis control consist of outer controller (speed controller) and inner controller (current controller). The inner controller in both  $d$  and  $q$ -axis have the same properties. As a rule of thumb in control design, the inner controller bandwidth is at least 10 times faster than the outer one.

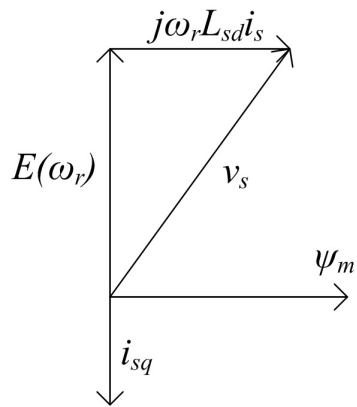


Figure A.5: Phasor diagram of full torque control strategy

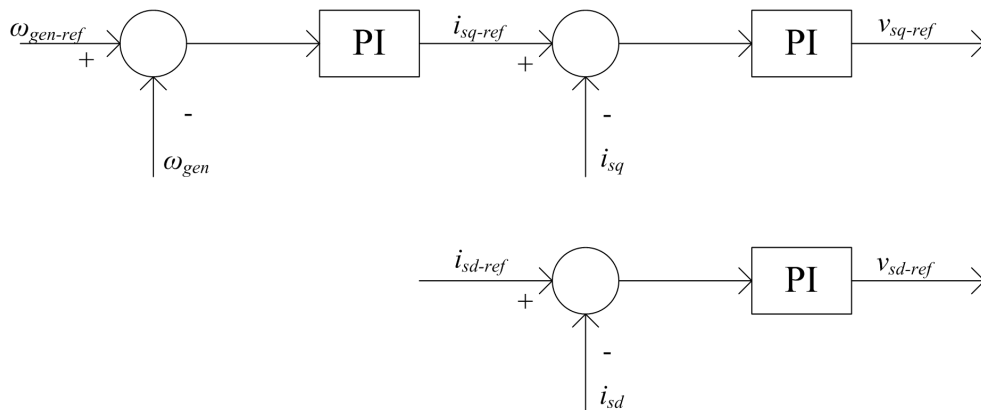


Figure A.6: PMSG control structure

# Appendix B

## FCG Model parameters

Table B.1: FCG model parameters

Part	Label	Description	Value	Unit
Wind Turbine	Vw	Rated wind speed	13	m/s
	Pturbine	Rated turbine power	3	MW
	Rrotor	Rotor radius	46.2	m
	Arotor	Rotor swap area	6705	m <sup>2</sup>
	Rho	Air density	1.225	kg/m <sup>3</sup>
	kp	Gain cst of turbine regulator control	6.5	
	ki	Integral cst of turbine regulator control	6.5	
	ks	Gain cst of speed damping	0.05	
	Gm	Gain multiplier	30	
PMSG	npp	Number of generator pole pairs	150	
	Sgen	Rated generator power	3	MVA
	freqgen	Generator frequency	50	Hz
	wref	Generator electrical speed	314.16	rad/s
	nsgen	Generator mechanical speed	20	rpm
	Vgen	Generator rated voltage	0.69	kV
	J	Generator inertia	2	pu
	B	Generator damping	0.002	pu
	VgenPh	Generator line to neutral voltage	0.39	kV
	VgenPeak	Generator peak voltage	0.56	kV
	Lbase	Base current	2.51	kA
	Lpeak	Current peak	3.55	kA
	Rs	Stator winding resistance	0.017	pu
	Xs	Stator leakage reactance	0.064	pu
Psi	Generator flux linkage	1	pu	
Rectifier	kpc_r	Gain cst of inner controller	1.4	
	Tic_r	Time cst of inner ctrl	0.059	
	kps_r	Gain cst of outer controller	60	
	Tis_r	Time cst of outer ctrl	0.001	
	Lgen	Estimated generator inductance	0.15	
	Idmax	Max current limit	1.1	pu
	Idmin	Min current limit	-1.1	pu
	Vdmax	Max voltage limit	1.05	pu

Continued on Next Page...

Table B.1 – Continued

<b>Part</b>	<b>Label</b>	<b>Description</b>	<b>Value</b>	<b>Unit</b>
	Vdmin	Min voltage limit	-1.05	pu
	Vqmax	Max voltage limit	1.05	pu
	Vqmin	Min voltage limit	-1.05	pu
DC-Link	DCv	rated DC voltage	1.1	kV
	Rbrake	Braking resistance	0.1	$\Omega$
	linkcap	DC-link capacitor	50	mF
	Dcvmax	max DC-link voltage	1.177	kV
Inverter	kps_i	Gain cst of current controller	10	
	Tis_i	Time cst of current controller	0.01	
	Hyband	Hysterisis band	0.05	
Transformer	Sxformer	Rated power of xformer	3	MVA
	LVxformer	Low voltage of xformer	0.69	kV
	HVxformer	High voltage of xformer	20	kV
	freqgrid	Grid frequency	50	Hz
	Lleak	Positive sequence leakage reactance	0.15	pu
	Culoss	Copper losses	0.015	pu
	Nlloss	No load losses	0.015	pu
PE Switch	Ron	ON Resistance	0.001	$\Omega$
	Roff	OFF Resistance	1	M $\Omega$